

*Wake Dynamics of a
Cylinder with a Flexible
Splitter Plate*

An Experimental Study

by

Aniruddha Deepak Paranjape

Wake Dynamics of a Cylinder with a Flexible Splitter Plate

An Experimental Study

by

Aniruddha Deepak Paranjape

to obtain the degree of Master of Science
at the Faculty of Aerospace Engineering, Delft University of Technology.
to be defended publicly on Tuesday March 28, 2023 at 10:00 AM.

Student number: 5285134
Project duration: November 11, 2021 – March 28, 2023
Thesis Committee: Prof. Dr. Fluvio Scarano, TU Delft *Committee Chair*
Dr. A. Sciacchitano, TU Delft *Thesis Supervisor*
MSc. G. Gonzalez Saiz, TU Delft *Daily Supervisor*
Dr. W. Yu, TU Delft *External Member*

An electronic version of this thesis is available at <http://repository.tudelft.nl/>.

Preface

The present thesis report is a culmination of everything I have learned at the Faculty of Aerospace Engineering, TU Delft. It has been an honor and privilege to have had the opportunity to study at one of the most prestigious universities and faculty in the world. The journey at TU Delft has not only been educational but deeply spiritual. I have truly come to appreciate the power of aerodynamics and its potential in solving the challenges of today for a prosperous and sustainable future. TU Delft has tested my tenacity and determination, I feel proud that I have been able to dig deep and come out on top each time. Completing this course is far from a singular effort, I would not be here without some very special people in my life.

I would first like to thank my supervisor Dr. Andrea Sciacchitano. Prof. Sciacchitano is one of the best teachers I have had the opportunity to learn from. His best qualities as a teacher are his student-centric approach and his care for student finances and mental health. I will always remember his kindness when he graciously allowed me to change my exam slot as I had fallen sick just before the exam. I owe a great debt of gratitude to Prof. Sciacchitano for his patience, and support during this project. I also extend this gratitude to MSc. Gabriel Gonzalez Saiz, my daily supervisor, for sharing his expertise in performing experiments and processing experimental data for my thesis. I would not have been able to complete this project without their valuable input and insights. I would like to take this opportunity to thank the thesis committee members for taking the time out of their busy schedules and engaging in a scientific discussion and providing me with valuable feedback.

I would firstly like to thank Riddhima for always pointing me in the right direction and motivating me at the most difficult moments. Thank you for your love, never-ending support, and company through all our zoom calls! I would like to thank my frequent collaborators, Aaron, Jahnavi, Nikhil, and Siddharth. Their help and support academically and otherwise has helped me manage the challenges of TU Delft. I would also like to thank my friends Parth, Naazneen, Ananya, Amrit, Viraj, Ram, Vishwanath, Naman, Harsha, and Shardul for their love and support, which has meant the world to me. A special thanks to my friends in Delft, Anitej, Abhishek, Arun, Mrinal, Saransh, and Yash. There has never been a dull moment with you lot.

I would like to thank my parents, Mrs. Deepa and Mr. Deepak Paranjape, without whom none of this would be possible. You have very patiently and graciously supported my love for aviation since I was a little boy. Thank you for taking me plane spotting, allowing me to play hours of Flight Simulator, giving up the window seat on all the flights we have taken together, and for giving me a chance to explore my obsession. When becoming a pilot wasn't an option due to my colorblindness, you provided me with all the means to get the best education so that I could still work closely with airplanes. Thank you for teaching me compassion, empathy, and the value of hard work. I would not be here without your unconditional love, trust, support, and understanding. I would like to dedicate this thesis to you, my dearest *Aai* and *Baba*.

Aniruddha Deepak Paranjape
Delft, February 2023

Abstract

As the world grapples with the challenges of global warming, there has been a significant push for the development of new methods of harnessing renewable energy. Energy harvesters have been a new avenue to generate electrical power locally for remote applications. An energy harvester is a device that taps into aeroelastic phenomena to convert vibrational energy into electrical energy. Additional benefits of harvesters include being lower in complexity, ease of maintenance, and the resulting cost-effectiveness.

The splitter plate represents a wake control device that alters the wake to make the energy capture more efficient and practical when attached to a cylinder. However, the flow mechanisms under different conditions have not been fully understood. The motivation of the present work is to bridge this gap by characterizing the mechanisms and wake dynamics of a cylinder with a flexible splitter plate. This will help advance the understanding of the wake behavior of these devices in order to make safe and efficient devices. In order to characterize the behavior of the wake, measurements are made at different flow speeds. A preliminary analysis of the splitter plate motion showed that increasing the Reynolds number produced four distinct regimes to be studied further: *crossover*, *baseline*, *reduced amplitude*, and *chaotic*. The initial analysis also revealed a condition named *burst*, defined as a period of resonant, two-dimensional, high amplitude oscillations of the splitter plate. All regimes are compared to a bare cylinder with no splitter plate to ascertain differences in wake behavior.

The use Helium Filled Soap Bubbles (HFSB) in flow diagnostic tools such as Particle Image Velocity (PIV) experiments has permitted large-scale measurements. In particular, a Lagrangian Particle Tracking (LPT) experiment was performed in which the HFSB is tracked individually with the help of an algorithm. The present study employs Shake-The-Box (STB), a novel LPT tracking algorithm that uses time-resolved experimental data to predict future tracer particle locations. The benefit of such an algorithm includes reduced ghost particle detection and computational efficiency. The details of this experimental method have been covered extensively in this thesis. The raw experimental data was processed to perform statistical analysis, proper orthogonal decomposition, and spectral analysis to provide insights to meet the thesis objective.

The study showed that the flexible splitter plate influences the wake behavior when compared to a bare cylinder by affecting the normal vortex formation processes, such as communication between the separated shear layers of the cylinder. It additionally affects the entrainment process in the formation region, which suppresses vortex shedding. During a burst, it was observed that the large oscillations of the plate allowed for more communication which restored the vortex shedding. As a result, it was determined that the appropriate way to categorize the wake is when the plate experiences regular deformations and when it experiences a burst.

Contents

Preface	iii
Abstract	v
Nomenclature	xi
List of Figures	xvii
List of Tables	xix
1 Introduction	1
2 Literature Review: Cylinder with a Flexible Splitter Plate	5
2.1 Vortex Shedding of Circular Cylinders	6
2.1.1 Reynolds Number Effects on Cylinder Wake	7
2.1.2 Strouhal Number	8
2.2 Flow Induced Vibrations	8
2.3 Splitter Plates	11
2.3.1 Key Parameters of a Splitter Plate	11
2.3.2 Types of Splitter Plates	13
2.4 Types of Instabilities for Splitter Plates	14
2.5 Effect on Vortex Shedding and Formation	15
2.6 Effect of Plate Length	16
2.7 Kinematics of a Splitter Plate	18
2.8 Effect of Non-Dimensional Bending Stiffness	20
2.9 Energy Harvesting Using a Splitter Plate	21
2.10 Research Gap	23
2.11 Research Goal	23
2.12 Research Question(s)	23
3 Measurement Techniques	25
3.1 Introduction	25
3.2 Working Principles	25
3.2.1 Tracer Particles	26
3.2.2 Illumination	27
3.2.3 Imaging	27
3.3 Tomographic Particle Image Velocimetry	28
3.4 Helium Filled Soap Bubbles (HFSB)	28
3.5 Lagrangian Particle Tracking	29
3.5.1 Shake-The-Box	30
4 Experimental Setup	33
4.1 Wind Tunnel Facility	33
4.2 Model Details	34
4.2.1 Cylinder	34
4.2.2 Splitter Plate	35

4.3	PIV Equipment Details	36
4.3.1	Frame Structure and Final Setup	36
4.3.2	Helium Filled Soap Bubbles (Tracer Particle)	36
4.3.3	Light Sources for PIV	37
4.3.4	High-Speed Cameras	38
4.3.5	Acquisition	38
4.4	Parameters	38
4.5	Preliminary Testing	39
5	Image Analysis and Data Processing	43
5.1	Pre-Processing	43
5.2	Volume Self-Calibration and Optical Transfer Function	44
5.3	Processing: Shake-The-Box Parameters	45
5.4	Binning	46
5.5	Post-Processing	47
5.5.1	Proper Orthogonal Decomposition	48
5.5.2	Power Spectral Density	49
6	Results	51
6.1	Baseline, $Re = 25,700$	51
6.1.1	Statistical Analysis	51
6.1.2	Time Series and Spectral Decomposition	53
6.1.3	Proper Orthogonal Decomposition	55
6.2	Reduced Amplitude Regime, $Re = 44,100$	57
6.2.1	Statistical Analysis	57
6.2.2	Time Series and Spectral Decomposition	58
6.2.3	Proper Orthogonal Decomposition	60
6.3	Chaotic Regime, $Re = 68,600$	63
6.3.1	Statistical Analysis	63
6.3.2	Time Series and Spectral Decomposition	66
6.3.3	Proper Orthogonal Decomposition	68
7	Conclusions and Recommendations	73
7.1	Conclusions	73
7.2	Recommendations	75
	References	81
A	Crossover Regime: Results	83
A.1	Statistical Analysis	83
A.2	Time Series and Spectral Decomposition	83
A.3	Proper Orthogonal Decomposition	86

Nomenclature

Abbreviations

AWE	Airborne Wind Energy
BNC	Bayonet NeillConcelman
CAGR	Compound Annual Growth Rate
CCD	Charged Coupled Devices
CMOS	Complementary MetalOxideSemiconductor
EIE	Extraneously - Induced Excitation
FIV	Flow Induced Vibrations
FOV	Field of View
FSI	Fluid-Structure Interaction
FSU	Fluid Supply Unit
HFSB	Helium Filled Soap Bubbles
IIE	Instability - Induced Excitation
IPR	Iterative Particle Reconstruction
LPT	Lagrangian Particle Tracking
MART	Multiplicative Algebraic Reconstruction Technique
MIE	Movement - Induced Excitation
OTF	Optical Transfer Function
PIV	Particle Image Velocimetry
POD	Proper Orthogonal Decomposition
PSD	Power Spectral Density
PXL	Pixel
RPM	Rotations Per Minute
SMART	Simultaneous Multiplicative Algebraic Reconstruction Technique
STB	Shake-The-Box
SVD	Singular Value Decomposition

Tomo-PIV	Tomographic Particle Image Velocimetry
USB	Universal Serial Bus
VIV	Vortex Induced Vibrations
VSC	Volume Self-Calibration

Symbols

\bar{u}	Steady Component of Velocity Vector
Δt	Laser Pulse Separation
δz	Depth of Field
δ_s	Shake Distance
ϵ	Strain
ϵ_{axial}	Axial Compression
ϵ_{trans}	Transverse Elongation
\hat{P}_M	Modified Periodogram Power Spectral Density
\hat{P}_W	Power Spectral Density
λ	Wavelength of light
λ_k	Eigenvalues
μ	Dynamic Viscosity
$\nabla \cdot$	Divergence Operator
∇	Gradient Operator
ν	Poisson Ratio
ω	Vorticity
∂	Partial Differentiation Operator
ϕ_k	Orthonormal Spatial Modes
ρ	Air Density
ρ_p	Tracer Particle Density
ρ_{sp}	Splitter Plate Density
σ	Axial Stress
\vec{u}	Velocity Vector
A^*	Non-dimensional Amplitude
A_k	Time Coefficients

D	Material Derivative Operator
d_i	Image Distance
d_o	Object Distance
d_p	Tracer Particle Diameter
D_{app}	Apperture Diameter
D_{cyl}	Cylinder Diameter
E	Young's Modulus
EI	Flexural Rigidity
f	Focal Length
f^*	Non-dimensional Frequency
$f\#$	F-Stop
f_s	Vortex Shedding Frequency
g	Acceleration due to Gravity
I	Pixel Intensity
K^*	Non-dimensional Bending Stiffness
L	Characteristic Length
L_{sp}	Length of Splitter Plate
M	Magnification Factor
p	Pressure
u'	Fluctuating component of Velocity Vector
U_g	Gravity Induced Velocity
V	Particle Velocity
V_∞	Freestream Velocity
w	Window Function
St	Strouhal Number
Re	Reynolds Number

List of Figures

2.1	Collar Triangle [78]	5
2.2	Formation region in the wake of a cylinder from Gerrard [39]. <i>(a)</i> , <i>(b)</i> Flow entrainment, and <i>(c)</i> Flow reversal	6
2.3	The regimes of vortex shedding across a smooth cylinder [19, 50]	8
2.4	The relationship between Strouhal and Reynolds number for circular cylinders [19, 50]	9
2.5	Characterization of FIVs [13, 69]	9
2.6	Lock-in bands for the resonance of the vortex shedding and transverse oscillations [19]	10
2.7	Various methods of vortex suppression [46, 19]. <i>Top Row, Left to right:</i> Splitter Plate, Ribbons, Pivoted Guiding Vane, Spoiler Plates. <i>Bottom</i> <i>Row, Left to right:</i> Helical Strakes, Shroud, Axial Slats, Streamline fairing.	10
2.8	Classification of control methods for flow over a bluff body [26].	11
2.9	The geometric configuration of a cylinder with an attached splitter plate [31]	12
2.10	Types of splitter plates (a) Rigid Splitter Plate (b) Flexible Splitter Plate [66]	13
2.11	A wire mesh 'permeable' splitter plate used by Cardell [22]	13
2.12	The categorization of the different sources of excitations [82]	15
2.13	Development of the secondary vortex over one oscillation cycle of the splitter plate. Reproduced from Wu et al. [80].	16
2.14	Variation of Strouhal number with L/D ratio [12]. The * markers are measurements from hot-wire anemometry while the solid circle markers are from film.	17
2.15	Vortex formation for a plain cylinder and splitter plate of different lengths. [12]. <i>(a)</i> Plain Cylinder, <i>(b)</i> $L/D \leq 1/4$, <i>(c)</i> $L/D = 1/2$, <i>(d)</i> $L/D = 1$, <i>(e)</i> $L/D = 1.5$, <i>(f)</i> $L/D = 2$	17
2.16	A summary of the effects of the splitter plate length from Anderson et al. [10]	18
2.17	Amplitude of the flexible splitter plate from Shukla et al. [66]. Addi- tionally the sub-figures <i>(a)</i> , <i>(b)</i> , and <i>(c)</i> highlight the periodicity of the regions being discussed.	19
2.18	Experimental Measurements by De Nayer et al. [31].	20
2.19	Experimental results of Shukla et al. [66] highlighting the effect of the flex- ural rigidity on the motion of the splitter plate. The non-dimensionality of the amplitude has been defined in Equation 2.7	21
2.20	Results of the use of splitter plate for energy harvesting [67]	22
2.21	Geometry of the oscillating 'eel' membrane in the wake of a bluff body, studied by Allen et al. [9]	22
3.1	Typical set up of an experiment with PIV [55]	26

3.2	A typical Tomographic PIV procedure [35]	29
3.3	(a) The use of HFSB under illumination by Bosbach et al. [21] studying cabin ventilation, (b) Detailed View	30
3.4	(a) Individual particles tracked in LPT (b) Single vector as a result of cross-correlation in PIV [36]	30
3.5	Schematic of the STB process in one time step as described by Schanz et al. [63]	31
3.6	Isosurfaces of vorticity ($\omega = 175/s$) obtained from (a) Tomo-PIV and (b) STB with grid interpolation at the same spatial resolution, from Schanz et al. [63]	32
4.1	The W-Tunnel, both images reproduced from TU Delft Aerodynamics Experimental Wiki [2]	34
4.2	The relationship between RPM of the W-Tunnel and the velocity	34
4.3	The model (cylinder with a flexible splitter plate) installed in the test section of the wind tunnel	35
4.4	The transparent flexible splitter plate against a dark background. The surface markers are made on the plate, additionally, 1 cm of space has been accounted for the mounting on the cylinder bracket. The surface markers are placed with a grid spacing of 1 cm with an average diameter of 0.8 mm	36
4.5	The final experimental set up in the W-Tunnel	37
4.6	Results of the preliminary study, the images across the measurement duration (1 second) are superimposed	40
4.7	Pre Result	40
5.1	The effect of the application of the symmetrical subtract time filter	44
5.2	The tracks developed by the STB algorithm for a measurement volume. The color bar represents the velocity magnitude of the particle tracks in m/s (Case: Sporadic Resonance)	45
5.3	Representation of the binned STB data in a selected X-Z plane. The colorbar represents the velocity magnitude of the particle tracks (Case: Sporadic Resonance)	48
6.1	The streamwise mean and standard deviation for the case $Re = 25,700$ (<i>Top: Cylinder without Splitter Plate, Below: Cylinder with Splitter Plate</i>). The limits of the splitter plate have been marked with a black dashed line. The velocity values are in m/s.	52
6.2	The transverse mean and standard deviation for the case $Re = 25,700$ (<i>Top: Cylinder without Splitter Plate, Below: Cylinder with Splitter Plate</i>). The limits of the splitter plate have been marked with a black dashed line. The velocity values are in m/s.	53
6.3	Time series of instantaneous transverse velocity at the point $x = 0.3089$ m, $y = 0.0179$ m, and $z = -0.0019$ m for the case $Re = 25,700$ (<i>Blue: Cylinder without Splitter Plate, Red: Cylinder with Splitter Plate</i>)	54
6.4	Power spectral density of instantaneous transverse velocity at the point $x = 0.3089$ m, $y = 0.0179$ m, and $z = -0.0019$ m for the case $Re = 25,700$ (<i>Blue: Cylinder without Splitter Plate, Red: Cylinder with Splitter Plate</i>)	54

6.5	Isosurfaces highlighting the spanwise coherence of the transverse velocity $w = 2$ m/s (in blue) and $w = -2$ m/s (in red) for the case $Re = 25,700$. The splitter plate has been shown in its neutral position.	55
6.6	Energy distribution over the first ten modes for the case $Re = 25,700$. . .	56
6.7	The first four streamwise mode shapes for the case $Re = 25,700$ (<i>Top: Cylinder without Splitter Plate, Below: Cylinder with Splitter Plate</i>). The limit of the splitter plate has been marked with a black dashed line. All the velocity values are in m/s.	56
6.8	The first four transverse mode shapes for the case $Re = 25,700$ (<i>Top: Cylinder without Splitter Plate, Below: Cylinder with Splitter Plate</i>). The limits of the splitter plate have been marked with a black dashed line. All the velocity values are in m/s.	57
6.9	The streamwise mean and standard deviation for the case $Re = 44,100$ (<i>Top: Cylinder without Splitter Plate, Below: Cylinder with Splitter Plate</i>). The limits of the splitter plate have been marked with a black dashed line. The velocity values are in m/s.	58
6.10	The transverse mean and standard deviation for the case $Re = 44,100$ (<i>Top: Cylinder without Splitter Plate, Below: Cylinder with Splitter Plate</i>). The limits of the splitter plate have been marked with a black dashed line. The velocity values are in m/s.	59
6.11	Time series of instantaneous transverse velocity at the point $x = 0.3089$ m, $y = 0.0179$ m, and $z = 0.0143$ m for the case $Re = 44,100$ (<i>Blue: Cylinder without Splitter Plate, Red: Cylinder with Splitter Plate</i>)	60
6.12	Power spectral density of instantaneous transverse velocity at the point $x = 0.3089$ m, $y = 0.0179$ m, and $z = 0.0143$ m for the case $Re = 44,100$ (<i>Blue: Cylinder without Splitter Plate, Red: Cylinder with Splitter Plate</i>)	60
6.13	Isosurfaces highlighting the spanwise coherence of the transverse velocity $w = 3$ m/s (in blue) and $w = -3$ m/s (in red) for the case $Re = 44,100$. The splitter plate has been shown in its neutral position.	61
6.14	Energy distribution over the first ten modes for the case $Re = 44,100$. . .	61
6.15	The first four streamwise mode shapes for the case $Re = 44,100$ (<i>Top: Cylinder without Splitter Plate, Below: Cylinder with Splitter Plate</i>). The limits of the splitter plate have been marked with a black dashed line. The velocity values are in m/s.	62
6.16	The first four transverse mode shapes for the case $Re = 44,100$ (<i>Top: Cylinder without Splitter Plate, Below: Cylinder with Splitter Plate</i>). The limits of the splitter plate have been marked with a black dashed line. The velocity values are in m/s.	62
6.17	The streamwise mean and standard deviation for the case $Re = 68,600$ (<i>Top: Cylinder without Splitter Plate, Below: Cylinder with Splitter Plate</i>). The limits of the splitter plate have been marked with a black dashed line. The velocity values are in m/s.	64
6.18	The transverse mean and standard deviation for the case $Re = 68,600$ (<i>Top: Cylinder without Splitter Plate, Below: Cylinder with Splitter Plate</i>). The limits of the splitter plate have been marked with a black dashed line. The velocity values are in m/s.	65

6.19	The streamwise and transverse mean and standard deviation for the case $Re = 68,600$ (<i>Top: Mean, Below: Standard Deviation</i>). The limits of the splitter plate have been marked with a black dashed line. The velocity values are in m/s.	65
6.20	Time series of instantaneous transverse velocity at the point $x = 0.2927$ m, $y = 0.0395$ m, and $z = 0.0305$ m for the case $Re = 68,600$ with the regular chaotic motion of the splitter plate. (<i>Blue: Cylinder without Splitter Plate, Red: Cylinder with Splitter Plate</i>)	66
6.21	Power spectral density of instantaneous transverse velocity at the point $x = 0.2927$ m, $y = 0.0395$ m, and $z = 0.0305$ m for the case $Re = 68,600$ with the regular chaotic motion of the splitter plate. (<i>Blue: Cylinder without Splitter Plate, Red: Cylinder with Splitter Plate</i>)	67
6.22	Time series of instantaneous transverse velocity at the point $x = 0.2927$ m, $y = 0.0395$ m, and $z = 0.0305$ m for the case $Re = 68,600$ for the resonant splitter plate motion. (<i>Red: Cylinder without Splitter Plate, Blue: Resonant Splitter Plate</i>)	67
6.23	Power spectral density of instantaneous transverse velocity at the point $x = 0.2927$ m, $y = 0.0395$ m, and $z = 0.0305$ m for the case $Re = 68,600$ for the resonant splitter plate motion. (<i>Top: Cylinder without Splitter Plate, Below: Resonant Splitter Plate</i>)	68
6.24	Isosurfaces highlighting the spanwise coherence of the transverse velocity $w = 5.5$ m/s (in blue) and $w = -5.5$ m/s (in red) for the case $Re = 68,600$. The splitter plate has been shown in its neutral position.	68
6.25	Energy distribution over the first ten modes for the case $Re = 68,600$	69
6.26	The first four streamwise mode shapes for the case $Re = 68,600$ (<i>Top: Cylinder without Splitter Plate, Below: Cylinder with Splitter Plate</i>). The limits of the splitter plate have been marked with a black dashed line. The velocity values are in m/s.	70
6.27	The first four transverse mode shapes for the case $Re = 68,600$ (<i>Top: Cylinder without Splitter Plate, Below: Cylinder with Splitter Plate</i>). The limits of the splitter plate have been marked with a black dashed line. The velocity values are in m/s.	70
6.28	The first four streamwise and transverse mode shapes for the resonant splitter plate case $Re = 68,600$ (<i>Top: Streamwise Modes, Below: Transverse Modes</i>). The limits of the splitter plate have been marked with a black dashed line. The velocity values are in m/s.	71
A.1	The streamwise mean and standard deviation for the case $Re = 22,000$ (<i>Top: Cylinder without Splitter Plate, Below: Cylinder with Splitter Plate</i>). The limits of the splitter plate have been marked with a black dashed line. The velocity values are in m/s.	84
A.2	The transverse mean and standard deviation for the case $Re = 22,000$ (<i>Top: Cylinder without Splitter Plate, Below: Cylinder with Splitter Plate</i>). The limits of the splitter plate have been marked with a black dashed line. The velocity values are in m/s.	84
A.3	Time series of instantaneous transverse velocity at the point $x = 0.3089$ m, $y = 0.0179$ m, and $z = -0.0019$ m for the case $Re = 22,000$ (<i>Blue: Cylinder without Splitter Plate, Red: Cylinder with Splitter Plate</i>)	85

A.4	Power spectral density of instantaneous transverse velocity at the point $x = 0.3089$ m, $y = 0.0179$ m, and $z = -0.0019$ m for the case $Re = 22,000$ (<i>Blue: Cylinder without Splitter Plate, Red: Cylinder with Splitter Plate</i>)	85
A.5	Isosurfaces highlighting the spanwise coherence of the transverse velocity $w = 1.5$ m/s (in blue) and $w = -1.5$ m/s (in red) for the case $Re = 22,000$. The splitter plate has been shown in its neutral position.	86
A.6	Energy distribution over the first ten modes for the case $Re = 22,000$. . .	86
A.7	The first four streamwise mode shapes for the case $Re = 22,000$ (<i>Top: Cylinder without Splitter Plate, Below: Cylinder with Splitter Plate</i>). The limits of the splitter plate has been marked with a black dashed line. The velocity values are in m/s.	87
A.8	The first four transverse mode shapes for the case $Re = 22,000$ (<i>Top: Cylinder without Splitter Plate, Below: Cylinder with Splitter Plate</i>). The limits of the splitter plate has been marked with a black dashed line. The velocity values are in m/s.	87

List of Tables

2.1	Important parameters of the splitter plate	12
4.1	Physical properties of the flexible splitter plate	35
4.2	Details of the optical setup	38
4.3	Experimental Parameters in the Wind Tunnel	39
4.4	Experimental parameters for PIV	39
4.5	Preliminary testing regime categorization	39
5.1	Parameters for the Volume Self Calibration	45
5.2	Parameters for Shake-The-Box, Case $Re = 27,500$	47
5.3	Parameters for Binning	48

1

Introduction

Energy is a convertible resource that drives technological growth and sustains the functions of society. However, due to the population growth exceeding the average 2%, the energy demand has never been higher. This has necessitated a substantial overhaul in the manner in which energy is being produced, distributed, and consumed [18]. Additionally, the current dependence on fossil fuel is a contributor not only to global warming but also to other environmental threats such as acid rain, air pollution, forest depletion, etc [33]. Renewable energy presents a more sustainable approach to energy production. The adoption and expansion of renewable energy is a significant way in which countries are implementing energy transition to meet policy goals. Between 2002 and 2017, countries such as China, India, Ireland, and Great Britain, have all increased their compound annual growth rate (CAGR) of renewable energy consumption[59].

Renewable energy of course encompasses all of the various energy sources such as wind, solar, hydro, geothermal, etc. However, wind energy is a global resource with the potential to extract energy either onshore or offshore through the use of conventional wind turbines/farms. Despite the technological advancements in the field of wind energy, there are still barriers to widespread development. In particular, Diógenes et al. [34] reviewed the barriers to wind energy implementation. In the study, it was found that the barriers to growth are mainly in the form of market failures (lack of awareness, lack of competition, restricted access to technology, etc), market distortions, financial factors (high capital costs, limited financial institutions/instruments), institutional (legal framework, unstable macroeconomics), and most importantly technical barriers (standards and certifications, lack of maintenance, system constraints) [34]. The complicated and variable nature of the hurdles necessitates a paradigm shift in the extraction of energy through the wind.

Over the years a number of solutions have been developed to overcome the challenges presented by energy generation from conventional wind energy sources. To combat the saturation of land with suitable wind potential, there is significant research into airborne wind energy (AWE). It is well known that wind over land creates a so-called '*atmospheric boundary layer*'. In this boundary layer, the flow closest to the ground is much slower than the flow at a certain height. AWE works on the concept of a machine that can be deployed at an altitude to extract energy from the wind with a higher potential, at the same time reducing the amount of space the base station occupies on the ground. For a long time, research into such concepts was not favored, but in recent decades has seen renewed interest [25]. Another concept that is being researched is an energy harvester that utilized Flow-Induced Vibrations (FIV).

In principle, a wind energy harvesting device taps into aeroelastic phenomena such as FIV, galloping, and flutter for energy conversion with the wind being the source. FIV have been encountered in several engineering fields such as aerospace, power generation, civil, and undersea cables. Flow around a bluff body leads to periodic vortex shedding in the wake. As a result of the shed vortices, the wake develops an asymmetrical pressure field and causes the bluff body to undergo vibrations itself [69]. These vibrations can be utilized to produce electricity using piezoelectric materials. However, such forms of vibrations are limited to a narrow range of velocities where the shedding frequency matches the natural frequency of the bluff body. To circumvent the issue of the narrow working range of such devices, additional modifications are made to the bluff body structure to 'remove' the upper limit on the velocity making it more practically usable [67].

One such modification is using a flexible splitter plate. A splitter plate is a two-dimensional surface that is mounted in the wake centerline in a direction that is parallel to the flow [45]. Historically it has been studied by Roshko [56, 57, 58], Gerrard [39], and Apelt et al. [12]. The flexible structure is locally deformed by the force the fluid exerts on it. The process becomes coupled when the structure also influences the flow. The splitter plate influences not only the near wake dynamics of the bluff body but also the vortex formation region. This is achieved by reducing the interactions between the separated shear layers of the bluff body and moving them further downstream [39]. These are complex aeroelastic interactions that have been historically investigated in two-dimensional flow conditions. In terms of other practical applications, this represents flag-flutter [82], the swimming motion of a tadpole and fish [9], a tool for Vortex-Induced Vibration suppression [15], and as a benchmark case for numerical aeroelasticity [31, 30].

Energy harvesters are an attractive alternative to traditional wind turbines and farms as they can produce energy locally. This means the electrical losses in long power lines can be minimized. Harvesters are also cheaper and due to their low complexity, are easier to maintain. Despite these advantages, harvesters still have a long way to go to become more efficient and well-understood. In particular, the flow fields and mechanisms under complex conditions have not been fully understood [69]. The overarching goal of this research is to investigate the wake dynamics and aeroelasticity of a flexible splitter plate at different flow regimes. To do this, advanced Particle Image Velocimetry (PIV) techniques will be used. PIV is a flow diagnostic tool for aerodynamics where the flow is 'seeded' with reflective particles that are then captured using high-speed cameras. The images are then subjected to cross-correlation to reveal the average displacements from which the flowfield can be constructed [55]. In specific, Lagrangian Particle Tracking (LPT) will be used. As the name suggests LPT tracks individual particles from a Lagrangian perspective. Shake-The-Box (STB) is one such LPT scheme that uses temporal data from time-resolved experimental data. [63]The objective of the thesis is thus:

"To characterize the mechanisms and wake dynamics of a cylinder and flexible splitter plate configuration using a Lagrangian Particle Tracking experiment."

This document serves to present and discuss relevant literature on energy harvesting, PIV, and most importantly, the flexible splitter plate. The literature will form the basis to formulate the research questions based on the research gap identified in the literature. The experimental setup as well as data reduction techniques are discussed in detail followed by which the results

from the PTV experiment are reported. The conclusions from these results will be used to answer the research questions. The remainder of the report is organized as follows:

Chapter 2 presents the historical background of this project by discussing relevant literature. In particular, concepts of the cylinder with splitter plate, and PIV (in Chapter 3) will be discussed in depth. Additionally, Chapter 2 is also used in identifying the research gaps and then posing research goals and questions to bridge the gaps. Chapter 4 reports the experimental setup in order to obtain the data. The processes of converting the raw images into useful results is explored in Chapter 5. Chapter 6 dives deep into the results of the experimental campaign. In Chapter 7 conclusions are drawn from the results such that the research questions posed earlier can be answered. The chapter also leaves room for recommendations for future work. The references to this thesis are added at the end of the report.

2

Literature Review: Cylinder with a Flexible Splitter Plate

In this chapter literature concerning the flow around the cylinder and the flexible splitter plate is discussed. The discussion is centered around the vortex shedding from cylinders as well as parameters that are useful in discussing the splitter plate behavior. This chapter concluded by identifying the research gap and formulating the research question and goals.

Aeroelasticity is a subset of aerodynamics that gives a theoretical description of the interaction between aerodynamic, elastic, and inertial forces [78]. Generally, aeroelasticity is used to describe the fluid-structure interaction (FSI) of flexible structures. Figure 2.1 shows the so-called Collar's triangle. The triangle gives a simple overview of how aeroelasticity can be understood. The interaction between elastic and inertial forces gives rise to vibrations, while the interaction between inertial and aerodynamic forces is used to describe stability and control, and lastly the interaction between aerodynamic and elastic forces is used to describe static aeroelasticity. When all the forces interact with each other, it is known as dynamic aeroelasticity. The understanding of aeroelasticity has helped advance fields like aerospace and civil engineering by improving structural integrity.

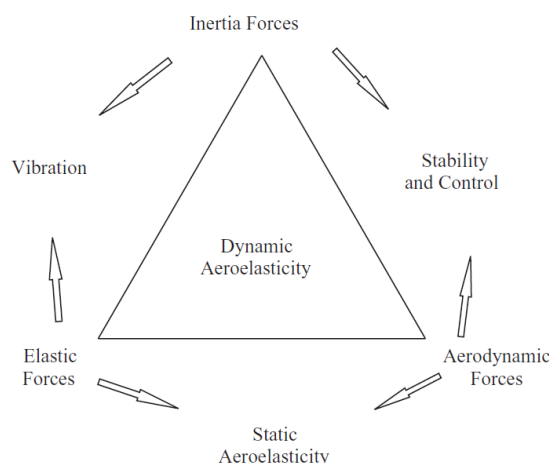


Figure 2.1: Collar Triangle [78]

The vortex shedding off a bluff body (particularly a circular cylinder) has been of interest to engineers and scientists alike for many years due to extensive real-life applications. Bluff body wakes are complex and involve shear layer interactions. These interactions result in a vortex street causing large pressure fluctuations and consequently transverse flow that may result in structural vibrations [74]. In addition to the vibrations, the periodic vortex shedding also produces noise and large drag forces.

2.1. Vortex Shedding of Circular Cylinders

The phenomenon of vortex shedding has been known to produce sound in Aeolian harps. It was Strouhal in 1878, who quantified with the Strouhal number, the relation between the flow velocity and the diameter of the Aeolian wires. Formally, the Strouhal number is a non-dimensional number that quantifies the frequency of shedding to the freestream velocity and the width of the cylinder. He found that the tones produced were directly proportional to the wind speed and inversely proportional to the wire diameter. Later, Lord Raleigh noted the transverse vibrations in violin strings due to the flow. In the 20th Century, Bernard and Von Kármán established the periodicity and stability of the vortex shedding process respectively [19].

Gerrard [39] studied the mechanics of the formation region behind bluff bodies. In specific he was looking at the formation of vortices. The *formation length* is the region (or length) behind the circular cylinder which is used to describe the fluctuating velocities in the wake. Additionally, it will provide the necessary basis to discuss the relation between the size of the formation region, the strength of vortex shedding, and the frequency of shedding.

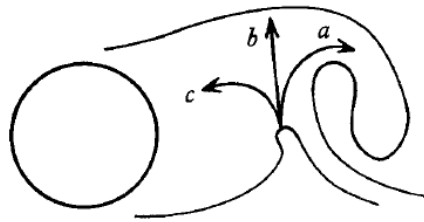


Figure 2.2: Formation region in the wake of a cylinder from Gerrard [39]. (a), (b) Flow entrainment, and (c) Flow reversal

More specifically, Bloor [20] describes the end of the formation region as the point on the wake axis that is closest to the cylinder, where a hot-wire anemometer will register the oscillating wake. This definition basically identifies the point where the wake first crosses the wake centerline. This is shown in Figure 2.2. The figure shows the instance when the fluid is pulled into the wake with the arrows showing the probable paths of the fluid after. From the figure, it is clear that some of the fluid is being entrained into the shear layer, on the other hand, some of the fluid experiences backflow toward the cylinder. Gerrard [39] also notes that only rotational flow bearing the opposite vorticity to the entraining layer can cross the wake centerline. This process is periodic, however, the process of entrainment is a continuous process. Thus, the size formation region is a balance of the fluid being entrained into the shear layers versus the fluid being subjected to a backflow. The author also proves that changes in vortex strength show a Reynolds number dependency. This is because the Reynolds number influences how much fluid is entrained by the turbulent shear layers. When the growing vortex is strong enough, it pulls the other across the wake, cutting off the supply of fluid from its own shear layer. And

this point the vortex is ejected into the wake from the near wake. Roshko [56] showed that if the formation region is reduced in size, the frequency of shedding increases, this is because the shear layers are brought closer to each other. Additionally, turbulence in the shear layers will result in a diffusion of vorticity reducing the shedding frequency as a result of insufficient vorticity concentration in them [39].

2.1.1. Reynolds Number Effects on Cylinder Wake

In the case of a cylinder, as the flow approaches it, it experiences increased pressure. This pressure is the stagnation pressure of the fluid that comes to rest at the leading edge. Away from the stagnation point, the flow develops on both sides with boundary layers. Reynolds number is a non-dimensional number that is a ratio of the inertial forces to the viscous forces. At high enough Reynolds numbers, the inertial forces dominate the flow and the boundary layer will separate from the cylinder. This separated flow is known as the shear layer on either side of the cylinder. As the name suggests, the shear layer consists of flow that varies from the slow-moving boundary layer to the faster-moving freestream flow. This causes the detached layers to roll into vortices in the near wake [19, 54, 74].

The Reynolds number of an object is defined as [11] :

$$\text{Re} = \frac{\rho UL}{\mu} \quad (2.1)$$

where ρ is the density of the flow, U is the flow velocity, L is the model-dependent characteristic length, and μ is the dynamic viscosity.

As mentioned above, the Reynolds number provides insight into the relative influences of the inertial and viscous forces. This is summarized by Lienhard [50] in Figure 2.3. At very low Reynolds numbers ($\text{Re} \leq 5$), the viscous forces dominate and the flow is faithful to the shape of the cylinder. The flow can be thought to be undisturbed by the cylinder and this viscous flow is called *Stokes flow* [11]. Increasing the Reynolds number to the range of $5 \leq \text{Re} \leq 45$, the flow has more inertia, and the viscosity of the fluid can no longer keep it attached. The flow is separated from the back of the cylinder and the shear layer rolls into two stable vortices with opposite senses on either side of the center line.

As the Reynolds number is increased, the influence of the viscous forces is reduced considerably, and these vortices grow in size [19]. This can be seen in the second diagram in Figure 2.3. As these vortices grow in size, they become unstable [19, 44] and they break away from the proximity of the cylinder into the wake [19, 38]. This occurs in the range $40 \leq \text{Re} \leq 150$. The wake enters a state of periodic vortex shedding where vortices of opposite sense are alternately shed into the wake. This pattern is called the *von Kármán Vortex Street*, named after the aerodynamicist Theodor Von Kármán who studied and analyzed this pattern [11]. Roshko [57] noted that in the range $150 < \text{Re} < 300$ the shed vortices transition to becoming turbulent. Increasing the Reynolds number in the range $300 < \text{Re} < 1.5 \times 10^5$ we see that the vortex street is now fully turbulent, with the shedding being strong and periodic [10, 19]. This range is called *subcritical*. $1.5 \times 10^5 < \text{Re} < 3.5 \times 10^6$ is called the *transitional* range of Reynolds numbers. In this range, the boundary layer on the cylinder becomes turbulent and the separation points move aft. This causes a reduction in drag and additionally three-dimensional effects affect the periodicity of vortex shedding. For Reynolds numbers that are greater than 3.5×10^6 the boundary layer is fully turbulent and vortex shedding is re-established [19, 11].

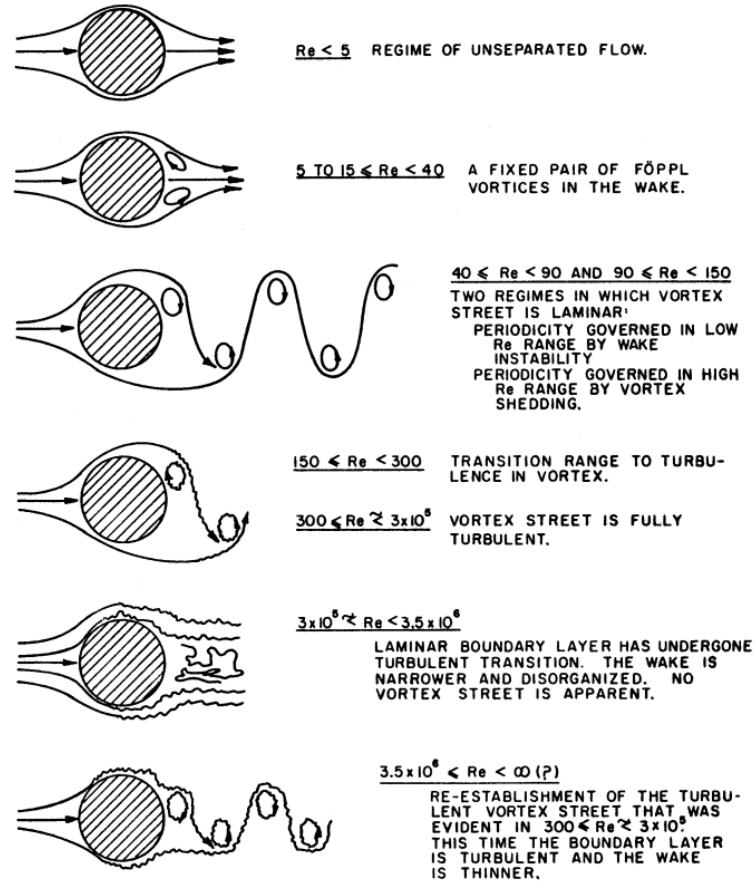


Figure 2.3: The regimes of vortex shedding across a smooth cylinder [19, 50]

2.1.2. Strouhal Number

Like the Reynolds number of the previous section, the Strouhal number is given as:

$$St = \frac{f_s D_{cyl}}{V_\infty} \quad (2.2)$$

where f_s is the vortex shedding frequency, V_∞ is the freestream velocity, and D_{cyl} is the diameter of the cylinder.

For a stationary cylinder, the Strouhal number is a function of the Reynolds number (See Figure 2.6) and to some degree is related to the surface roughness and the freestream turbulence [19]. In the transitional range of the Reynolds number, smooth surface cylinders have a Strouhal number of ≈ 0.5 , on the other hand, rougher surfaces have a Strouhal number is ≈ 0.2 [19].

2.2. Flow Induced Vibrations

FIVs are a complex phenomenon that has fascinated researchers and been studied extensively. Although in some cases they can be undesirable and dangerous if not understood correctly in the design phases [24]. In the case of the cylinder, when there is periodic vortex shedding, the vortices create a force on the structure. In turn, the structure creates a force on the surrounding fluid [19], coupling of the solid and fluid media. FIVs are studied broadly under the field of aeroelasticity as it involves the interplay of aerodynamic, elastic, and inertial forces. FIVs are

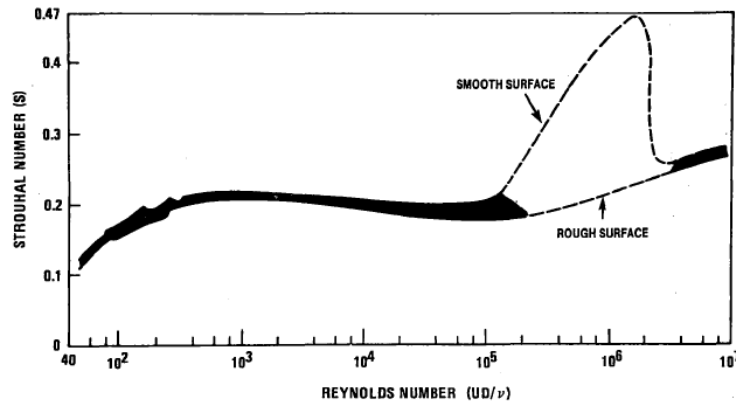


Figure 2.4: The relationship between Strouhal and Reynolds number for circular cylinders [19, 50]

fundamentally forced vibrations whose responses can be categorized based on the speed of the flow. VIV and buffeting are characterized by their low speeds of operation. However, they are limited to an operational window of the natural frequency of the bluff body causing the vortex shedding. On the other hand, galloping and flutter are limit-cycle oscillations and occur at higher flow speeds.

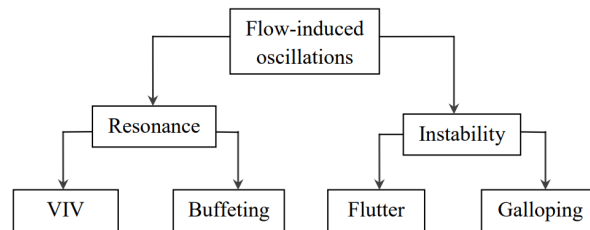


Figure 2.5: Characterization of FIVs [13, 69]

This force on the structure manifests itself into transverse oscillations on the cylinder with a frequency that is close to that of the vortex shedding. The resulting effects of this coupling can [19]:

- Increase the vortex strength
- Increase the spanwise correlation of the shed wake
- Create a resonance between the shedding frequency and the vibration frequency of the cylinder. This phenomenon is known as *lock-in*.
- Cause increase in drag of the structure
- Influence the phase of the vortex shedding

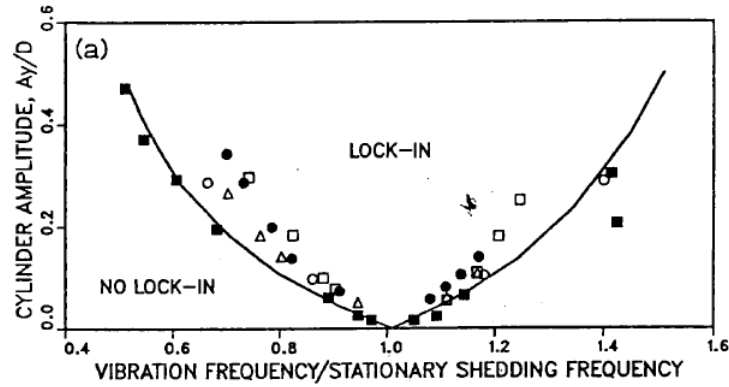


Figure 2.6: Lock-in bands for the resonance of the vortex shedding and transverse oscillations [19]

Thus the possibility of lock-in can influence the wake of the cylinder by increasing the spanwise correlation. This leads to larger amplitude transverse oscillations which in some applications can be destructive to the structure [19]. This has motivated researchers to consider different techniques to understand and control not only the processes of vortex shedding but also the lock-in phenomenon [45]. As a result, there has been significant research in developing active (external energy input) and passive (no energy input) control to modify or suppress the vortices. Ultimately, these modifications involve introducing a solid body of some form into the wake [22]. Passive techniques such as a splitter plate, rods, base bleeds, roughness, and helical strakes are relatively less complicated and are used for flow control applications widely [8]. Some of these passive methods can be seen in Figure 2.7.

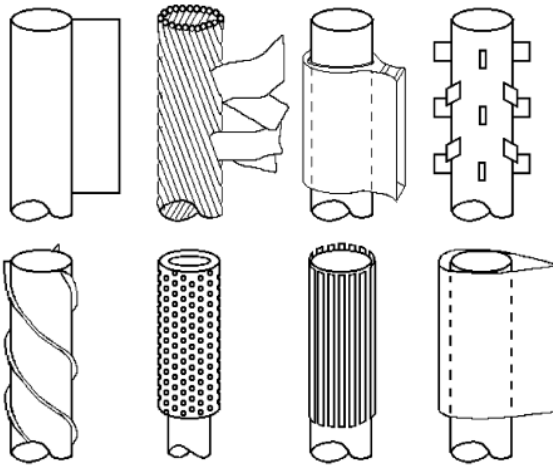


Figure 2.7: Various methods of vortex suppression [46, 19]. *Top Row, Left to right:* Splitter Plate, Ribbons, Pivoted Guiding Vane, Spoiler Plates. *Bottom Row, Left to right:* Helical Strakes, Shroud, Axial Slats, Streamline fairing.

In specific, a cylinder-splitter plate is a cylinder with a two-dimensional surface that is mounted in the wake centerline in a direction that is parallel to the flow to [45]. Splitter plates have been found to be useful in curbing VIV in undersea cables [43], representative of the flag flutter problem [82]. The rest of this chapter is dedicated to understanding the cylinder-splitter plate configuration and its associated phenomena.

2.3. Splitter Plates

As detailed in the previous section, the cylinder experiences different types of flow across a range of Reynolds numbers (attached, periodic vortex shedding, separated flow). Consequently, this causes FIVs in the cylinder. Significant effort has been put into controlling and mitigating these vibrations. A categorization of the research areas is listed in Figure 2.8. The strategies are broadly classified as active (when external energy is input) and passive (when there is no external energy input). Additionally, active control strategies can be open-loop or closed-loop. Choi et al. [26] call geometrical modification in the spanwise direction as three-dimensional forcing, and two-dimensional forcing when it is not. The controls can be further classified based on whether they influence the boundary layer or change the wake characteristics.

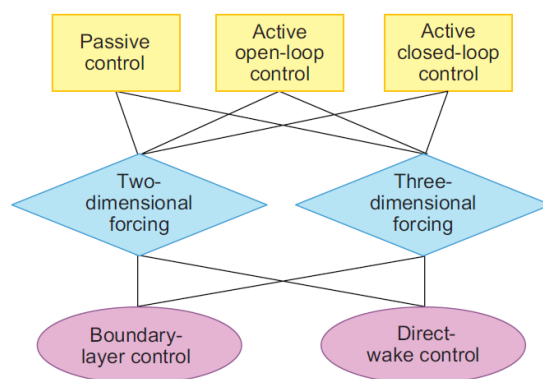


Figure 2.8: Classification of control methods for flow over a bluff body [26].

The *splitter plate* is a type of passive direct wake control device. The splitter plate is typically a two-dimensional plate that is mounted along the wake center line. The splitter plate may be attached to the base of the cylinder or maybe downstream [45, 26]. It was Roshko [57, 58] who first studied the issue of vortex shedding and wake manipulation. He argued that manipulating the vortex formation should strongly affect the base pressure. He was able to test this by using a splitter plate attached to the cylinder. While Gerrard [39] studied the mechanics of the formation region of vortices behind a bluff body by using a splitter plate.

Despite the advantages of simplicity, one of the disadvantages of a splitter plate is that it is sensitive to the direction of the flow [26]. However, this can be solved by using an omnidirectional or freely rotating splitter plate as shown by Cimbalá et al. [27]. Additionally, the splitter plate has found use in drag reduction [12], energy extraction [9, 67], nuclear reactors [24], and serves as a benchmark case for numerical aeroelasticity [31].

2.3.1. Key Parameters of a Splitter Plate

In order to describe the effects of the splitter plate, it is first important to understand the geometric parameters. In order to do this, the geometric description from De Nayer et al. [31] will be used. This can be found in Figure 2.9. For the sake of simplicity, the key parameters are summarized in the table below:

The diameter of the cylinder D_{cyl} determines the Reynolds number of the flow, while the length of the splitter describes how far into the wake the splitter plate extend. The width of

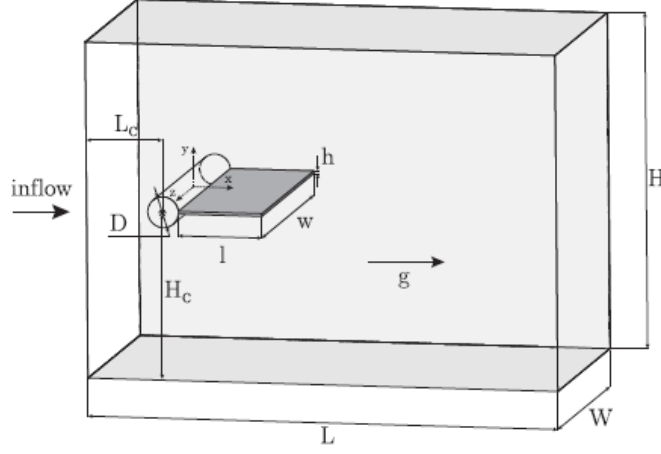


Figure 2.9: The geometric configuration of a cylinder with an attached splitter plate [31]

Table 2.1: Important parameters of the splitter plate

Symbol	Parameter
Geometric	
D_{cyl}	Diameter of the cylinder
L_{sp}	Length of splitter plate
W	Width of the splitter plate
T	Thickness of the splitter plate
Material Properties	
ρ_{sp}	Density of the splitter plate
E	Young's Modulus
ν	Poisson Ratio

the splitter plate can also be understood as the height, i.e the span of the splitter plate along the cylinder length. The thickness of the splitter plate is an average value for the entire length of the splitter plate. The thickness is used to homogenize the manufacturing imperfections of the material. Here, it is also important to define a non-dimensional ratio that relates the splitter plate length to the diameter of the cylinder. This is given as:

$$L/D = \frac{\text{Splitter plate length}}{\text{Diameter of Cylinder}} = \frac{L_{sp}}{D_{cyl}} \quad (2.3)$$

Most of the literature is organized based on different L/D ratios, as the length of the splitter plate is the most critical factor in the cylinder wake modification. This will be addressed in more detail in the following sections. Additionally, the material of the splitter plate has been a topic of research, with plastic sheets [66] and natural rubber [31] being a few choices. The most important material properties are thus the density of the splitter plate, Young's modulus, and the Poisson ratio. Young's modulus is a mechanical property that is defined by the ratio of the axial/compressive stress (σ) and the resulting strain (ϵ), while the Poisson ratio is the ratio of the transverse elongation ($d\epsilon_{trans}$) caused due to axial compression ($d\epsilon_{axial}$). This is given as:

$$E = \frac{\sigma}{\epsilon} \quad \nu = -\frac{d\epsilon_{trans}}{d\epsilon_{axial}} \quad (2.4)$$

2.3.2. Types of Splitter Plates

The splitter plates come in various shapes and sizes. However, they can be broadly classified based on how they respond to the pressure fluctuations in the wake, which are:

- Rigid
- Permeable
- Flexible

Rigid Splitter Plate

A rigid splitter plate is a type of splitter plate that is not deformed by the flow, at the same time, it does not allow any communication between the shear layers across it. This can be seen in Figure 2.10 (a) where the splitter plate is attached to the leeward side of the cylinder and the flow does not deform it. It is important to note that a rigid splitter plate has also been studied with a hinge at the base. In this case, the splitter plate is free to oscillate with the flow variations, however, is still not locally deformed. This configuration will be referred to as a hinged rigid splitter plate [66, 27, 15].

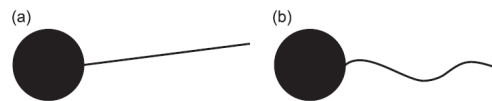


Figure 2.10: Types of splitter plates (a) Rigid Splitter Plate (b) Flexible Splitter Plate [66]

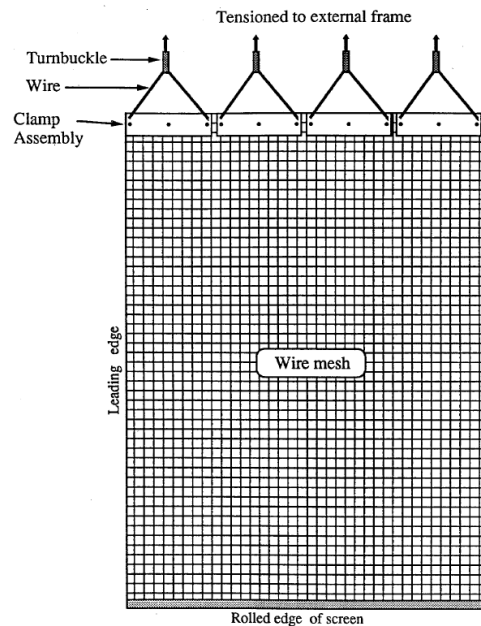


Figure 2.11: A wire mesh 'permeable' splitter plate used by Cardell [22]

Permeable Splitter Plate

The permeable splitter plate was studied by Cardell [22] in his thesis. In his study, he defined the permeable splitter plate as one that interferes with the communication of the shear layers, however, by varying the permeability the magnitude of the interference can be regulated [22].

In his study, Cardell [22] uses a splitter plate that is made out of thin perforated metal or a wire mesh screen. This can be seen in Figure 2.11. This is done so to minimize the geometrical effects. The communication takes place in the form of the transverse velocity component and the changes in the pressure fields. Assi et al. [14] also studied a variation of a permeable splitter plate in which they used a spanwise slotted splitter plate.

Flexible Splitter Plate

A fully flexible splitter plate is one that is free to deform along the length of the splitter plate. Thus, the vortices shed from the cylinder cause vibrations along the length of the plate. This allows for more use cases apart from vortex modulation. One of the important ones is for the purpose of energy harvesting as studied by Allen et al. [9] and Taylor et al. [68] by utilizing piezoelectric materials. The vibration amplitude of the plate is characterized by the unsteady loading caused by the vortex shedding. The flexible splitter plate can be visualized in Figure 2.10 (b) where pressure and viscous shear stress variations locally deform the plate in the wake. On the other hand, the vibration frequency is a combination of the vortex shedding frequency and the naturally occurring frequency of the flexible plate [47]. The shedding frequency depends on the Reynolds number of the flow while the natural frequency depends on mechanical properties such as Young's modulus and geometric properties such as length [47]. Due to the local deformations, the splitter plate has complex aeroelastic interactions with the flow. Due to this reason, experiments with flexible splitter plates have been insufficient [47, 48]. The flexible splitter plate will be the focus of this study due to understanding its wake dynamics for the application of energy harvesting, as discussed in the previous chapter.




2.4. Types of Instabilities for Splitter Plates

FIVs with flexible splitter plates can be classified based on the type of excitation. These are:

- Instability - Induced Excitation (IIE)
- Movement - Induced Excitation (MIE)
- Extraneously - Induced Excitation (EIE)

Yu et al. [82] use this classification in explaining the dynamics of three configurations of flexible flags or splitter plates (inverted flag, standard flag, and flag behind a bluff body). Essentially, these configurations are differentiated by their boundary conditions. This can be seen in Figure 2.12.

The IIE is associated with the vortex-shedding mechanism of an inverted flag. An inverted flag is when the trailing edge of the flag is fixed, while the leading edge is free to vibrate. The vortex dynamics of the periodic vortex shedding of the leading and trailing edge cause large amplitude deformation of the flag. As a result of this, the vibrations are self-controlled [82]. The vibration dynamics of a standard flag are a result of MIE. This occurs as a result of a feedback loop between the internal, elastic, and fluid (aeroelastic) forces. The fluid load on the flag undergoes more displacement as it tries to achieve an optimal energy exchange between the structural and fluid domains. In aerospace engineering, this is often termed as *flutter* [82]. A flag that is driven into motion by fluctuations in pressure produced upstream is known as an EIE. This is generally related to the vortex shedding from a bluff body. In this case, a circular cylinder [82]

Main source of excitation	Instability-induced excitation (IIE) *	Movement-induced excitation (MIE)	Extraneously Induced excitation (EIE) *
	Inverted flag	Standard flag	Flag behind bluff body
Flag configuration			
Nature of vibration	Self-controlled vibration	Self-excited vibration	Forced vibration

* Self-excited vibrations (due to MIE) can also be observed if the conditions for fluid-elastic instability are reached.

Figure 2.12: The categorization of the different sources of excitations [82]

2.5. Effect on Vortex Shedding and Formation

The insertion of the splitter plate in the flow causes the formation region to grow in length. This causes the Strouhal number to decrease. The splitter plate will also disrupt the communication between the shear layers and some of the cross-flow may be deflected away from the wake. The overall physical effect is that the shedding period may increase. The circulation at the base of the cylinder is also affected by the splitter plate. The presence of the plate may result in the weakening of the vortices in the formation stage decreasing frequency. Although, Gerrard [39] notes that this effect may be small. Wu et al. [79] studied a flapping plate numerically. They also confirm the findings of Gerrard [39] with regard to the elongation of the formation region slowing down the vortex shedding. Additionally, Wu et al. [79] in their simulations observed a secondary vortex on the edge of the splitter plate. This vortex had a sign opposite to that of the main cylinder-produced vortex. They also note that the strength of this secondary vortex was not strong enough to alter the main vortex of the cylinder. However, this was true for small angles of splitter plate flapping. For larger angles, they found either a constructive or destructive interaction between the secondary vortex and the primary vortex. Wu et al. [80] also studied this effect numerically with an undulatory (flexible) plate. Constructive interference occurs when the primary and secondary vortices have the same sense. In this case, the circulation is increased which also leads to an increase in drag. On the other hand, destructive interference occurs when the two vortices have the opposite sense and cancel each other out.

This observation can be seen in Figure 2.13. The figure shows the vortices involved in one cycle of the splitter plate. In the upstroke of the splitter plate, the plate produces a counterclockwise vortex, and the cylinder produces a clockwise vortex. In the next time interval, the plate vortex ($P1$) is detached and interacts with the cylinder vortex ($C1$). Wu et al. [80] attribute this due to the traveling wave along the plate which facilitates the movement of the primary vortex. In the downstroke of the splitter plate, the interacting vortex ($S1$) is shed into the wake and a clockwise vortex forms at the plate. The authors concluded that the motion of the flexible splitter plate serves to weaken the primary cylindrical vortex while controlling the wake width.

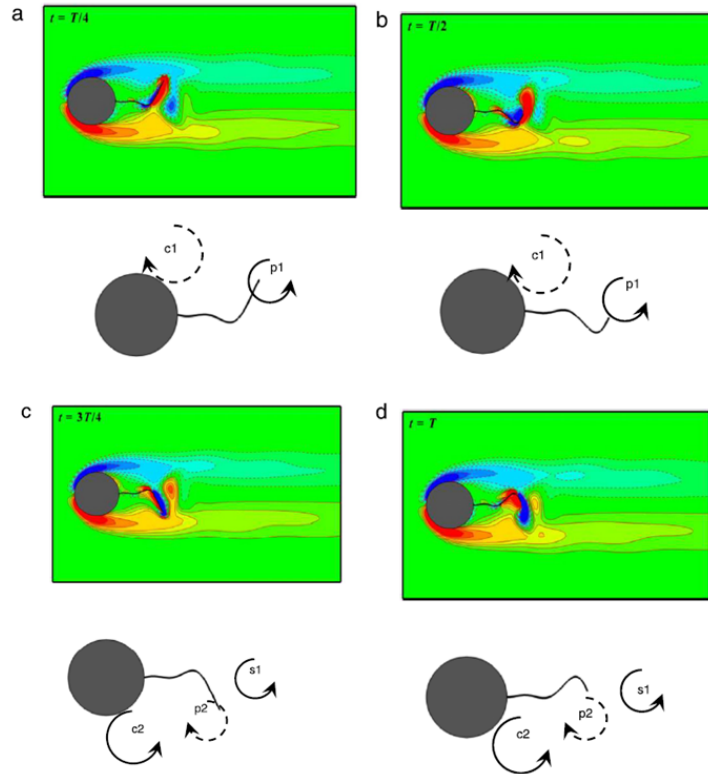


Figure 2.13: Development of the secondary vortex over one oscillation cycle of the splitter plate. Reproduced from Wu et al. [80].

2.6. Effect of Plate Length

In order to understand the influence of the splitter plate length on the wake characteristics, we refer to two important studies performed by Apelt et al. [12] and Anderson et al. [10].

Apelt et al. [12] performed an experimental evaluation of the flow past a circular cylinder with different-length splitter plates. These experiments were performed in the Re range of $10^4 < Re < 5 \times 10^4$. They studied the variation of the Strouhal number compared to an increase in the splitter plate length. We can see this in Figure 2.14, where the Strouhal number initially increases with the length of the splitter plate. The value of the Strouhal number then drops as the L/D ratio approaches 1. After this, the Strouhal number further increases with an increase in the length of the splitter plate.

Additionally, they studied the influence of the splitter plate on the wake width. They found that the short splitter plates reduced the wake width, as compared to a plain cylinder. A further increase in length reduced the wake width. However, splitter plates with L/D ratios closer to 2 saw an increase in the wake width. They also noted that short plates produced relatively linear wakes, and longer plates produced a wake with curvature. Figure 2.15 shows the effect of the splitter plate length on the vortex formation region. Fig 10 (a) shows that the vortex formation region of a plain cylinder is right behind it, as the shear layers roll up and are ejected into the wake. For very short plates shown in Fig 10 (b), The shear layers roll up at the edge of the plate. The longer plates cause the vortex to form at a distance from the plate before being ejected into the wake. For longer plates it can be seen that the vortex is

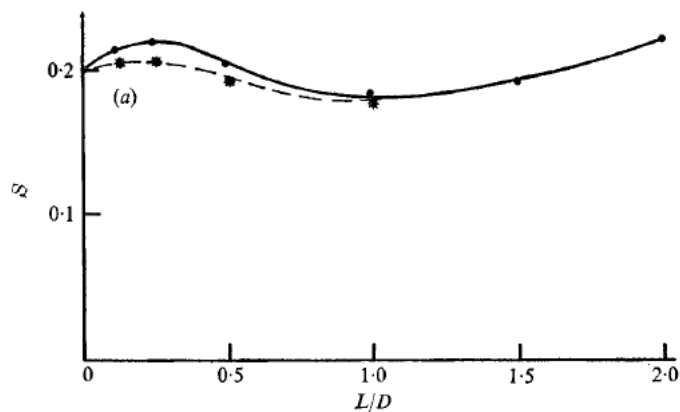


Figure 2.14: Variation of Strouhal number with L/D ratio [12]. The * markers are measurements from hot-wire anemometry while the solid circle markers are from film.

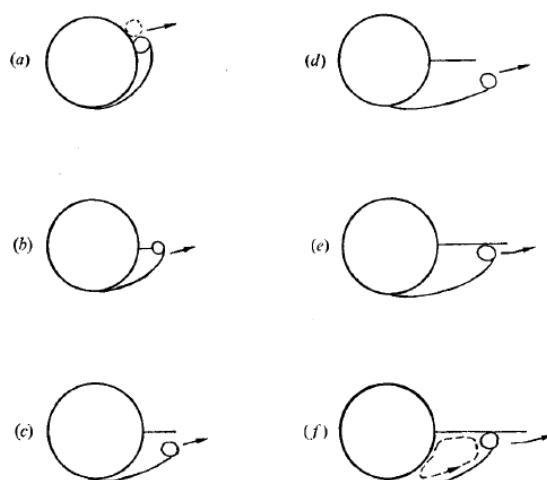


Figure 2.15: Vortex formation for a plain cylinder and splitter plate of different lengths. [12]. (a) Plain Cylinder, (b) $L/D \leq 1/4$, (c) $L/D = 1/2$, (d) $L/D = 1$, (e) $L/D = 1.5$, (f) $L/D = 2$

being formed on the splitter plate before being released into the wake, this also explains the double curvature wake observed by the authors. Furthermore, the authors also noted that the vortex formation position was essentially the same once the L/D ratio exceeded 1.

Anderson et al. [10] also studied the effects of the splitter plate length on the wake and vortex formations. In their study the authors determined four regions namely:

- *Region I:* Stabilization Region (L/D : 0 to 0.25)
- *Region II:* Shear Layer Elongation Region (L/D : 0.25 to 0.75)
- *Region III:* Reduced Entertainment Region
- *Region IV:* Splitter Plate Vortex Interaction Region

Region I extended for the $L/D = 0 - 0.25$. In this region, the Strouhal number increases, this is also in line with the observations of Apelt et al. [12]. The short splitter plates are able to reduce the amplitude of oscillations compared to a plain cylinder. This causes a reduction of

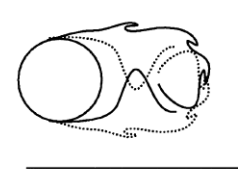
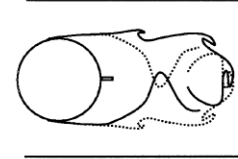
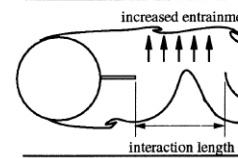
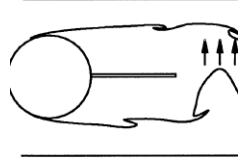
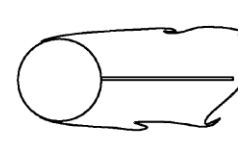
	<p>No splitter plate, $l/D=0$</p> <ul style="list-style-type: none"> o With no splitter plate the shear layers 'flap' in-phase with the Kármán shedding. (dashed lines indicate second shedding cycle.) o Relatively large momentum thickness. o Strouhal number constant at approx. 0.20.
	<p>Region I - Stabilizing region, $l/D < 0.25$</p> <ul style="list-style-type: none"> o Splitter plate lessens transverse oscillation of shear layer. o Decrease in momentum thickness. o Increased strength of shear layers facilitates their interaction. o Progressive increase in St with l/D.
	<p>Region II - Elongation region, $0.25 < l/D < 0.75$</p> <ul style="list-style-type: none"> o Large shear layer interaction length allows increased entrainment which reduces the strength of the shear layers and inhibits their interaction. o Progressive increase in formation length with l/D. o Progressive decrease in St with l/D.
	<p>Region III - Reduced entrainment, $0.75 < l/D < 1.5$</p> <ul style="list-style-type: none"> o Formation length remains relatively constant. o Interaction length decreases although it remains larger than the no splitter plate case. o Progressive increase in St with l/D.
	<p>Region IV - Splitter plate-vortex interaction region, $l/D > 1.5$.</p> <ul style="list-style-type: none"> o Shear layer interaction length becomes smaller than it was in any of the previous regions including $l/D=0$. o progressive decrease in St with l/D.

Figure 2.16: A summary of the effects of the splitter plate length from Anderson et al. [10]

momentum thickness of the boundary layer as evidenced by the phase-averaged experimental measurements. The splitter plate configuration also produced stronger shear layers which increases their interaction downstream. According to Gerrard's [39] model, this would increase the shedding frequency. The results also pointed to this phenomenon as the enhanced shear layers diffused the vorticity by means of increased oscillations in the flow. In Region II, the shear layer is elongated, and as a consequence, there is increased entrainment. The effect of increased oscillation in Region I is now not as effective. Region II is in the L/D range of 0.25 to 0.75. The elongation of the shear layers causes more communication between them, and more flow with the opposite vorticity is allowed to mix. As a consequence, the diffusivity is increased decreasing the shedding frequency. In Region III, the entrainment region is reduced, causing the vortex shedding to increase as the diffusivity has also reduced. This region is applicable for splitter plates of L/D ratios between 0.75 to 1.5. Region IV represents all L/D ratios greater than 1.5. In this region, the interaction length is the shortest with the least communication between the two shear layers. As a result, the shedding frequency is reduced with increasing splitter plate length. This was found to be consistent with the results of Apelt et al. [12].

2.7. Kinematics of a Splitter Plate

Shukla et al. [66] studied the kinematics of a flexible splitter plate that was in the wake of a circular cylinder. They used experimental methods (laser sheets and CCD camera) in a water tunnel. They investigated the behavior of the splitter plate in the flow Reynolds numbers of $Re \approx 1800 - 10,000$. For the splitter plate, they used a plastic sheet that was $40\mu\text{m}$ thick. To prevent the splitter plate from collapsing under its own weight, stiffeners were placed at regular intervals. The results discussed are for an L/D ratio of 5 and the flexural rigidity of

the plate was 3.96×10^{-6} Nm. Lastly, he uses non-dimensional amplitude and frequency of the splitter plate motion respectively. This is given as:

$$A^* = \sqrt{2}y_{rms} \quad f^* = fD/V_\infty \quad (2.5)$$

In their experiments, Shukla et al. [66] found that at low Reynolds numbers the amplitude of vibration was low. The amplitude increases slowly with an increase in Re. The amplitude then drops after reaching a local maximum at $Re = 2500$. The amplitude then increases in magnitude with increasing Re, until it saturates at Re values greater than 6000. They [66] further identify three distinct regions of oscillations based on periodicity. *Region (a)* is periodic oscillations at low Re values, *Region (b)* is a range of Re values when the oscillations of the plate are non-periodic. Finally, there is a *Region (c)* at high Re values, where the plate again resumes its fairly periodic motion. This is highlighted clearly in Figure 2.17. As a result, they also call Region (a) as *Mode I* and Region (c) as *Mode II* of vibration. They also found that the normalized tip frequency was approximately 0.2 in the periodic regimes of Mode I and II. While in the non-periodic region, it was found to be lower at approximately 0.15. The non-periodic regime is made up of multiple f^* values which account for the behavior in the regime. The authors suggest that this could be due to two competing modes. Lastly, the authors also found that in Mode I and II, the non-dimensional phase speed of the splitter plate was similar to that of the convection speed of the shed vortices [66].

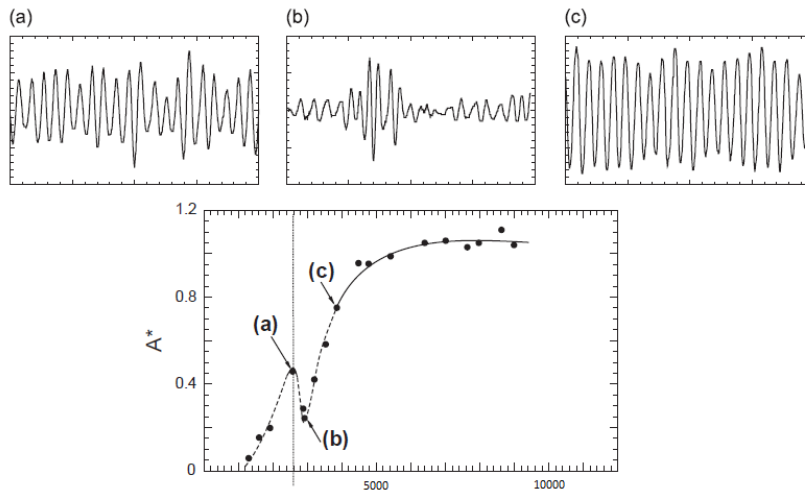


Figure 2.17: Amplitude of the flexible splitter plate from Shukla et al. [66]. Additionally the sub-figures (a), (b), and (c) highlight the periodicity of the regions being discussed.

De Nayer et al. [31] conducted an experimental benchmarking test for numerical FSI validation. Specific details of the experiment can be found in their research article. They performed their test in a water tunnel with $Re = 30,470$. The splitter plate was made out of rubber with an L/D ratio of ≈ 2.72 . In the course of their experiments, they performed some preliminary tests to work out the best working conditions for reproducible numerical models. They were able to detect four regimes:

1. The first regime is when the flow velocity is less than or equal to 0.4 m/s. In this regime, the structure has minimal displacement and is disturbed by turbulent fluctuations of

the flow itself. In line with the previous section, the splitter plate undergoes the EIE mechanism.

2. In the second regime, the flow velocity lies between 0.4 m/s and 1.65 m/s. The splitter plate motion is quasi-two-dimensional that is driven by the IIE mechanisms discussed in the previous sections. These fluctuations become correlated as they approach the resonance frequency (*lock-in phenomenon*). Oscillations with large amplitude are to be expected in the first swiveling mode.
3. The third regime is dominated by splitter vibrations that are chaotic and three-dimensional. This regime is seen in the flow velocity region of 1.65 m/s to 2.33 m/s. In the study, they found it difficult to measure the interaction frequency due to chaotic interactions.
4. The fourth regime is made up of velocities greater than 2.33 m/s. The deformations of the splitter plate are now fully three-dimensional with several modes of vibration superimposed over one another.

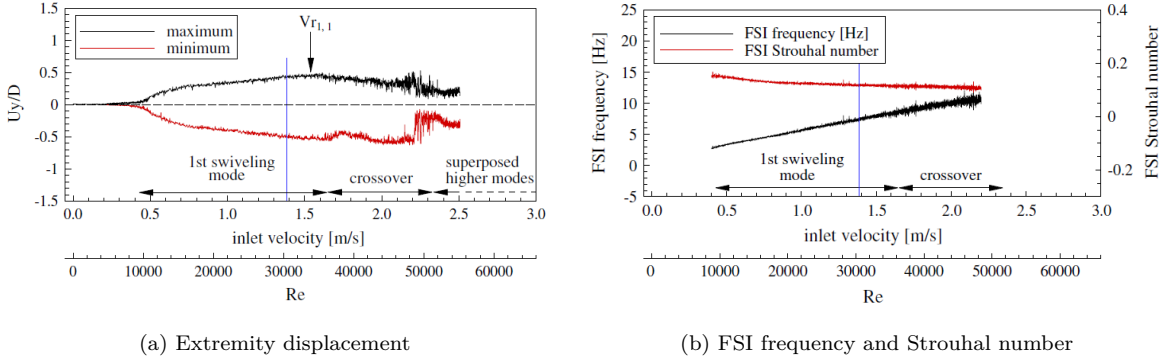


Figure 2.18: Experimental Measurements by De Nayer et al. [31].

Figure 2.18 shows the experimental measurements of De Nayer et al. [31] depicting the extreme measurements of the splitter plate, frequency of splitter plate motion, and the Strouhal number. Figure 2.18a shows the displacements of the structure extremities, this reflects the observations of splitter plate deformations from Regimes I, II, III, and IV. While Figure 2.18b shows the first swiveling mode that then crosses over to multiple modes of vibration.

2.8. Effect of Non-Dimensional Bending Stiffness

Flexural rigidity (EI) can simply be defined as the resistance of a structure to bending. Shukla et al. [66] studied the effect of varying the flexural rigidity on the splitter plate deformations. They consider three values with $EI = 3.96 \times 10^{-6}$ Nm as the baseline flexural rigidity. The second EI value is roughly 3 times the baseline, and the third case is approximately 3 times the second [66].

Figure 2.19a, we can see the effects of increasing the flexural rigidity. The non-dimensional amplitude is calculated as per equation 2.7. The base case is marked with filled circles, while the second and third variations of EI are marked with hollow circles and triangles respectively. By increasing the EI from the baseline once, we can see that the position of Mode I (from the previous section, which refers to the regions of periodic splitter plate motion) has been shifted

to a higher Reynolds number. This indicates there is an inherent relationship between flexural rigidity and flow velocity. At this point, the authors introduce the non-dimensional bending stiffness [28, 66] which relates the flexural rigidity to the load due to dynamic pressure on the splitter plate.

This can be quantified as:

$$K^* = \frac{EI}{0.5\rho V_\infty^2 L^3} \quad (2.6)$$

where K^* is the non-dimensional bending stiffness, ρ is the freestream density, V_∞ is the velocity of the flow, and L is the length of the splitter plate. As expected, at low flow speeds or Reynolds numbers, the value of K^* is very high, while at higher flow speeds, the value decreases. Figure 2.19a can be now replotted considering the non-dimensional bending stiffness, as seen in Figure 2.19b. This form of representation offers a more intuitive understanding of the splitter plate as the different flexural rigidity values essentially are lumped into a single representative curve. Shukla et al. [66] argue that at lower K^* values (i.e. higher velocities), there exists more communication of the shear layers arising from the cylinder. This causes a larger amplitude of oscillations. On the other hand, higher values of K^* indicate a more rigid splitter plate that reduces the communication and consequently the amplitude of oscillation.

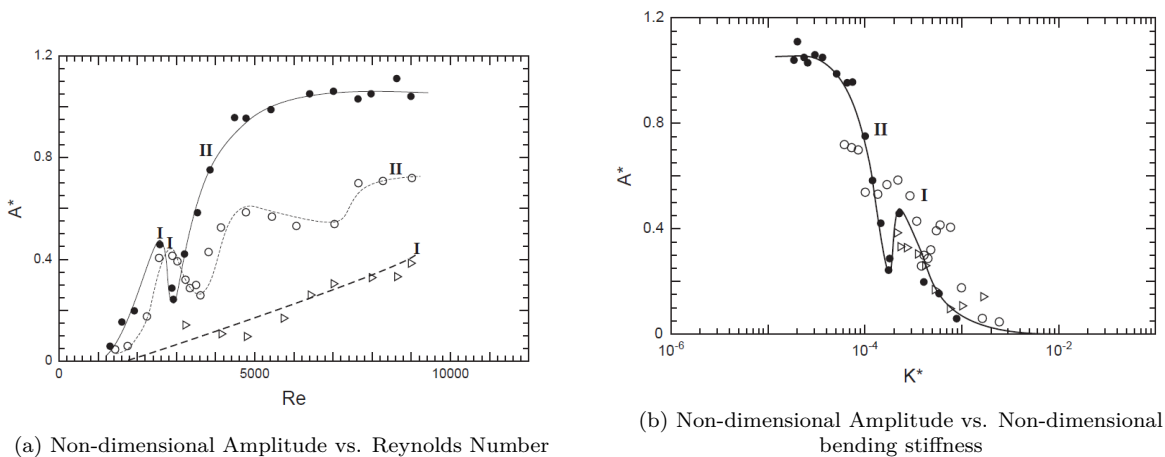


Figure 2.19: Experimental results of Shukla et al. [66] highlighting the effect of the flexural rigidity on the motion of the splitter plate. The non-dimensionality of the amplitude has been defined in Equation 2.7

2.9. Energy Harvesting Using a Splitter Plate

For a circular cylinder, the harvesting can occur in a narrow wind speed range of the VIVs but is immune to galloping [67]. Significant research has gone into developing mechanisms that modify the flow physics in order to eliminate the upper bound of the cut-in velocity range and improve the efficiency of the harvester [69]. The modification under consideration is of course the splitter plate.

Song et al. [67] studied the performance of such a splitter plate attached to a cylinder. The acrylic splitter plates were attached in the wake of the cylinder along with the piezoelectric layer. The experimental set-up is highlighted in Figure 2.20a. Through their experiments, they found that the attached splitter plate altered the vibration behavior by eliminating the upper bound of the workable range of VIV. It can be seen that for a bare cylinder, the velocity

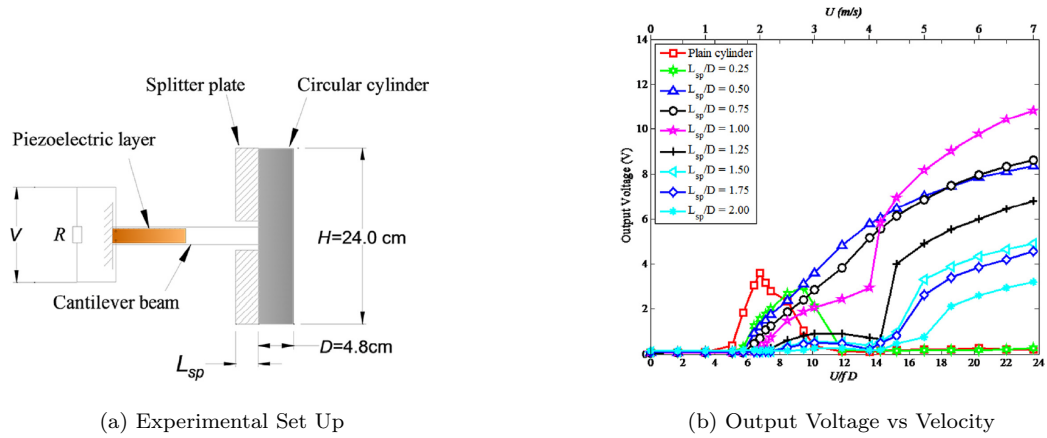


Figure 2.20: Results of the use of splitter plate for energy harvesting [67]

range is approximately between 1-3 m/s. Beyond this, the output voltage is zero. However, the addition of a significantly long splitter was found to remove the upper bound as the output voltage increased with an increase in velocity.

Akaydm et al. [7] studied short-length piezoelectric beams in the wake of a circular cylinder at high Reynolds numbers. In their study, they found that flow greater than a Reynolds number of 10,000 provided an opportunity for energy harvesting as the wake structures were coherent in spatial and temporal scales. Allen et al. [9] studied the feasibility of using a piezoelectric membrane in a so-called 'eel' setup. The membrane was in the wake of a bluff body and subject to periodic vortex shedding by the body. Additionally, they concluded that the membrane was able to function as a voltage source and also defined the requirements for optimal coupling of the membrane and the flow.

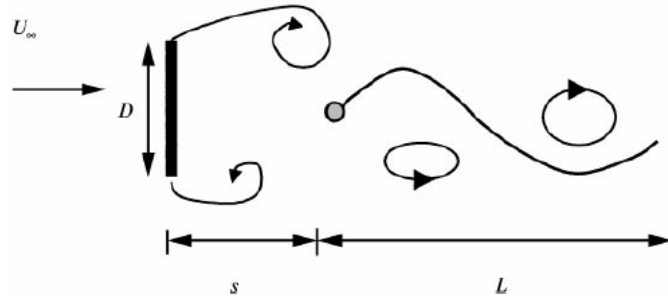


Figure 2.21: Geometry of the oscillating 'eel' membrane in the wake of a bluff body, studied by Allen et al. [9]

Such modifications to conventional vortex shedding have the potential to enhance energy harvesting. Such devices find use in powering solitary sensors and or low-consumption devices such as street lights. They also have potential applications in distributed energy networks. Despite all the advantages that energy harvesting presents there are still plenty of challenges to be overcome. One of the pressing challenges restricting the growth of these devices is the fact that theories surrounding FIVs have not matured yet. Additionally, there is a need to study and understand mechanisms in complex flow conditions and around bluff bodies [69].

2.10. Research Gap

The review study from Wang et al. [69] highlighted the fact that the barrier to the further development of energy harvesters is that the flow mechanisms of complex flow conditions have not been fully understood. Additionally, most flow mechanisms have been investigated in two dimensions with very little literature discussing the three-dimensional effects of the splitter plate.

Thus a study of the wake dynamics of a flexible splitter plate by using advanced PIV techniques can serve to expand on the existing knowledge in this field and help bridge the knowledge gap.

2.11. Research Goal

As touched upon in the introduction, the main goal of this thesis is to:

"To characterize the mechanisms and wake dynamics of a cylinder and flexible splitter plate configuration using a Lagrangian Particle Tracking experiment."

To achieve the main objective can be broken down into several sub-goals, which include:

- Performing a literature study to establish the historical context and the knowledge gained from other research work.
- Performing a preliminary analysis using cameras to ascertain the different flow regimes.
- Performing a 4D-PTV measurement of the cylinder and flexible splitter plate as well as the bare cylinder itself to obtain time-resolved experimental data.
- Statistical analysis of the generated experimental data sets and generating relevant results to answer the research questions, which are designed to fulfill the research goal.

The details of the LPT experiment and general measurement techniques will be covered in detail in Chapter 3

2.12. Research Question(s)

To achieve the goals set above, the thesis aims to answer the following research questions:

- **What is the influence of the flexible splitter plate on the wake dynamics when compared to a bare cylinder?**
 - How does the flexible splitter plate affect the vortex shedding frequency of the cylinder?
 - What energy modes are dominant in the flow?
 - Is the motion of the splitter plate coupled with the flow?
 - How does the splitter plate affect the coherence of the near wake spanwise vortex shedding of the cylinder?
 - How do the wake dynamics and FSI mechanisms change with the freestream Reynolds number?

- **Can the behavior of the flexible splitter plate be characterized into distinct aeroelastic regimes based on their wake dynamics?**
 - If so, what are the wake dynamic distinctions between each regime?
 - If not, what are the possible reasons for the lack of distinction between each regime?

3

Measurement Techniques

In this chapter the measurement technique that will be employed to perform the experiment will be expanded on. The working principles of PIV, Tomographic PIV will be discussed with a special emphasis on Shake-The-Box, a LPT algorithm. Shake-The-Box will be used extensively in this thesis to track particle motion to extract velocity information.

3.1. Introduction

Particle Image Velocimetry (PIV) is a flow diagnostic technique that is used to obtain flow information. This is achieved by the process of seeding the flow with particles that are assumed to be small enough to faithfully follow the flow. The flow is then illuminated and several images are taken using high-speed cameras. Cross-correlation is then performed on successive images to reveal the average displacement. This along with the illumination frequency gives information about the flow velocity [55]. The earliest work in digital PIV was done by Willert et al. [75]. Recent improvements in imaging and computational power have made PIV more accessible and popular with aerodynamic researchers [55]. The advantages of PIV are that it is a non-intrusive measurement technique and gives spatial information about the whole velocity field.

Lagrangian Particle Tracking (LPT) is a PIV technique in which the individual tracer particles are tracked in three-dimensional volume [52] and works with lower seeding densities [55]. Unlike 2D PIV which involves cross-correlation on an interrogation window, LPT algorithms track individual particles. This will be discussed in more detail in this chapter. In particular, an LPT algorithm called Shake-The-Box (STB) will be discussed.

3.2. Working Principles

The PIV system consists of various sub-parts that work cohesively to produce the final processed velocity fields. The seeding system injects into the flow a steady stream of evenly distributed particles. These particles need to faithfully follow the flow. The illumination system consists of lasers and light sheet optics to generate an illuminated region of interest. Another purpose of the system is to illuminate the region with a constant pulse rate (Δt). The imaging system consisting of high-speed cameras and lenses then captures images of the illuminated region in sync with the constant pulse rate. Figure 3.5 shows a typical setup of an experiment that involves the use of PIV. The images are divided into smaller images called interrogation windows. The interrogation windows are then processed using cross-correlation to find average

displacements. Velocity can then be calculated by using the average displacements and pulse width separations.

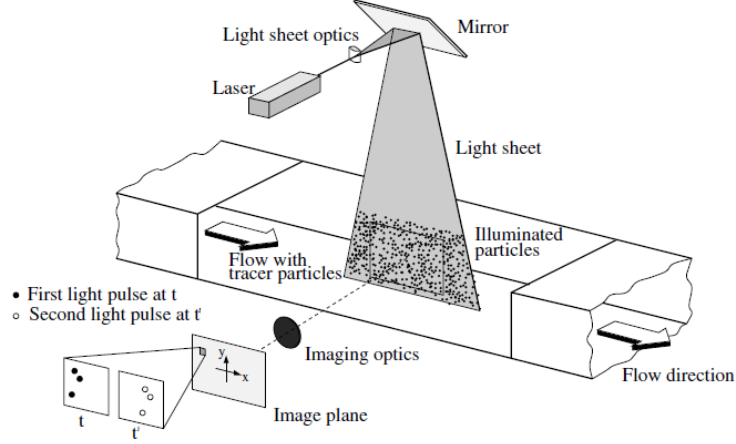


Figure 3.1: Typical set up of an experiment with PIV [55]

3.2.1. Tracer Particles

In PIV, the velocity is not calculated from the flow itself, but from the velocity of particles. Therefore the choice of the seeding particle is an important one. Thus fluid mechanical properties of such seeding particles must be studied [55]. With the right amount of particle density, they can follow the flow faithfully. If the density is too low, then not enough information can be extracted from the flow, and if it is too high, then it starts affecting the flow properties.

An important source of error in tracer particle measurements is the gravitational forces. This error occurs if the density of the air (ρ) and the density of the tracer particle (ρ_p) are not the same. In order to account for the gravitation-induced velocity (U_g), Stoke's law is used. This is given as:

$$U_g = d_p^2 \frac{(\rho_p - \rho)}{18\mu} g \quad (3.1)$$

where g is the acceleration due to gravity, μ is the dynamic viscosity, and d_p is the diameter of the tracer particle. Since Stoke's drag dominates particle physics, a slip velocity can be defined as the difference between the velocity of the particle and that of the freestream velocity.

$$V - V_\infty = d_p^2 \frac{(\rho_p - \rho)}{18\mu} \frac{dV}{dt} \quad (3.2)$$

The seeding particles must also be neutrally buoyant so that the particle can follow a single trajectory over a long distance. This allows for flexibility of particle choice while keeping the particle response time low. This can be quantified by the particle response time, which is given by the following formula:

$$\tau_p = d_p^2 \frac{\rho_p}{18\mu} \quad (3.3)$$

Another requirement for the particle is its ability to scatter the light efficiently when it is illuminated. For spherical particles with a diameter larger than the wavelength (λ) of the laser, Mie's scattering theory is generally applied [55]. This is characterized by a normalized diameter q :

$$q = \frac{\pi d_p}{\lambda} \quad (3.4)$$

The value of q is an indication of the angular distribution of the scattering of light.

3.2.2. Illumination

Since the measurements are taken at a fixed interval of time (Δt), the light source must be suited to such experimental conditions. Additionally, the pulse should be sufficient such that the high-speed cameras do not pick up the particles as elongated streaks. The pulse width can be calculated such that it is appropriate for the tracer particle diameter (d_p), the velocity of the flow (V_∞), and the magnification (M , see 3.2.3). This is given as:

$$\delta t \ll \frac{d_p}{V_\infty M} \quad (3.5)$$

The illumination device should also light up the area evenly such that all the particles in the light sheet are in focus. Additionally, the illumination source should have enough intensity to allow for scattering by the tracer particles.

Lasers are immensely useful in planar PIV and to some extent, tomographic PIV [35] as they have several advantages, the first being that they can emit monochromatic light of high energy density [55]. Additionally, the laser light can be manipulated to form thin sheets, which are then recorded by high-speed cameras. A disadvantage of lasers is that they're expensive, difficult to use, and operated with a trigger delay [76].

Willert et al. [76] studied the use of LEDs in image velocimetry experiments. They concluded that LEDs are a cheaper alternative to the use of lasers and provided sufficient illumination for both air and water experiments. Additionally, the LEDs can be fired instantaneously unlike their laser counterparts.

3.2.3. Imaging

Initially, PIV work was carried out using photographic chemical film [55, 1]. This was quickly replaced by electronic imaging which provided images immediately and avoided the use of photochemical processing of film. The most common electronic sensors that are being used are charged coupled devices (CCD) and complementary metaloxidesemiconductors (CMOS). In addition, CCD sensors have found the most use [55].

As far as the parameters relating to imaging are concerned, the field-of-view (FOV) is a critical parameter that is set at the beginning of the experiment to design the imaging system around it. Field of view defines the region of interest surrounding the model, this is usually set to 1.5 times the characteristic length of the model as a good estimate. Some of the other important parameters in PIV are the focal length, f-number ($f\#$), and image magnification. These are defined as:

$$\frac{1}{f} = \frac{1}{d_i} + \frac{1}{d_o} \quad M = \frac{d_i}{d_o} \quad f\# = \frac{f}{D_{app}} \quad (3.6)$$

where d_i is the image distance, d_o is the object distance, and D is the aperture size. The magnification factor can be defined in a more useful way:

$$M = \frac{\text{sensor size}}{\text{image object size}} = \frac{\text{pxl} \times \text{No of pxl}}{\text{FOV}} \quad (3.7)$$

Another important concept in PIV imaging is focal depth. The focal depth of the imaging system represents the range in which the particles can be observed with sufficient sharpness. This is given by the formula:

$$\delta z = 4.88\lambda(f\#)^2 \left(\frac{M+1}{M} \right)^2 \quad (3.8)$$

3.3. Tomographic Particle Image Velocimetry

Three-dimensionality is an inherent part of fluid mechanics. It is particularly important when there is no specific symmetry in the flow, multiple planes of measurement may be required to describe the flow accurately. Turbulent flow is an example of such an asymmetric flow [35]. PIV is limited to planar measurements where two in-plane components are calculated from the cross-correlation of the tracer particles. In order to get the full picture of the flow, the out-of-plane component needs to be calculated.

A novel approach in three-component PIV measurements was put forth by Elsinga et al. [35] in what is called Tomographic Particle Image Velocimetry (Tomo-PIV). The system works by the tomographic reconstruction of the particles in three-dimensional space. In order to obtain the particles, the illuminated region is recorded simultaneously from multiple viewing directions with cameras similar to PIV [35].

The recorded images from the non-collinear views are then put into a reconstruction algorithm that derives the particle distribution from the two-dimensional images. There are several algorithms that are based on iterative algebraic reconstruction [61]. The main goal of these algorithms is to derive an accurate relation of the particles between the *object space* and the *image space*. In order to do this a calibration procedure is usually carried out at various depths of fields in order to increase the accuracy [72]. The entire Tomo-PIV procedure is shown in Figure 3.2. The figure shows how the measurement volume is illuminated and recorded using cameras from different viewing angles. The recorded image pairs are then subjected to tomographic reconstruction which yields the particle distributions in the measurement volume. A three-dimensional cross-correlation then gives the necessary velocity field. The iterative reconstruction allows relatively high particle image densities, roughly 0.05 ppp [63] using algorithms such as Multiplicative Algebraic Reconstruction Technique (MART) [42], and Simultaneous Multiplicative Algebraic Reconstruction Technique (SMART) [16].

3.4. Helium Filled Soap Bubbles (HFSB)

The classic PIV involves taking measurements in two-dimensional space. However, more information about complex flow features can be extracted by performing PIV in more than two dimensions. As discussed in the previous section, Elsinga et al. [35] showed a novel technique that uses tomographic photography principles to reconstruct tracer particles in a three-dimensional space. Since then, measurement volume for experiments performed has grown from laser sheets to medium ($10 \times 10 \text{ cm}^2$) and larger scales ($50 \times 50 \text{ cm}^2$) [62].

Under the umbrella of PIV technology, optical technology has grown immensely, but laser technology has stayed relatively the same. This is a particular challenge when dealing with medium and large-scale measurements. Additionally, the scattering efficiency is lowered at larger measurement volumes thus affecting the spatial resolution [62]. A possible solution is using larger tracer particles, however, with longer relaxation times they do not represent the flow faithfully [62]. Melling [53], in his study on tracer particles for PIV, showed that if the

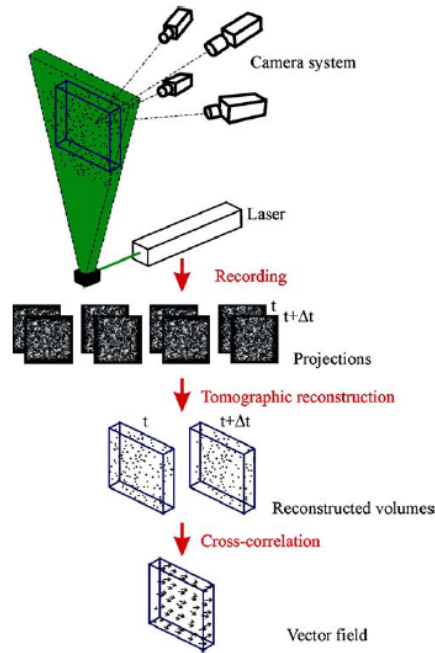


Figure 3.2: A typical Tomographic PIV procedure [35]

density of the particle was close to that of the fluid, then large particles can be used without the relaxation time penalty.

Helium Filled Soap Bubbles (HFSB) are tracer particles that have been used in PIV and PTV experiments as they are an ideal solution to the problems of large-scale PIV. HFSB are larger particles than their counterparts (typical particle diameter is $300\mu\text{m}$) and reflect 10,000 times more light [37]. Additionally, they also satisfy the condition of being neutrally buoyant. The compelling advantages make them ideal candidates to be used in experiments with complex flows where the pathlines of the bubbles can be visualized. Recent developments in bubble generation at sub-millimeter levels have accelerated the use of HFSB in experiments [21, 23]. Using sub-millimeter bubbles adds less momentum into the flow, has a higher generation efficiency, higher sensitivity towards small objects in the flow, and finally, lower model contamination [21]. Bearing such advantages, experiments have shown that by using HFSB, high spatial resolution can be achieved while minimally disturbing the flow physics, revealing detailed flow information [21].

3.5. Lagrangian Particle Tracking

LPT is a PIV technique in which the individual tracer particles are tracked in three-dimensional volume [52]. Unlike 2D PIV which involves cross-correlation on an interrogation window, in theory, LPT has higher spatial resolution due to the fact it tracks individual particles. The cross-correlation of planar PIV provides a single vector that accounts for the displacement of the flow in a particular direction. Thus planar PIV provides an Eulerian description of the flow. As mentioned in LPT individual particles are tracked and hence each particle has its own displacement vector, providing a Lagrangian insight into the flow. The added benefit of this method is that Eulerian information can be extracted from LPT measurements. Maas et al. [52] detailed the hardware equipment needed to perform 3D Particle Tracking Velocimetry (PTV). They also discuss a mathematical model that determines 3D

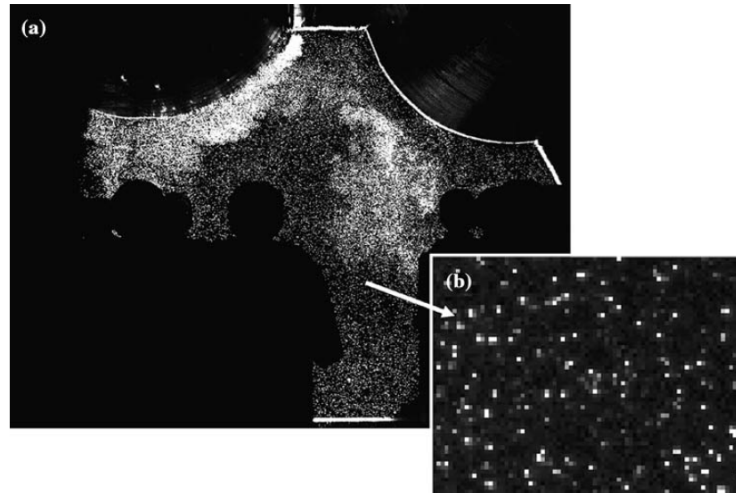


Figure 3.3: (a) The use of HFSB under illumination by Bosbach et al. [21] studying cabin ventilation, (b) Detailed View

coordinates which is significantly faster than the previous manual methods. [35] put forth a novel 3D PTV system that makes use of simultaneous views for the reconstruction of the measurement volume.

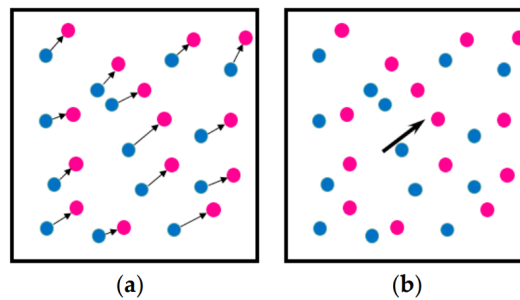


Figure 3.4: (a) Individual particles tracked in LPT (b) Single vector as a result of cross-correlation in PIV [36]

3.5.1. Shake-The-Box

Shake-the-box (STB), a novel Lagrangian Particle tracking method that predicts the particle distribution of the next time step using time-resolved flow data was put forth by Schanz et al.[63]. STB uses time-resolved data to track particles even in densely seeded flows with benefits in spatial resolution, computational load, and reduced ghost particle detection. Additionally, the STB methodology is computationally efficient when compared to its counterparts, 3D-PTV or Tomo-PIV. Before STB can be performed on an image data set, a calibrated Optical Transfer Function (OTF) must be generated [64].

In order to recreate the tracks, a reconstruction algorithm will first need a function that maps the voxel to the pixels. A linear mapping was used by Bosbach et al. [21], while a Gaussian function was used by Elsinga et al. [35]. The functions chosen however are applied to the entire volume uniformly, thus an error from even one camera will cause an incorrect reconstruction of the particle. In that, the particle may now appear as deformed, enlarged, displaced, or reduced in intensity, causing an increase in ghost particle detection [64]. This

can be resolved by using a variable OTF that can improve tracking and reduce ghost particle detection. The OTF can be generated using Volume Self-Calibration [72].

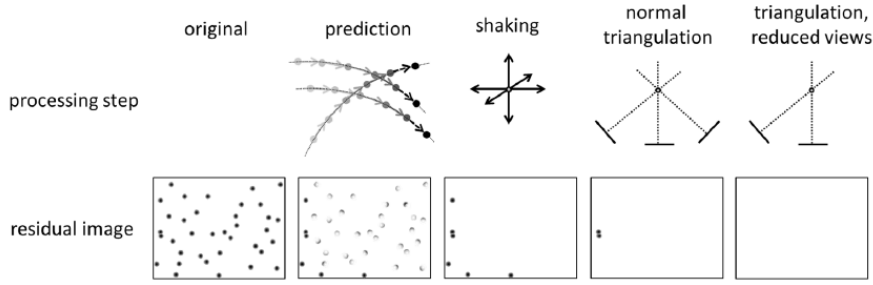


Figure 3.5: Schematic of the STB process in one time step as described by Schanz et al. [63]

The process of STB relies on the assumption that the particles in the measurement volume do not leave the volume, and the particle trajectory estimates are reliably accurate. The STB scheme can be found in detail in Schanz et al. [63]. A summary will be covered in this study. The algorithm works in three stages, namely *initialization*, *convergence*, and *converged stage*. In the *initialization* phase, there are no known tracks and they need to be developed from scratch. The goal of this phase is to identify particles by extended Iterative Particle Reconstruction (IPR) and to limit the detection of ghost tracks. Schanz et al. [63] set this to the first four time steps ($n_{init} = 4$).

Once the *initialization* has been completed, the algorithm can be extended such that additional tracks can be added using the time-resolved data until *convergence* is reached. This is achieved with the following steps:

1. *Prediction in next time step:* The particles being tracked at the end of the previous time step (t_n) is estimated at the next time step (t_{n+1}) by using a Wiener filter [73]. The filter can be adjusted to increase the accuracy depending on the available information.
2. *Shaking:* The predicted particle positions are usually not very far off from the actual positions. Image matching techniques can be used, which minimize the residual image I_R . Wienke [71] uses 'shaking' which involves moving the particle in space in small steps (δ_s) while calculating the local residue. The residual is calculated by considering the recorded image (I_{rec}), the projected image (I_{proj}), and the projection of the particle (I_{part}) with intensity I_P . The use of OTF [64] in this step will give more accurate results.
3. *Intensity Correction:* The intensity of the particle after shaking is calculated using:

$$I_{P,new} = I_P \cdot \sqrt{\frac{\sum_{\text{pxl}} I_{res+p}}{\sum_{\text{pxl}} I_{Part}}}$$

Where the sums add all pixels of the chosen window around the projection point. Ghost tracks generally occur when one of the cameras in the setup shows the highest intensity, while the remainder of the cameras show noise. By omitting such peaks in intensity while calculating the new intensity, ghost particles can be reduced considerably.

4. *Deleting Particles:* If the new intensity falls below a specified threshold, the shaking process does not converge to its true position as the particle is considered to be lost. In such a scenario, the particle track is deleted and the track is stopped.

5. *Identifying new candidates:* Once the particles have been predicted and corrected, the residual images are searched again as all tracks have not been established. The residual images will still show many particles with lower image density when compared to the original images. With each iteration, particles are added by triangulation, and the ghost particles are deleted until a stable number of particles in the image is reached.
6. A mixture of tracked particles and candidates are left, some of which might contain ghost particles. For the candidate particles, 4 track lengths are searched using a Gaussian-weighted average predictor. These tracks are added to the list of tracked particles. If found leaving the measurement domain, they are deleted.

The STB algorithm will reach a final *converged* and stable state where the number of particles that are tracked remains fairly constant until it leaves the measurement volume.

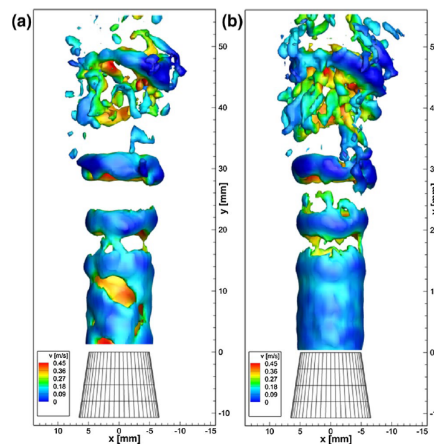


Figure 3.6: Isosurfaces of vorticity ($\omega = 175/s$) obtained from (a) Tomo-PIV and (b) STB with grid interpolation at the same spatial resolution, from Schanz et al. [63]

Figure 3.6 shows the comparison of the STB results to those obtained from Tomo-PIV from the experiments performed by Schanz et al. [63]. In essence, this is a comparison of the results of the algorithms being used for the reconstruction and consequently information extraction. The results of Schanz et al. [63] showed that STB is better able to represent the flow and resolve even small vortical structures due to its superior particle position accuracy and reduced/removal of ghost particles.

4

Experimental Setup

This chapter will expand on the experimental setup used to conduct the PIV measurements required to study the cylinder with a flexible splitter plate. The chapter covers the wind tunnel facility being used, the details of the model, and lastly, the details of the PIV equipment employed.

4.1. Wind Tunnel Facility

The PIV measurements were performed at the W-Tunnel Facility at the Faculty of Aerospace Engineering, TU Delft (*TU Delft Faculteit Luchtvaart- en Ruimtevaarttechniek*). The W-tunnel is an open-loop, open-jet wind tunnel with a square exit that can be interchanged between three contractions, namely, $40 \times 40 \text{ cm}^2$, $50 \times 50 \text{ cm}^2$, and $60 \times 60 \text{ cm}^2$. For the current experimental campaign, the $60 \times 60 \text{ cm}^2$ contraction was used. The maximum flow velocity that can be achieved by the tunnel is 35 m/s when using the smallest contraction. This velocity can be regulated by presetting the rotational speed of the centrifugal fan and depending on the flow velocity a turbulence level of 0.5% can be achieved [32]. In terms of the wind tunnel design, it consists of a plenum and a centrifugal fan which accelerates the air through the tunnel. This flow then passes through a diffuser followed by a settling chamber to create uniform flow conditions. This is also part of the tunnel where the flow is seeded with flow tracers. The more organized flow then passes through the pre-selected contraction, nozzle, and then exits the tunnel. For PIV experiments, such as the present study, the exhaust fan is used to remove the tracer particles (*specifically* HFSB) from the flow. Figure 4.1 shows the main components of the wind tunnel facility, open jet test section (4.1a), and exhaust fan (4.1b). Additionally, two transparent plates are attached to the exit of the wind tunnel. These plates are used to secure the model in place and simultaneously facilitate the illumination of the test section.

In order to categorize the wake dynamics of the cylinder with a flexible splitter plate, the model will be subject to a range of flow velocities. Figure 4.2 shows the relation between the set RPM and the exit velocity of the flow coming out of the tunnel. It was found that the relationship was linear for RPMs between 300 and 2800 with the equation of the best-fit line being:

$$y = (0.0059)x - 0.3823 \quad (4.1)$$

where, x is the set RPM data, and y is the corresponding tunnel velocity to be calculated.



Figure 4.1: The W-Tunnel, both images reproduced from TU Delft Aerodynamics Experimental Wiki [2]

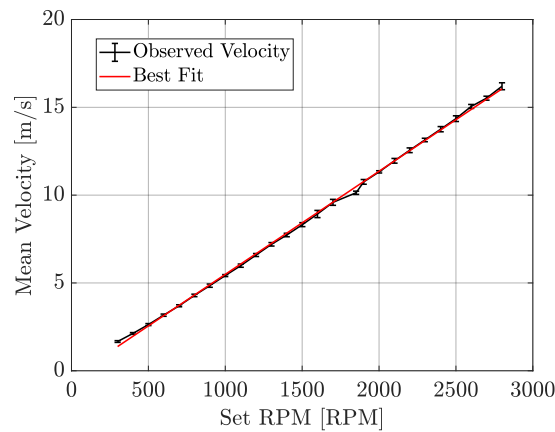


Figure 4.2: The relationship between RPM of the W-Tunnel and the velocity

4.2. Model Details

To perform the experimental campaign, the model used was the same as the one produced by Gonzalez Saiz et al. [60]. The model consists of two parts, the first part is the cylinder, and the second is the flexible splitter plate. This will be covered separately and in more depth in the following sub-sections.

4.2.1. Cylinder

The cylinder being used is a circular cylinder with a diameter of $D_{cyl} = 90$ mm and a height of 600 mm, installed vertically in the wind tunnel test section. The cylinder is fastened to the test section with the help of screws and painted black to avoid reflections that may affect the PIV measurements. The cylinder surface is made to be smooth to reduce the influence on the boundary layer and ensure laminar flow separation, resulting in von Kármán vortex shedding. Another benefit of a smooth cylinder is that the experiments can be repeatable and reproducible. Additionally, on the rear of the cylinder, there is a vertically attached bracket where the splitter plate can be mounted.

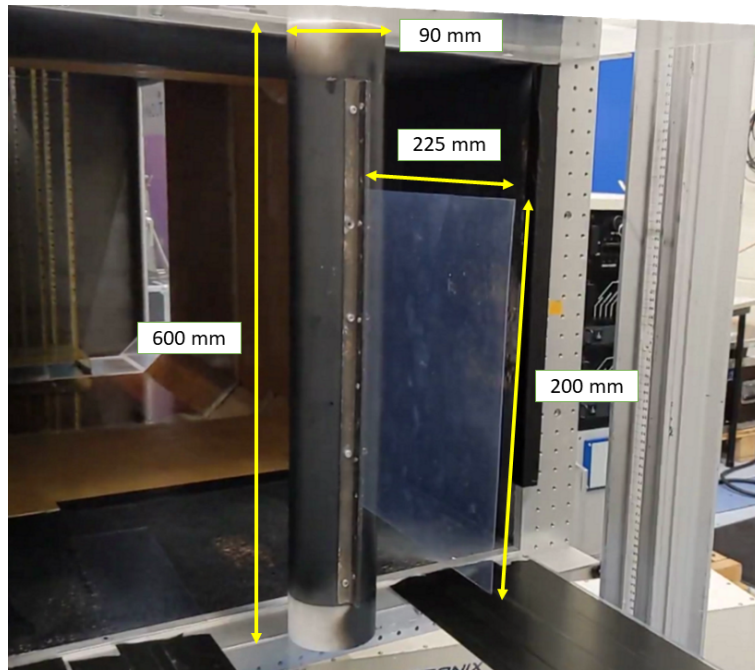


Figure 4.3: The model (cylinder with a flexible splitter plate) installed in the test section of the wind tunnel

4.2.2. Splitter Plate

The rectangular splitter plate is vertically attached to the rear of the cylinder. It is roughly placed at a mid-span position and is made of an optically transparent material so that the HFSB particles can be tracked by the STB algorithm behind it. This allows for the camera to be placed in only one direction simplifying the support structure design. The splitter plate, made out of 0.3 mm PVC sheet, is $235 \times 200 \text{ mm}^2$. As mentioned before, the splitter plate is attached to the cylinder with the help of the vertical bracket. Thus, 10 mm of attachment tolerance was accounted for in the dimensions of the splitter plate. This means that the flexible portion of the plate is $L = 225 \text{ mm}$ giving an L/D ratio of 2.5. Several splitter plates were tested in the wake of the cylinder with some being too heavy and collapsing on their own weight, while others were found to buckle under high bending and torsional loads. The physical properties of the splitter plate chosen are summarized in Table 4.1. In order to obtain measurements of the flexible splitter plate kinematics, markers were made. The markers are bright surface spots with an average diameter of 0.8 mm and pitch of 1 cm. The preliminary tests will be discussed in the next sections.

Table 4.1: Physical properties of the flexible splitter plate

Property	Symbol	Value	Units
Thickness	T/D_{cyl}	0.0028	[-]
Length	L/D	2.5	[-]
Width	W/D	2.22	[-]
Density of Splitter Plate	ρ_{sp}	1300	[kg/m^3]
Young's Modulus	E	0.1	[GPa]
Poisson Ratio	ν	0.3	[-]
Flexural Rigidity	EI	2.6×10^{-4}	[Nm]

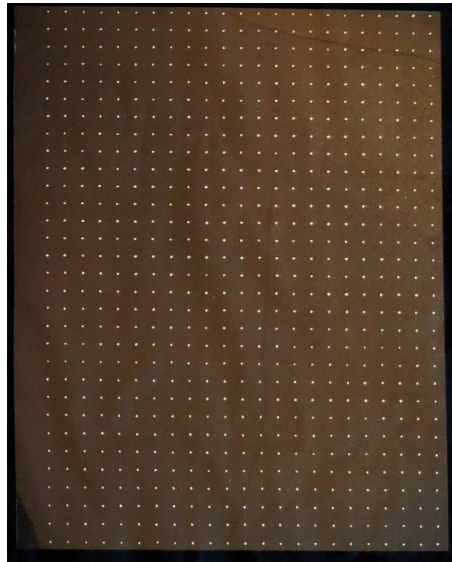


Figure 4.4: The transparent flexible splitter plate against a dark background. The surface markers are made on the plate, additionally, 1 cm of space has been accounted for the mounting on the cylinder bracket. The surface markers are placed with a grid spacing of 1 cm with an average diameter of 0.8 mm

4.3. PIV Equipment Details

In this section, the details of the PIV equipment are discussed. A PIV setup broadly consists of tracer particles, a light source, and high-speed cameras. In this section, the details of the PIV equipment will be discussed in order to extract the most information out of the flow.

4.3.1. Frame Structure and Final Setup

Figure 4.5 shows the final setup of the PIV equipment. The main components are listed below:

- Tomographic Camera Setup
- High Speed Controller
- Fluid Supply Unit
- Mirror
- Model
- Black Screen
- Support Frame Structure
- LED Units

The tomographic camera support frame setup is made from X95 structure beams. Since the splitter plate is optically transparent, the support frame is constructed on only one side of the plate, thus reducing the complexity of the experimental setup. The individual components are dealt with in more detail in the following sub-sections.

4.3.2. Helium Filled Soap Bubbles (Tracer Particle)

The potential use of HFSB as tracer particles in large-scale PIV has been discussed in detail in the previous chapter (Chapter 3). The HFSB are produced in the tunnel by means of a Fluid Supply Unit (FSU). The in-house FSU was developed by Dennis Bruikman [3]. The basic design of the FSU consists of three inlets, namely, the air, helium, and soap inlets. The air inlet is used for two purposes, the first is to pressurize the tank containing the soap, and the second is to produce air-filled soap bubbles. The Helium inlet is connected to the bottle/cylinder and used only during actual PIV measurements, while the soap return is used to collect the

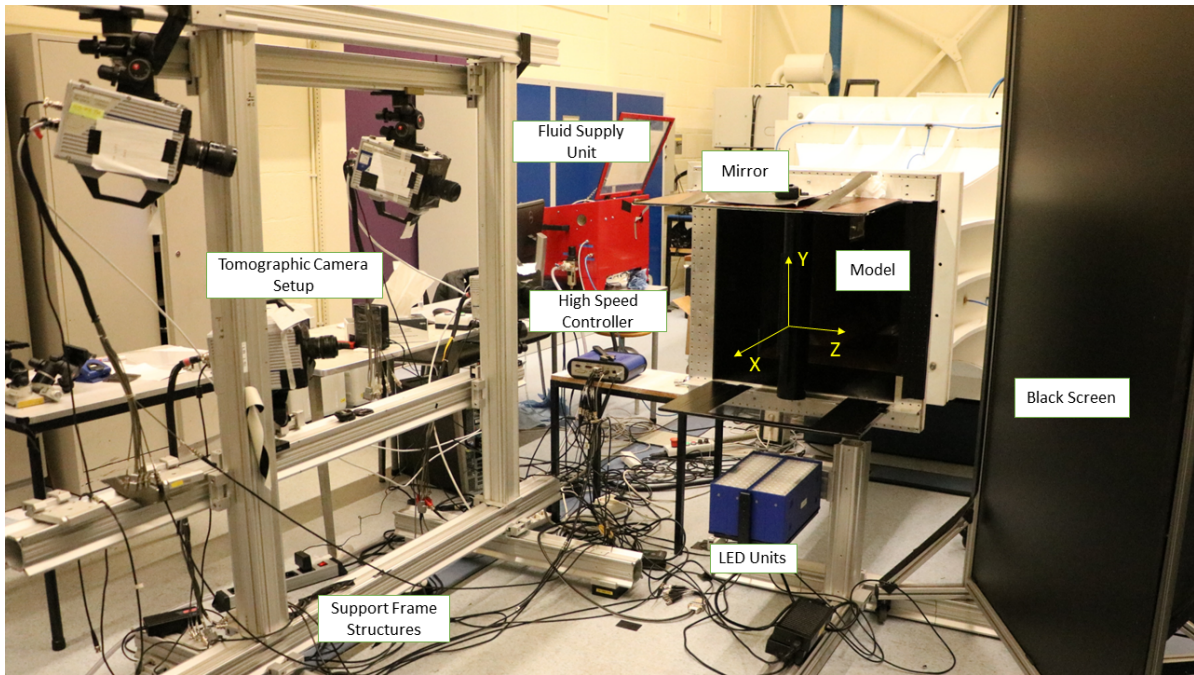


Figure 4.5: The final experimental set up in the W-Tunnel

unused soap from the seeder rake. The production of the HFSB can be controlled by using inlet pressure regulators. The nominal working pressures of the inlets are 2 bar, 1.8 bar, and 2.5 bar for air, helium, and soap respectively. [60, 3]

The device that generates the bubbles is called the seeding rake and is placed inside the wind tunnel. The seeding rake is developed in-house consisting of 200 nozzles. These nozzles are evenly distributed and placed along columns in the shape of airfoils to minimize the disturbance to the flow. The seeding unit can be configured to work with either 100 nozzles or 200 nozzles in order to achieve the correct particles per pixel (ppp) for the experiment, which is the measure of particle density in the flow. The nominal production rate of the bubbles is 6×10^6 bubbles/s. For this experiment three, 1 liter soap bottles were used during the measurement campaign [60]. Additionally, both configurations of the seeding rake were used in order to keep the seeding concentration in the flow consistent.

4.3.3. Light Sources for PIV

The light source is perhaps one of the most crucial aspects of a successful PIV measurement campaign. In the literature review, it was detailed how LEDs can be used to illuminate medium to large-scale PIV experiments [62].

For this measurement campaign, two LaVision LED Flashlights - 300 [4] were used. The LED lights are positioned next to each other and under the wind tunnel exit. Each individual LED flashlight consists of 72 high-powered LEDs that are distributed over an area of $300 \times 100 \text{ mm}^2$. Unlike lasers, the LEDs produce incoherent white light, ensuring homogeneous brightness in the illuminated area and across the measurement duration. To improve the intensity of light in the measurement volume, a mirror was attached directly above the LED lights. Lastly, the LED lights are triggered by a Programmable Time Unit (PTU) that is connected to the acquisition system.

4.3.4. High-Speed Cameras

The measurement volume was recorded using four high-speed CMOS cameras. The cameras have a sensor size of 1024×1024 pixels with the pixel size being $20 \times 20 \mu\text{m}$. At full resolution, the maximum acquisition frequency for the camera is 5400 Hz. The four cameras are positioned in a tomographic setup [35] roughly a meter away from the model. The cameras subtend an aperture of about 30 deg. Three cameras Nikon Nikkor 50 mm lenses were used along with a 60 mm lens for the fourth camera to record the particles from different positions and perspectives. The acquisition frequency for the recording was set to 1 kHz recording 5000 images. This means that the flow of the particles is recorded for a duration of 5 seconds. In the case of high flow velocities, an acquisition frequency of 2 kHz was used so that the particles can be accurately reconstructed and the splitter plate deflections can be captured. An essential part of PIV experiments is that the light source and the camera are in synchronization. This synchronization is achieved by using a high-speed controller from LaVision [5]. All the connections are made through Bayonet NeillConcelman (BNC) cables, which are quick connect/disconnect cables. Once the images have been acquired by the cameras, they are transferred to the acquisition computer system by ethernet cables, while the high-speed controller is connected to the acquisition computer via a USB cable.

Table 4.2: Details of the optical setup

Tomographic System	
Illumination	2x LaVision <i>Flashlight 300</i> LED
Cameras	2x Photron <i>FastCam SA1.1</i> (1024 x 1024 pixels, 5400 fps)
	1x Photron <i>FastCam SA5</i> (1024 x 1024 pixels, 7000 fps)
	1x HighSpeedStar 8 (1024 x 1024 pixels, 7000 fps)
Lenses	3x Objectives Nikkor 50 mm - f# = 1/11.2
	1x Objectives Nikkor 60 mm - f# = 1/11.2
Acquisition Frequency	1000 and 2000 Hz
Optical Magnification	0.0435

4.3.5. Acquisition

The acquisition system consists of the W-Tunnel computer and the LaVision DaVis 10.1 software. This computer is used to store the experimental data, while the software is used to pre-process, process, and to some extent post-process the experimental data. The DaVis software is used to implement the STB algorithm to develop the particle tracks. The computer is additionally used to synchronize (with the help of the PTU) all the components of the PIV setup, such that they are all started and stopped at the end of the measurement time. The recorded data is then stored on a hard disk and then connected to one of the servers in the Dept. of Aerospace Engineering, TU Delft to further process the data. Information about the processing strategies can be found in the next chapter.

4.4. Parameters

There are several important parameters that need to be set and calculated for the experiments. These can be broadly divided into experimental and PIV parameters. The experimental parameters are associated with the wind tunnel and other external factors such as air density, etc. On the other hand, PIV parameters are related to the setting up of the tomographic system, such as the magnification factor and F-stop. For the sake of conciseness, these parameters have been presented in tabular form below.

Table 4.3: Experimental Parameters in the Wind Tunnel

Parameter	Symbol	Formula	Value	Units
Cylinder Diameter	D_{cyl}	-	0.09	[m]
Air Density	ρ	-	1.225	[kgm^{-3}]
Air Temperature	T	-	298	[K]
Dynamic Viscosity	μ	-	1.8×10^{-5}	[$\text{kgm}^{-1}\text{s}^{-1}$]
Freestream Velocity Range	V_∞	-	2 - 12	[ms^{-1}]
Reynolds Number Range	Re	$\frac{\rho V_\infty D_{cyl}}{\mu}$	12, 250-73, 500	[-]

Table 4.4: Experimental parameters for PIV

Parameter	Symbol	Equation	50mm Lens	60 mm Lens	Unit
Pixel Size	pxl	-	20×10^{-6}		[m]
Resolution	-	-	1024×1024		[-]
Field of View	FOV		0.4710		[m]
Depth of Field	δz	-	30×10^{-2}		[m]
Focal Length	f	-	50	60	[mm]
F-Stop	$f\#$	-		11.2	[-]
Magnification Factor	M	(pxl \times res.)/FOV		0.0435	
Wavelength of light	λ	-	500×10^{-9}		[m]
Object Distance	d_o	$f(1/M + 1)$	1200	1440	[mm]
Image Distance	d_i	$M.d_o$	52	63	[mm]

4.5. Preliminary Testing

Before PIV measurements can be made, the different behaviors of the splitter plate must be ascertained. In order to do this, a test splitter plate was attached to the cylinder and the tunnel was switched on. The wind tunnel speed was progressively increased from the lowest to the highest flow velocities and observations were made. In order to get a better image of the splitter plate behavior, one of the high-speed cameras was placed directly above it to get a top-down view of the plate. The acquired camera images were summed up to generate a single image, as seen in Figure 4.6. The measurement time for the preliminary testing was set to 1 second. From these preliminary runs, four regimes or splitter plate behaviors could be identified and form the basis for the full PIV measurements made later. These regimes correlate to the experiments performed by De Nayer et al. [31]. A description of these regimes can be found in Chapter 2. For the purpose of this thesis, the regimes will be named as the following (Table 4.5):

Table 4.5: Preliminary testing regime categorization

Number	Regime Name	Freestream Velocity [m/s]	Reynolds Number [-]
I	Crossover	3.7	22,000
II	Baseline	4.3	25,700
III	Reduced Amplitude	7.2	44,100
IV	Chaotic	11.3	68,600

The first regime is called the '*crossover condition*' as the foil changes from weak two-dimensional motion to the first mode of oscillation. At this flow velocity, there was enough dynamic pressure to cause the splitter plate to oscillate with a small amplitude. It was also

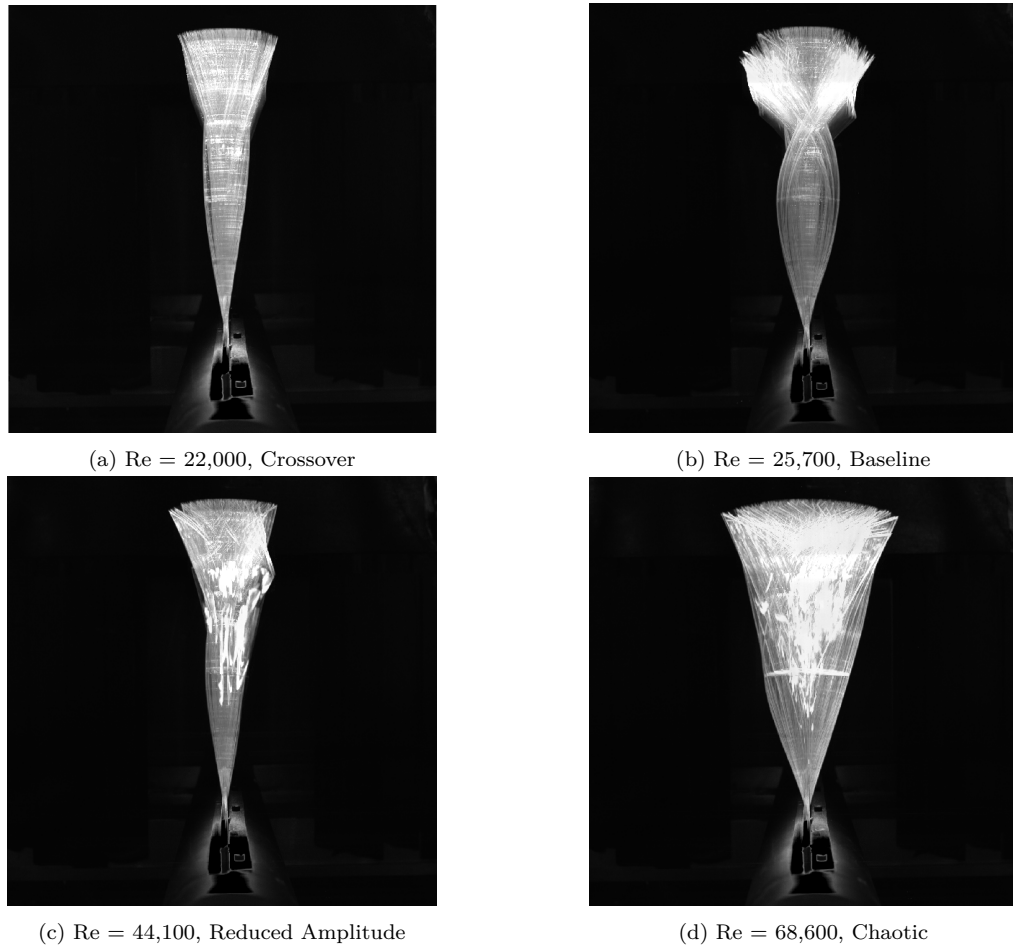


Figure 4.6: Results of the preliminary study, the images across the measurement duration (1 second) are superimposed

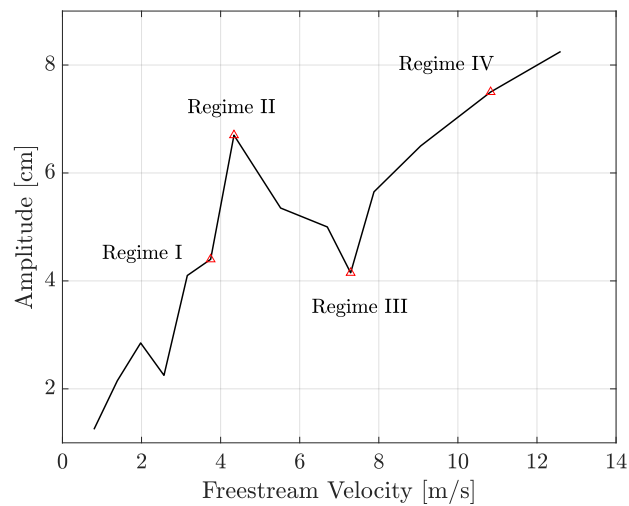


Figure 4.7: Pre Result

observed that at this velocity, there was an appearance of the first swivel mode with the nodal point weakly visible in the top-down view of the splitter plate motion. As the dynamic pressure

increases, the splitter plate oscillated with a higher amplitude and the first swiveling mode is apparent. For this reason, the regime will be called '*baseline*'. The purpose of deciding a baseline is to give a reference and comparison to the other regimes observed. At higher Reynolds numbers, namely 44,100, the first swivel mode was replaced by oscillations with many modes superimposed. Additionally, the number of torsional vibrations of the splitter plate increased, while the bending reduced. This regime is best described as a '*reduced amplitude*' regime. At the highest wind tunnel velocities, the splitter plate motion was chaotic. In that, there were many bending and torsional splitter plate modes superimposed. This regime is characterized by large amplitudes of vibration and is thus appropriately termed as the '*chaotic*' regime. It was also observed that at times regular plate oscillation was not sustained for a long period of time and the resonance would occur in 'bursts'. A 'burst' is defined as a period of high-amplitude oscillations in between low-amplitude oscillations. These burst motions were observed at different velocities which indicated that the phenomenon occurred when the dynamic pressure was large enough to cause deformations of the plate.

These visual descriptions are reflected in Figure 4.7, where the approximate amplitude of the splitter plate motion is plotted against the freestream velocity of the tunnel. The amplitudes are calculated by estimating the pixel distance which is then multiplied by the pixel pitch and divided by the magnification factor to get the actual amplitude of the splitter plate. Since the motion of the splitter plate is not periodic and is a combination of bending and torsion, an average amplitude cannot be calculated. For this reason, only the maximum amplitude is plotted to get an insight into the splitter plate behavior over a range of velocities.

5

Image Analysis and Data Processing

In this chapter, the steps to convert the raw images into usable data are elaborated upon. The steps involved in treating the images can be broadly divided into Pre-processing, Processing, and Post-processing.

Using the setup described in the previous chapter, the PIV measurements were made. The end result of each measurement was a large number of images of the measurement volume. In order to derive meaningful information from these images, they must first be processed. Each of these steps involved will be described in more detail in this chapter with the relevant parameters listed in tabular form.

5.1. Pre-Processing

In order to ensure a consistent quality of images across different measurements, pre-processing of the raw images is required. In an ideal scenario, the raw images are composed of the light that is scattered by the bubbles. This is favorable as it ensures good cross-correlation and consequently velocity vector determination.

But in reality, the raw images may often contain reflections from the model that is placed in the illuminated measurement volume. This reflected light will dominate the pixel intensity when compared to the scattered light by the bubbles. As a result of this, erroneous vectors are calculated which results in loss of useful information [65]. In order to minimize the effect of external reflections from the model or otherwise, a symmetrical minimum time filter is used. The filter works by identifying the minimum light intensity for each pixel given a certain kernel of images. For low freestream velocities, the kernel was set to 'all images' to remove the unwanted reflections and noise. This also includes the cases of higher freestream velocities, where the large deflections of the splitter plate caused some reflections. Additionally, for the reduced amplitude case, the structural markers on the splitter plate (see Figure 4.4) generated spurious vectors. This was due to the fact that the spacing between the markers (1 cm) was roughly the same distance traversed by the particles in one second (for that particular flow speed), causing the STB algorithm to misidentify the structural markers as tracer particles. In order to minimize the issue of the spurious vectors, a kernel of 5 images (instead of all the images) was used to minimize the effect of structural marks. The unfiltered (Figure 5.1a) and filtered image (Figure 5.1b) can be found in Figure 5.1. In the figures, we can see that the reflections from the cylinder have been removed as well as some of the reflections of the splitter plate.

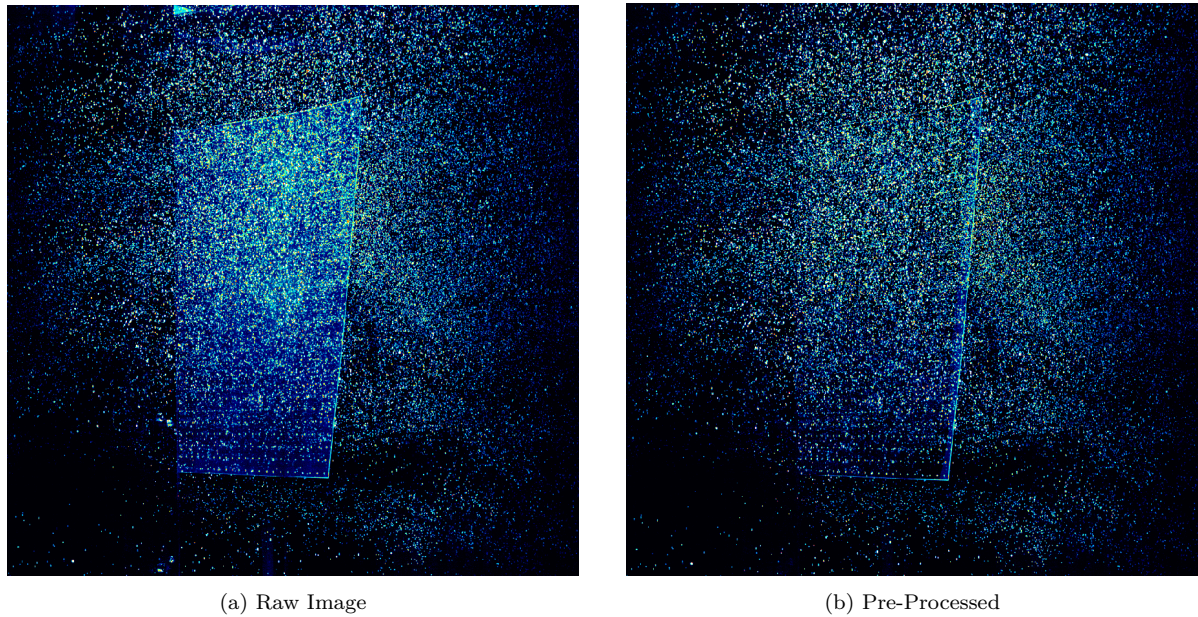


Figure 5.1: The effect of the application of the symmetrical subtract time filter

5.2. Volume Self-Calibration and Optical Transfer Function

The second part of analyzing the images involves performing a Volume Self-Calibration (VSC) and the generation of an Optical Transfer Function (OTF). The purpose of the VSC is to remove any remaining calibration disparities with the recorded images. This process is performed in two steps: (a) generation of a disparity vector map, (b) then correcting the perspective calibration function [40]. In an ideal scenario, the perspective error is zero when a particle is directly in the line of sight of all the cameras in a multi-camera setup. However, in reality, there is always some amount of perspective error as the particle may not always intersect with the camera's line of sight. In this case, an estimate needs to be made for a point in space that is closest to the lines of sight from all cameras, and this position is back-projected onto the camera sensor. The disparity vector map is a collection of vectors that point to the back-projected position from the original sensor positions. In order to do this systematically and correctly, the measurement volume is divided into further sub-volumes and the disparity information from each sub-volume is then combined [40]. As discussed in the literature review, an OTF [72] is required to perform the STB operation. The generation of the OTF allows for a precise reconstruction of the particles as it reduces ghost particle detection by optimizing the intensity and particle position [40, 64, 72].

The VSC process was performed for each case, i.e. with and without a splitter plate, and at different freestream velocities. This was found to produce better and more targeted results for each specific case, maximizing the use of the particles. In order to perform the VSC, 1000 images were taken spanning the entire dataset for better statistical convergence. The VSC parameters were sequentially refined to find the right balance between processing time and the quality of the disparity vector maps. The final parameters for the VSC are listed in Table 5.1. Once the process VSC was finished and accepted, the OTF was calculated and then subsequently used while performing STB operations.

Table 5.1: Parameters for the Volume Self Calibration

	Parameter	Value	Units
Volume	Xmin	-250	[mm]
	Xmax	250	[mm]
	Ymin	-200	[mm]
	Ymax	200	[mm]
	Zmin	-200	[mm]
	Zmax	200	[mm]
Particle Detection	Maximum number of particles in image	10000	[-]
	Allowed triangulation error	1.00	pixels
Data Range	Range	1-5000	[-]
	Image increment	5	[-]

5.3. Processing: Shake-The-Box Parameters

As detailed in Chapter 3, Shake-The-Box (STB) is a Lagrangian Particle Tracking (LPT) algorithm that is used to track the flow of tracer particles. The STB algorithm is used on the pre processed images along with the VSC and OTF that have been generated for each flow case. The specific parameters for the STB algorithm are listed in Table 5.2.

The parameters have been sequentially refined to strike the right balance between the processing time and the quality of the tracks that the algorithm develops. For this reason, the measurement volume was cropped from the original VSC volume. The reduced measurement volume ensures that the quality of the tracks is consistent across all flow cases. Some of the additional benefits were that the processing time was reduced by approximately 40% and the burden on storage capacity was reduced by almost 80%.

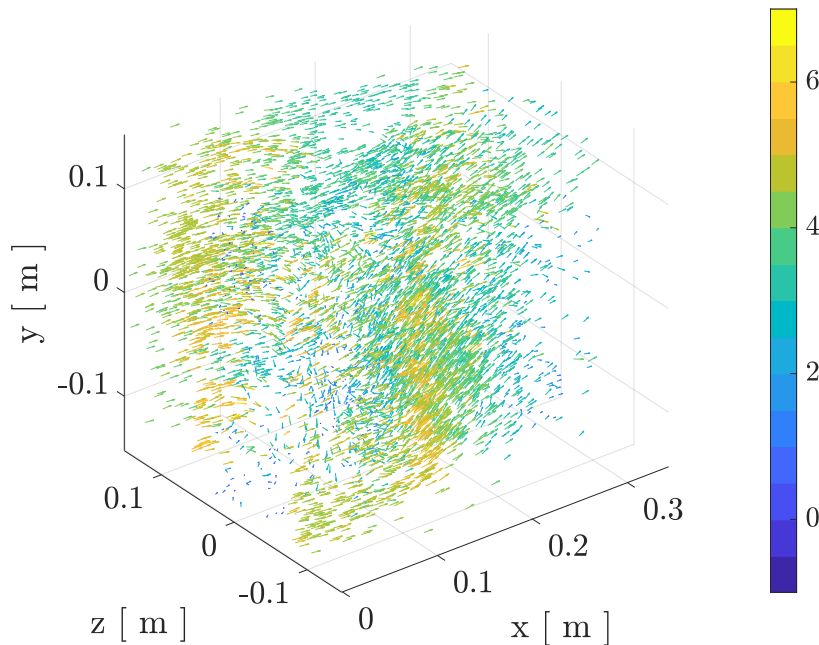


Figure 5.2: The tracks developed by the STB algorithm for a measurement volume. The color bar represents the velocity magnitude of the particle tracks in m/s (Case: Sporadic Resonance)

The most important STB parameters to are [40]:

- **Intensity Threshold for 2D Particle Detection:** Even after pre processing the image to remove reflections and noise, the filtered images may contain some amount of noise. This threshold is a final adjustment for the algorithm to distinguish particles from noise. The set value is case specific and is fine-tuned to improve the results. If this value is too high it might lead to sparse tracks being developed. Consequently, if the value is too low, the background noise might contribute to the detection of ghost particles and tracks.
- **Allowed Triangulation Error:** This value is essentially the tolerance for the triangulation error that exists due to the different camera perspectives. If this value is set too high, then the number of admissible particles is increased. In this case, not all the particles are real and lead to spurious vectors being calculated. On the other hand, a lower value will impose a stricter tolerance leading to fewer particles being detected, although with lower ghost particles.
- **Velocity Limits:** The velocity limits are used to define the range of permissible velocity vectors. Since the freestream velocity is set and known beforehand, the x -, y -, and z -components of the velocity can be estimated. These values again need to be sequentially refined to balance loss of information versus spurious vector detection. In this field, even negative velocities are permissible as they are considered to be 'backflow'.
- **Maximum Relative Change in Particle Shift:** This parameter is used to limit the change in direction or magnitude of the particle between two time instances. This improves the quality of the tracks developed as particles that exhibit large changes in the above-mentioned quantities can be filtered. DaVis sets this by default to 20%. In the case of the reduced amplitude regime, this parameter was relaxed in order to account for the large deflections of the flexible splitter plate. It was noted that the number of tracks developed by the algorithm improved, consequently improving the statistics.

5.4. Binning

The STB tracks developed give a Lagrangian description of the flow and are unstructured, in that, the tracks represent the particles that pass through the measurement volume during the measurement time. In order to analyze the data to answer the research questions, mapping the track data onto a Cartesian grid is required. This is done by the operation known as 'Binning'. Binning is essentially the conversion of three-dimensional STB data into a regular Cartesian grid [40]. There are two options for this kind of conversion, a vector field for each time instant, or a single time-averaged vector field.

The averaging process is done by defining a sub-volume size, also known as a 'bin' size, and the amount of overlap to determine the vector spacing on the grid. The x -, y -, and z -components of the vector are calculated by utilizing the available tracks in the vicinity of the sub-volume. The contribution of the tracks is done using a Gaussian weighting function [40]. More information about the ensemble PTV statistics can be found in the work done by Agüera et al. [6]. A representation of this binned data can be seen in Figure 5.3 where the data is represented on a Cartesian grid.

In order to keep things consistent across all the cases, the binning parameters were kept constant. The sub-volume size was chosen to be 64 voxel with a 75% overlap. After initially trying a sub-volume of 128 voxel, it was observed that the vortex shedding was poorly captured

Table 5.2: Parameters for Shake-The-Box, Case $Re = 27,500$

	Parameter	Value	Units
Volume	Xmin	-150	[mm]
	Xmax	210	[mm]
	Ymin	-150	[mm]
	Ymax	150	[mm]
	Zmin	-150	[mm]
	Zmax	150	[mm]
Particle Detection	Threshold	80	counts
	Allowed triangulation error	1.00	[voxel]
Shaking	Adding particles (outer loop)	4	iterations
	Refine particle position and intensity (inner loop)	4	iterations
	Shake particle position by	0.00	[voxel]
	Remove particles if closer than	1.50	[voxel]
	Remove weaker particles if intensity <	0.10	avg. int.
Particle image shape and intensity	Make OTF smaller	1.00	times
	Residuuum computation - increase particle intensity	1.00	times
	Residuuum computation - OTF radius	auto	pixel
Velocity Limits	V_x	2 ± 4	[m/s]
	V_y	0 ± 3	[m/s]
	V_z	0 ± 4	[m/s]
Acceleration Limits	Max. abs. change in particle shift	1.00	voxel
	Max. rel. change in particle shift	20.00	%

leading to a severe loss of information. The sub-volume size was refined to capture the vortex-shedding process. The number of particles for the sub-volume to be valid is set to one. Using a number larger than one can improve results, but may also cause loss of information if the particle density is low in some places [40].

For this thesis, both options for binning were used, i.e, the vector field for each time step and a single vector field over time. The instantaneous vector fields were used in post processing to calculate the energy modes and the spectral decomposition, while the single time-averaged vector field was used to calculate the mean and standard deviation. It was observed that for higher flow velocities the number of particles tracked by the STB algorithm was a bit low in some spanwise sections. Additionally, it was noted that the splitter plate itself affected the density of the tracks developed behind it. This could be attributed to the camera positioning (see Figure 4.5) and the fact that the splitter plate was not always optically transparent under high deformations. In such cases, the instantaneous vector fields did not accurately represent the spanwise physics, and it was found that the time-averaged vector field provided better results. This is because time-averaging puts all the tracks from different time steps into the bins, improving the statistics.

The binned data is then exported as '.dat' files. These files are then loaded onto Matlab and converted into '.mat' files (using a self-made code), which can be then used for post processing.

5.5. Post-Processing

Once the images have been pre-processed and processed using the STB algorithm, the next stage of the analysis is post-processing. This step involves using the data after processing

Table 5.3: Parameters for Binning

	Parameter	Value	Units
Collect tracks inside subvolumes	Subvolume size	64	voxels
	Overlap	75	%
	Grid	16	voxel
	Minimum number of particles	1	[-]
	Spatial Polynomial Order	0	[-]
Track conversion by polynomial fit	Polynomial order	3	[-]
	Filter length (time steps)	5	[-]

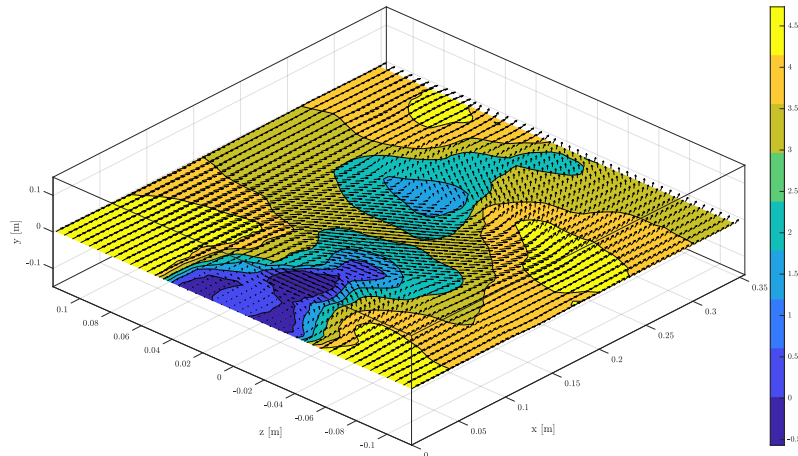


Figure 5.3: Representation of the binned STB data in a selected X-Z plane. The colorbar represents the velocity magnitude of the particle tracks (Case: Sporadic Resonance)

to generate meaningful results to answer the research questions. In this section, two of the analysis methods will be discussed, namely Proper Orthogonal Decomposition and Welch's method for spectral decomposition.

5.5.1. Proper Orthogonal Decomposition

Proper Orthogonal Decomposition (POD) is a form of data processing where approximate descriptions are made for higher-dimensional processes. It is an efficient way to represent dominant modes of a process [49] and is most useful when analyzing data from experiments or numerical simulations. Additionally, it also enables the analysis of turbulent flows as it allows the extraction of spatial and temporal structures [17]. POD is essentially a set of ordered orthonormal basis vectors that are used to represent the data set as lower order approximations [49, 51]. In the context of the current analysis, the POD will reveal flow structures and the energy modes associated with them. These flow structures and associated energy modes can provide insight into the influence of the flexible splitter plate on the near wake of the cylinder. Any flow vector can be decomposed into its steady component and fluctuating component. This is given as:

$$u(\vec{x}, t) = \bar{u}(\vec{x}) + u'(\vec{x}, t) \quad (5.1)$$

where, $\bar{u}(\vec{x})$ is the steady component and is simply average in time of the velocity field, given as:

$$\bar{u}(\vec{x}) = \frac{1}{N} \sum_i^N u(\vec{x}, t_i) \quad (5.2)$$

The time-dependent component of the velocity, $u'(\vec{x}, t)$, can be written as a linear combination of orthonormal spatial model $\vec{\phi}_k(x)$ and the associated time-coefficient $\vec{A}_k(t)$. This is represented as:

$$u'(\vec{x}, t) = \sum_k^N \lambda_k \vec{A}_k(t) \vec{\phi}_k(x) \quad (5.3)$$

The modes ($\vec{\phi}_k(x)$) are calculated by solving an eigenvalue problem, and are then arranged in decreasing energy content, or decreasing eigenvalues λ_k . This process is performed on Matlab by using the `svd()` function which performs a Singular Value Decomposition (SVD). SVD is one of the ways to perform POD as SVD finds the basis vectors which satisfy the POD requirement [49].

5.5.2. Power Spectral Density

The periodicity of the vortex shedding in the wake of the cylinder can be determined by examining the transverse component of the velocity. By plotting the magnitude of this transverse component against the measurement time, an instantaneous time series can be generated. This time series can then be analyzed to find the most dominant frequencies, which manifests itself as a peak in the Power Spectral Density (PSD) estimate. In order to perform this PSD estimate, Welch's method will be used [70].

Welch's method is an approach to estimating the power spectral density of a signal. This method was first introduced by Peter D. Welch [70]. In simple terms, the method is based on breaking up a time series (signal) into smaller segments or sequences. For each of these segments, a periodogram is calculated; all periodograms are then averaged for the entire time series. This method is a modification of Bartlett's method with regards to the fact that (a) this method allows the segments to overlap each other (usually 50%), and (b) the method allows the application of a window function that produces modified periodograms [41]. Additionally, the benefit of averaging the segmented periodograms is that there is a reduction in the variance of the estimate when compared to a single periodogram of the entire signal.

Mathematically the PSD using Welch's method can be written as [41]:

$$\hat{P}_W(e^{j\omega}) = \frac{1}{KLU} \sum_{i=0}^{K-1} \left| \sum_{n=0}^{L-1} w(n)x(n+iD)e^{-jn\omega} \right|^2 \quad (5.4)$$

where; $w(n)$ is the data window which consists of L points that are contained in the sequence. The term $x(n+iD)$ denotes the i^{th} sequence of the signal that has an offset of D points. K is the total number of sequences that span the entire dataset of N points. As an average of the modified periodograms, the PSD estimate can be written as below:

$$\hat{P}_W(e^{j\omega}) = \frac{1}{K} \sum_{i=0}^{K-1} \hat{P}_M^{(i)}(e^{j\omega}) \quad (5.5)$$

where; P_M is the PSD of the individually modified periodogram.

Matlab provides an inbuilt function in its Signal Processing Toolbox called `pwelch()`. Matlab by default divides the time series into segments such that 8 of them with 50% overlap can be obtained. Each of the calculated segments is then windowed with a Hamming window, and as per the definition, they are averaged. `pwelch()` calculates the PSD and the associated frequencies, which can then be plotted on a graph to identify and visualize the dominant frequencies.

6

Results

In this chapter, the meaningful results generated using the data processing strategies from the previous chapter will be presented and discussed. The observations and interpretations of the results will be covered in depth which will then be used to answer the research questions.

This chapter presents and discusses the results obtained from the experiment discussed in Chapter 4 and the data obtained through the techniques described in Chapter 5. The chapter primarily puts forward the results of the *baseline*, *reduced amplitude*, and *chaotic* regimes. The crossover regime is quite similar to its results to the baseline and was chosen to primarily reflect the transition from small to larger two-dimensional oscillations with some torsion. Hence, this has been covered in Appendix A.

6.1. Baseline, Re 25,700

In order to present the results in a comparative manner, this was chosen to be the baseline. In order to quantify and observe the effects of the splitter plate it is compared to pure cylinder flow (i.e, no splitter attached). For the sake of this thesis, these two cases will be referred to as the '*Cylinder without Splitter Plate*' and '*Cylinder with Splitter Plate*' respectively. Additionally, each regime will be studied through the lens of statistics and modal decomposition.

6.1.1. Statistical Analysis

In order to get more accurate statistics for the mean and standard deviations, a single time-averaged velocity field was calculated. This velocity field was then averaged along the span such that a single spanwise-time average velocity field was obtained. The velocity fields for the streamwise and transverse velocity components were investigated. Figure 6.1 shows statistics of the streamwise velocity component. The top row shows the cylinder without the splitter plate and immediately we can see a small recirculation zone at the base of the wake. For the baseline case, it was observed the presence of a long foil elongated the recirculation bubble from approximately 0.15 m to 0.25 m. This can be attributed to the fact that the formation region (which consists of crossflow and backflow) is lengthened by the insertion of the splitter plate [20, 39]. This lengthening can also be verified by the standard deviation plot which shows longer shear layer fluctuations on either side of the plate. The regions of fluctuations are not only longer in the case of the splitter plate, but also in magnitude due to the presence and motion of the splitter plate in the wake. Additionally, in the near wake of the cylinder with the splitter plate, a reduction of fluctuations is observed. This can be attributed to the presence of the splitter plate, which obstructs the base flow in the wake of the cylinder.

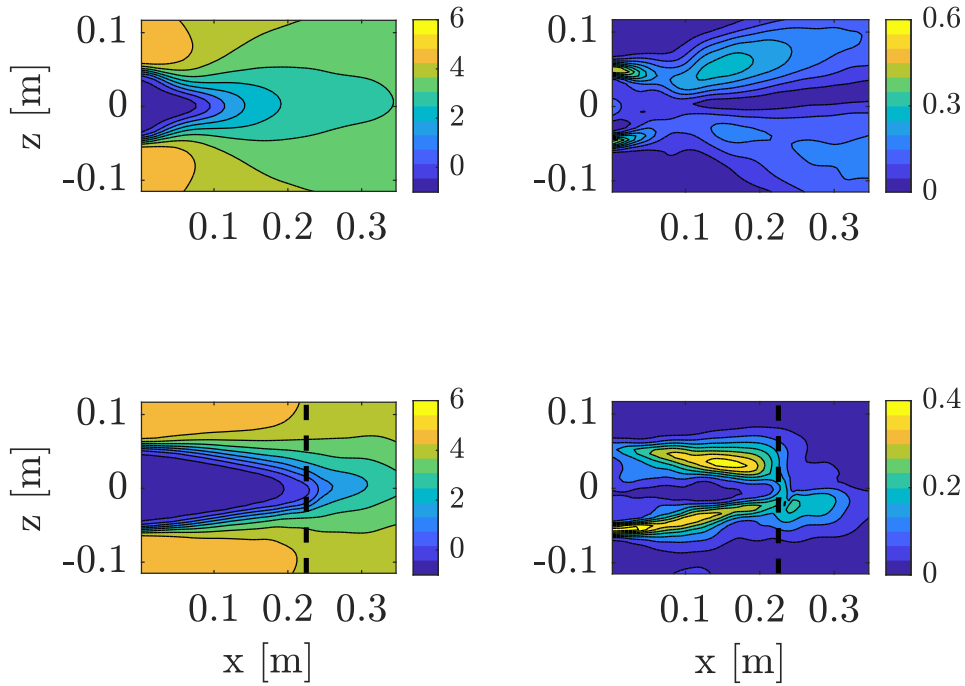


Figure 6.1: The streamwise mean and standard deviation for the case $Re = 25,700$ (*Top: Cylinder without Splitter Plate, Below: Cylinder with Splitter Plate*). The limits of the splitter plate have been marked with a black dashed line. The velocity values are in m/s.

Figure 6.2 shows the spanwise averaged transverse velocity component. For the cylinder without the splitter plate case, we see the hallmarks of vortex shedding, i.e., the two counter-sign regions with smaller structures at the base of the cylinder. These counter-sign regions contain the recirculation bubble that was alluded to earlier. These regions are periodically shed in the wake. However, in the presence of the splitter plate, this region has shifted further into the wake ($x = 0.25$ m) when compared to the pure cylinder case ($x = 0.1$ m). Additionally, the plate motion causes a wedge between the counter-sign regions. The near wake structures which are observed in the pure cylinder region are affected by the splitter plate. This is due to the fact that the communication of the shear layers as well as the crossflow is inhibited. Additionally, the counter-sign regions appear to be slightly elongated in the case of the splitter plate [12]. When looking at the standard deviations, the region of fluctuations has also shifted further downstream due to the influence of the splitter plate. In the case of the splitter plate, we can see that the region of maximum fluctuations has two short branches, likely due to the splitter plate motion in the wake. The right-hand branch is cannot be easily distinguished, and this can be attributed to the splitter plate affecting the visibility of the tracer particles causing the STB algorithm difficulties in tracking particles behind the splitter plate.

Overall, the splitter plate strongly affects the wake of the flow by disrupting the communication between the shear layers. As a result, the cross-flow and back-flow are inhibited and the vortex-shedding process is delayed and/or diminished [39].

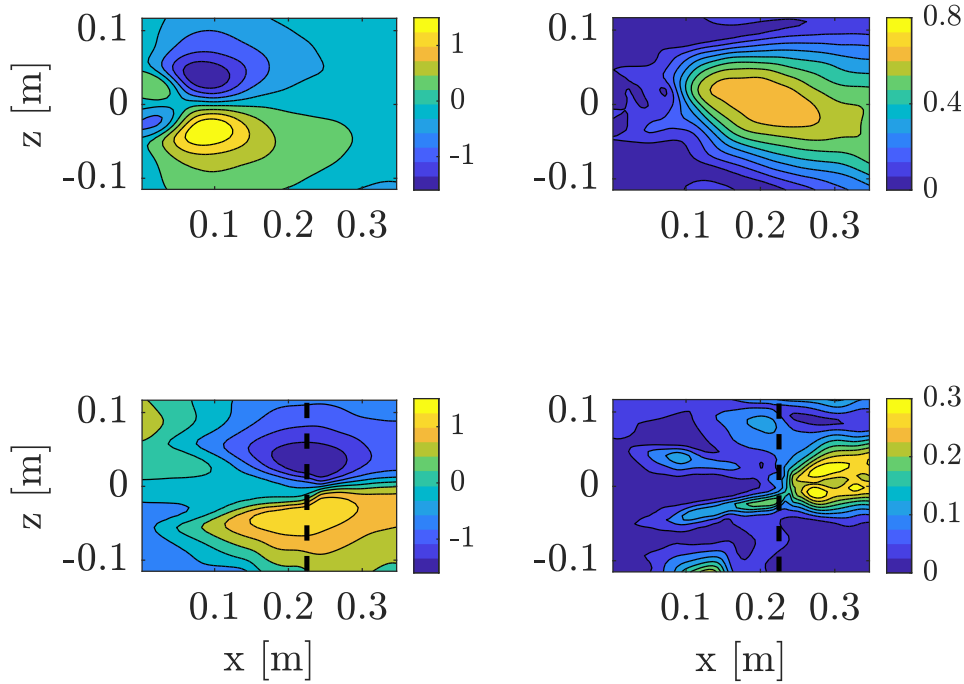


Figure 6.2: The transverse mean and standard deviation for the case $Re = 25,700$ (*Top: Cylinder without Splitter Plate, Below: Cylinder with Splitter Plate*). The limits of the splitter plate have been marked with a black dashed line. The velocity values are in m/s.

6.1.2. Time Series and Spectral Decomposition

In order to work out the influence of the splitter plate on the vortex-shedding process, we can look at the variation of the transverse velocity component with respect to time. The time series can provide insight into magnitude reduction or increase in the magnitude of the velocity component as well as provide the signal to identify the frequency content. The frequency content of this series can be observed by looking at the power spectral density, which indicated the frequency of the vortex-shedding process. Although the duration of the measurement time is 5 seconds, for the sake of clarity, Figure 6.3 has been plotted for 1 second. This is followed by the other time series in this section.

For the instantaneous time signal, we can see that the time series for the cylinder (*blue curve*) flow is fairly periodic. This is to be expected as the vortex shedding of a plain cylinder is periodic in the sub-critical regime [29]. A section of aperiodic behavior is observed between 250 ms to 450 ms. As the cylinder wake is expected to be periodic, this section can be explained by poor interpolation due to binning, or just experimental error. On the other hand, the time series of the cylinder with the splitter plate (*red curve*) does not show the same periodicity with the overall magnitude of the oscillations being lower. The fluctuations are more intense in the case of the splitter plate, highlighting its effect on the vortex-shedding process of the cylinder.

This conclusion is backed up by looking at the power spectral density plot. The blue curve represents the PSD of the cylinder without the splitter plate and shows a strong peak at the

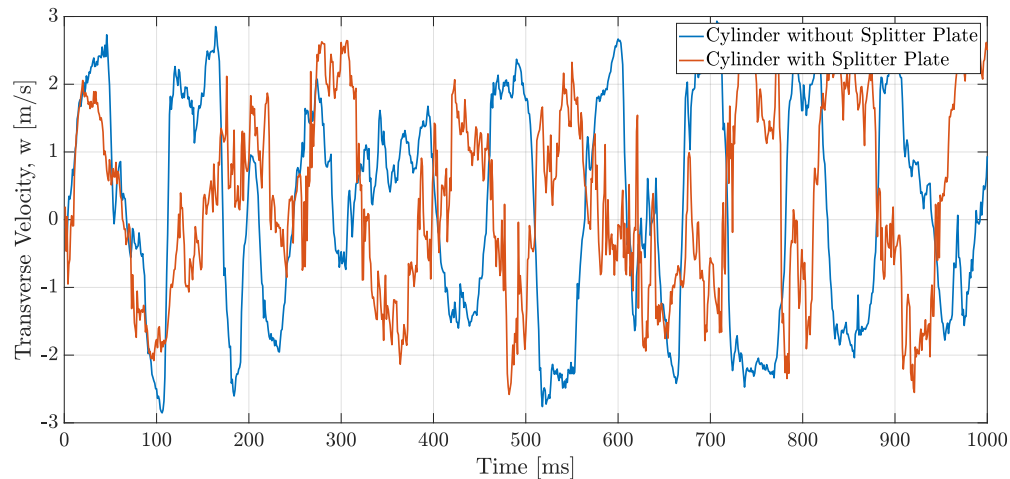


Figure 6.3: Time series of instantaneous transverse velocity at the point $x = 0.3089$ m, $y = 0.0179$ m, and $z = -0.0019$ m for the case $Re = 25,700$ (Blue: *Cylinder without Splitter Plate*, Red: *Cylinder with Splitter Plate*)

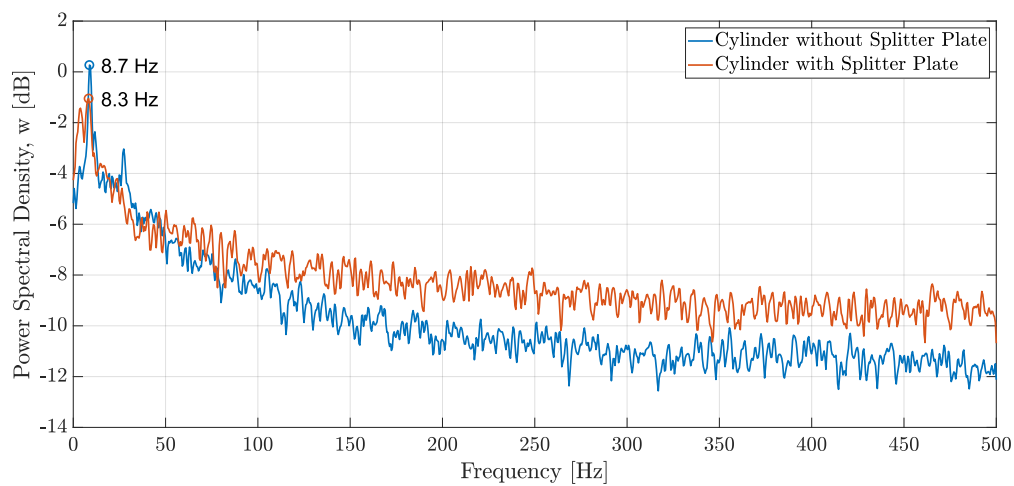


Figure 6.4: Power spectral density of instantaneous transverse velocity at the point $x = 0.3089$ m, $y = 0.0179$ m, and $z = -0.0019$ m for the case $Re = 25,700$ (Blue: *Cylinder without Splitter Plate*, Red: *Cylinder with Splitter Plate*)

frequency of $f \approx 8.7$ Hz which corresponds to a Strouhal number of $St \approx 0.2$, which is consistent with literature [77]. Additionally, the blue curve shows a secondary peak at $f \approx 27.34$ Hz, underlining the higher harmonics of the vortex shedding phenomenon. The red curve of the splitter plate however indicates different vortex dynamics. The single sharp peak is replaced by multiple lower-intensity peaks, indicating that the splitter plate affects the vortex-shedding process. The splitter plate PSD plot shows higher intensity at high frequencies, indicating the splitter plate is adding energy to the smaller turbulence scales. The highest peak of the splitter plate

From Figure 6.5, we see the influence of the splitter plate on the spanwise coherence of the vortices shed by the cylinder. As expected, there is a strong spanwise coherence in the case of the cylinder with no splitter plate [81]. Since the splitter plate is absent, the shear layers can freely interact and develop into what Wu et al. [81] call "shear aligned vortices", which are vortex tubes being stretched out by consecutive Strouhal vortices. These vortices or vortex

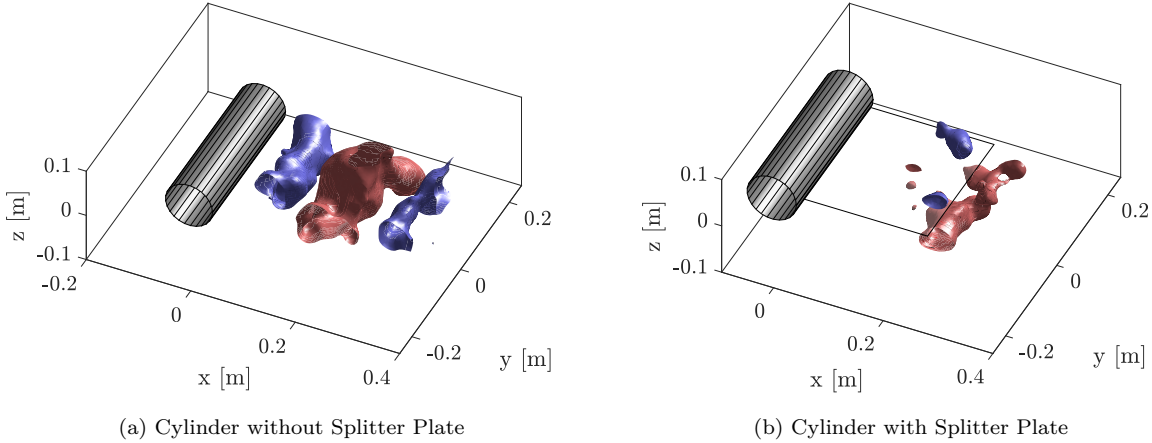


Figure 6.5: Isosurfaces highlighting the spanwise coherence of the transverse velocity $w = 2$ m/s (in blue) and $w = -2$ m/s (in red) for the case $Re = 25,700$. The splitter plate has been shown in its neutral position.

tubes are shed alternately as seen by the red and blue isosurfaces of the transverse velocity of ± 2 m/s. The blue and red coloring of the isosurface highlights the sense of the rotation of the vortex, but the magnitude of the transverse component remains the same. On the other hand, the splitter plate seems to disturb the spanwise coherence breaking up the vortices being formed. The splitter plate influences the shear layer processes of cross-flow and entrainment, which causes the break up of coherent structures into smaller scales of turbulent structures. This also confirms the earlier observation of the increased high-frequency contribution in the PSD of the wake with the splitter plate.

6.1.3. Proper Orthogonal Decomposition

POD is performed on the velocity fields to identify flow structures and their associated energy content. By performing such an analysis we can see how the splitter plate is coupled with the flow, i.e how the splitter plate affects the symmetry and coherence of the wake.

Figure 6.6 shows the energy content of the first 10 modes after performing POD on the experimental data. From the figures, we can see that the splitter plate has a clear influence on the Karman vortex shedding. In the case of the cylinder without the splitter plate, the first two modes dominate the energy content in the streamwise and the transverse directions and contain almost 80% of the energy. On the other hand, the first two modes of the splitter plate have lower energy content. Additionally, the higher modes of the splitter plate carry more energy than the cylinder without the splitter plate suggesting that the energy is being transferred from the higher modes. This is observed by looking at the power spectral density, although, this can also be an artifact of the flow structures not being fully captured. The latter seems to be the better argument as the difference between the first and second modes is almost 150% in the streamwise direction and 80% in the transverse direction. This can be attributed to the wake structures being pushed out of the domain being analyzed by the splitter plate. To verify this claim, the flow modes in the two velocity directions can be looked at.

Figure 6.7 shows the mode shapes in the streamwise direction. The top row shows the mode shapes of the cylinder, while the bottom row visualizes the mode shapes of the cylinder with the splitter plate. We can see that the mode shapes are markedly different due to the influence of the splitter plate. The first two modes of the cylinder without the splitter plate show the

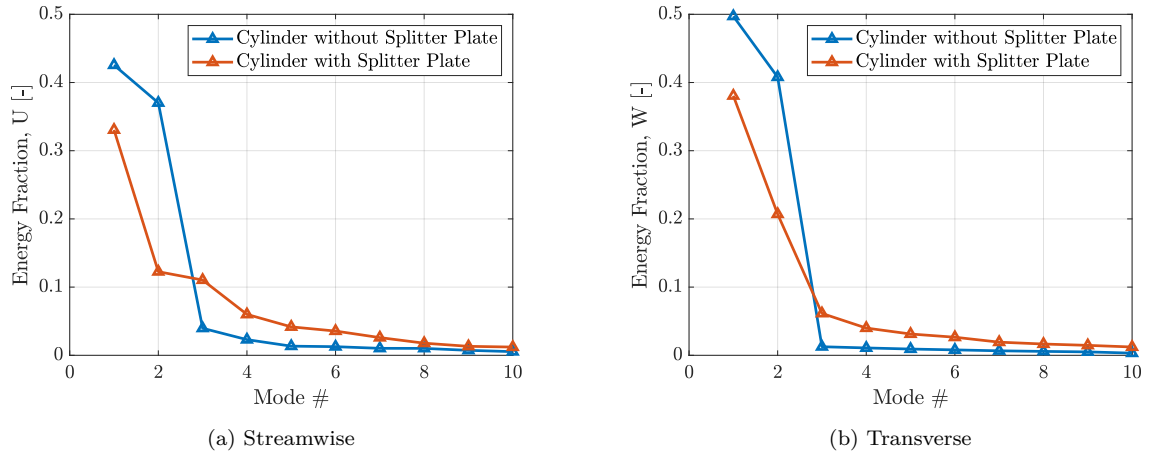


Figure 6.6: Energy distribution over the first ten modes for the case $Re = 25,700$

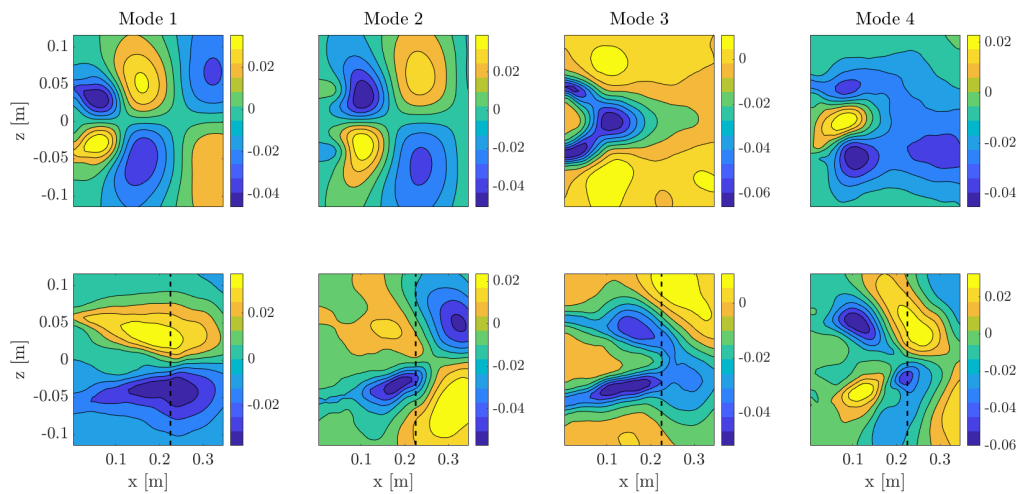


Figure 6.7: The first four streamwise mode shapes for the case $Re = 25,700$ (Top: *Cylinder without Splitter Plate*, Below: *Cylinder with Splitter Plate*). The limit of the splitter plate has been marked with a black dashed line. All the velocity values are in m/s.

vortex roll-up and vortex shedding process. The shedding is periodic, symmetrical, and in quadrature of phase. These flow structures are altered by the presence of the splitter plate in the wake with the regular vortex shedding pattern replaced by two large 'blobs', indicating that the roll-up of vortices happens along the length of the plate [12]. The second mode appears to be similar to the first two modes of the cylinder case with structures being shifted to the back of the splitter plate. Some of these structures are incomplete in the case of the splitter plate, this is the reason for the precipitous drop in the energy content seen in Figure 6.6a. The third mode also appears to be stretched by the splitter plate. The higher streamwise modes for the splitter plate show smaller alternating structures which bear weak similarities to the second mode of the cylinder without the splitter plate case, indicating some impacted vortex shedding.

The mode shapes in the transverse direction show the convection of the alternating vortices in the wake. The modes for the cylinder without the splitter plate show well-defined regions with strong positive and negative regions of the transverse velocity component representing

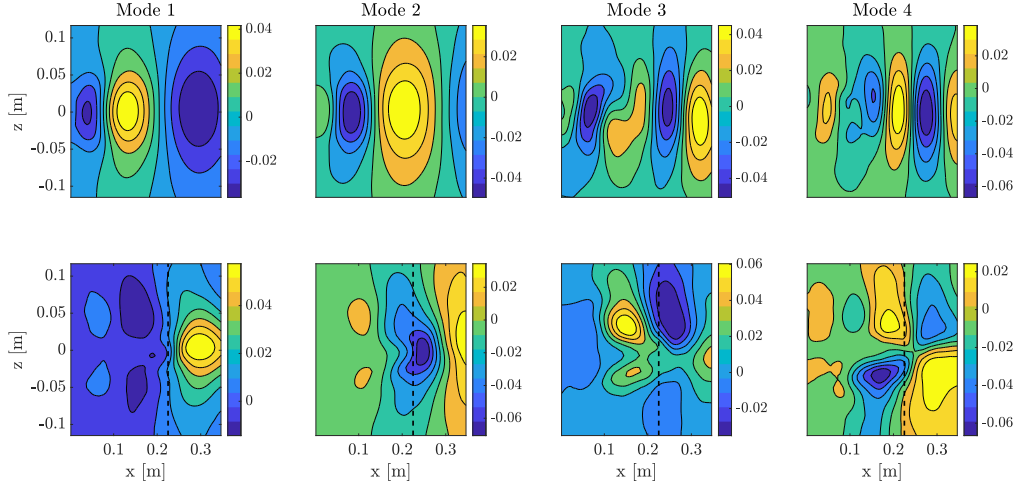


Figure 6.8: The first four transverse mode shapes for the case $Re = 25,700$ (*Top: Cylinder without Splitter Plate, Below: Cylinder with Splitter Plate*). The limits of the splitter plate have been marked with a black dashed line. All the velocity values are in m/s.

periodic shedding. Additionally, it is observed the higher modes (modes 3 and 4) show the higher harmonics of the first pair. This is also observed in the PSD plot as the secondary peak. The regular vortex-shedding process is interrupted by the splitter plate. With the formation and roll-up of vortices delayed as seen previously, these vortices are now being convected from the tip of the splitter plate, with a few smaller structures developing on either side. In the second mode, the counter-sign regions leave the domain which explains the drop in energy content. The higher modes show a random distribution of the structures, with no straightforward interpretation.

6.2. Reduced Amplitude Regime, $Re = 44,100$

This section deals with the results of the reduced amplitude regime. In order to derive meaningful conclusions, the results are compared to the baseline. In this regime, it was observed that the amplitude was distinctly reduced from the baseline splitter plate oscillations (Figure 4.6). It was also observed that the splitter plate motion was increasingly three-dimensional due to torsional motion.

6.2.1. Statistical Analysis

With an increase in the freestream velocity, the recirculation region for the cylinder increases with a distinct recirculation bubble forming. Consequently, the magnitude of the fluctuations is also higher at the base of the cylinder. As was the case with the baseline, the presence of the splitter plate in the near wake elongates the recirculation region as the formation region is affected. We can also observe that the recirculation region has extended well beyond the splitter plate [20, 39]. When compared to the baseline, the tip of the splitter plate was the limit of the recirculation region. An interesting point to note is the presence of a high-velocity region at the base of the cylinder in the case of the splitter plate. As explained in Chapter 5 in the section regarding the development of STB tracks, the distribution of structural markers on the splitter plate led to the development of spurious vectors with nonphysical accelerations. In order to combat this, the pre-processing kernel size had to be changed in order to remove the bad vectors, however, all the bad vectors could not be eliminated. The wake of the cylinder with a splitter plate is expected to have a pronounced region of low velocity, as can be seen

in the baseline. As a result, the fluctuations are also concentrated at the base of the cylinder and splitter plate.

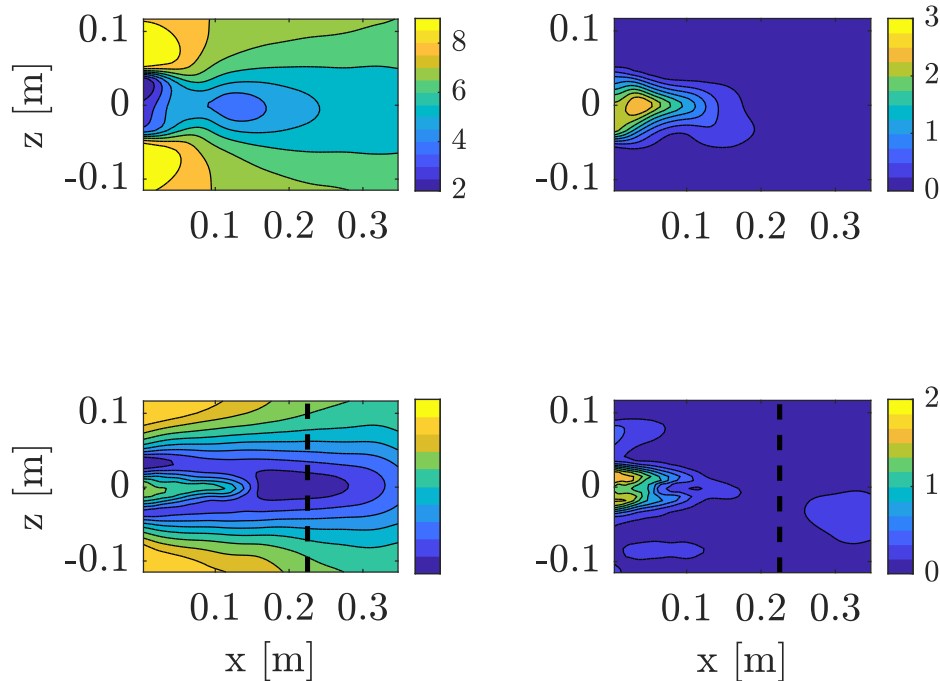


Figure 6.9: The streamwise mean and standard deviation for the case $Re = 44,100$ (*Top: Cylinder without Splitter Plate, Below: Cylinder with Splitter Plate*). The limits of the splitter plate have been marked with a black dashed line. The velocity values are in m/s.

The effect on the near wake can be especially understood by looking at the transverse velocity component. Figure 6.10 shows the mean and the fluctuations associated with the transverse velocity component. In both cases, we can see the regions of the counter-rotating signs, which represent the containment of the recirculation bubble. The cylinder without the splitter plate case shows the characteristics of periodic vortex shedding and is consistent when compared to the baseline. In the case of the splitter plate, these regions are more elongated and displaced slightly backward by the presence of the splitter plate. The splitter plate also affects the development of the near-wake counter-sign structures. When comparing it to the baseline, we can see that at a higher freestream velocity, the counter-rotating regions have shifted inboard and closer to the splitter plate ($x \approx 0.15$). The inboard movement of the counter-sign regions coupled with their magnitude increase could explain the reduction in amplitude of the splitter plate oscillations. This is different from the wedge that is observed in the baseline case due to the splitter plate motion. As a result of this, the fluctuations are also reduced and are concentrated along the length of the splitter plate.

6.2.2. Time Series and Spectral Decomposition

We can now investigate the instantaneous flow data. The magnitude of the transverse velocity component is plotted against the time of observation as seen in Figure 6.11. As expected, the cylinder without the splitter plate (*blue curve*) case shows periodic behavior that

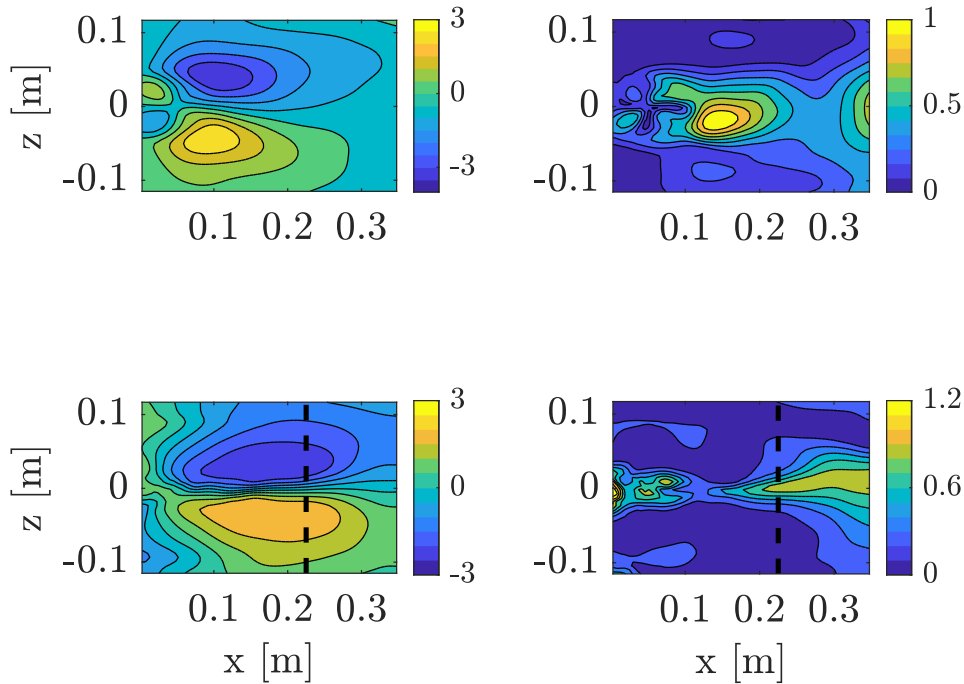


Figure 6.10: The transverse mean and standard deviation for the case $Re = 44,100$ ((*Top: Cylinder without Splitter Plate, Below: Cylinder with Splitter Plate*). The limits of the splitter plate have been marked with a black dashed line. The velocity values are in m/s.

is consistent with the vortex shedding process [29]. It is interesting to observe that the wake behavior due to the presence of the splitter plate (*red curve*) also appears to be periodic with a frequency that is lower than that of the plain cylinder (approximately half the frequency). The reduced splitter plate oscillations cause the wake to be more structured and ordered. This is in contrast to the wake behavior of the baseline splitter plate, which shows more aperiodic behavior with damped-out magnitude and increased fluctuations. Additionally, the amplitude of the oscillation is larger with an increased freestream velocity at ± 4 m/s.

The observations of the time series plot can be corroborated by looking at the spectral content of the signal. The periodic behavior of the wake can be seen as strong peaks in the power spectral density in Figure 6.12. The cylinder shows a peak of about 15.63 Hz, which gives a corresponding Strouhal number of ≈ 0.2 , as expected. The splitter plate on the other hand has a peak at about 8.3 Hz, which is half the value of the cylinder without the splitter plate. This could be likely due to the increased length of the formation region due to the plate. This reduction in frequency and a general reduction in Strouhal number was noted by Roshko [56]. The magnitude of the peak is also significantly reduced, while the contribution of the higher frequencies is slightly increased. This shows that the energy is being transferred by the splitter plate to the smaller turbulent length scales, although not as much as the baseline. As a consequence, the vortex shedding process is inhibited by the splitter plate resulting in a reduction in the value of the Strouhal number to ≈ 0.1 . This is again reflected by the spanwise coherence of the wake structures seen in Figure 6.13. In the absence of the splitter plate, the wake shows strong spanwise coherence and alternating counter-sign structures being shed in

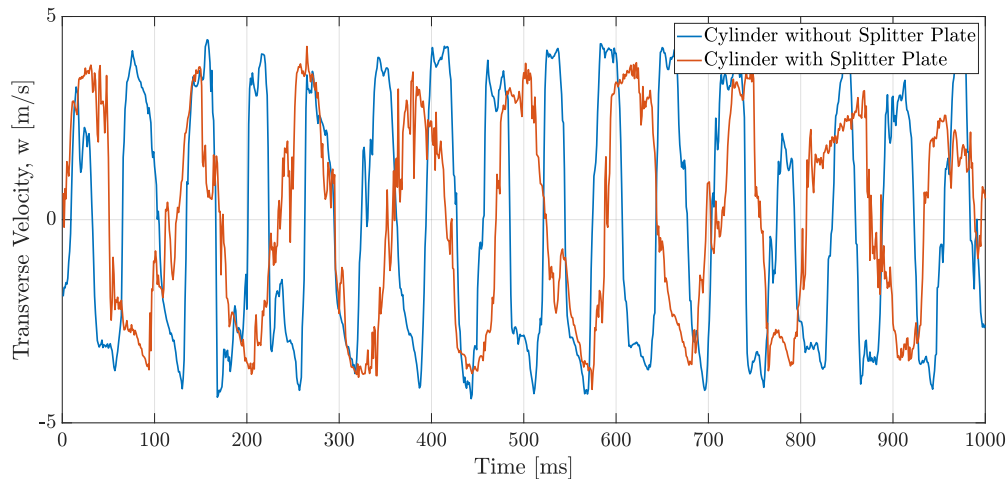


Figure 6.11: Time series of instantaneous transverse velocity at the point $x = 0.3089$ m, $y = 0.0179$ m, and $z = 0.0143$ m for the case $Re = 44,100$ (Blue: *Cylinder without Splitter Plate*, Red: *Cylinder with Splitter Plate*)

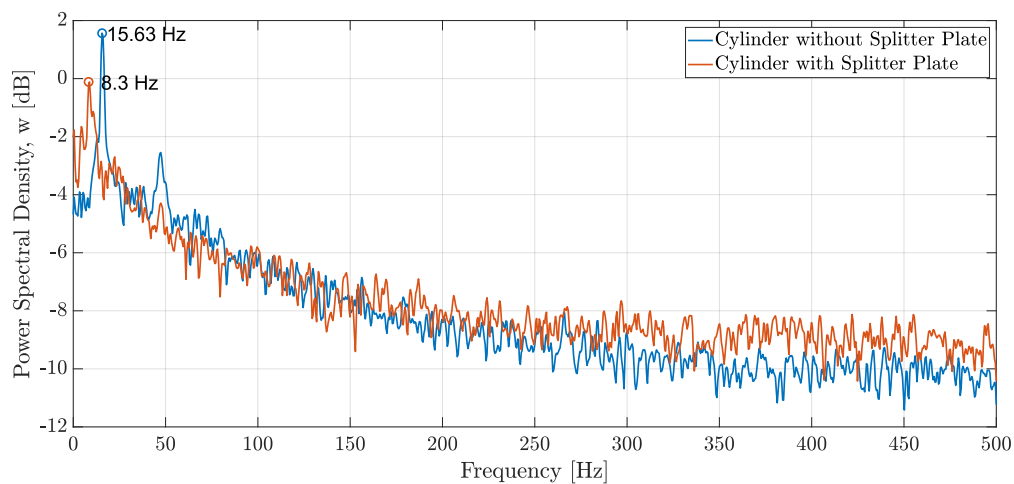


Figure 6.12: Power spectral density of instantaneous transverse velocity at the point $x = 0.3089$ m, $y = 0.0179$ m, and $z = 0.0143$ m for the case $Re = 44,100$ (Blue: *Cylinder without Splitter Plate*, Red: *Cylinder with Splitter Plate*)

the wake [81]. On the other hand, the splitter plate shows an impaired spanwise coherence with smaller structures also being present in the wake. This is consistent with the observations of the power spectral density. Additionally, the separation of the large spanwise structures can be compared to the time series which shows a reduction in the frequency of the transverse velocity component.

6.2.3. Proper Orthogonal Decomposition

Performing POD on the reduced amplitude case's data set reveals the flow structures' energy content. In the case of the cylinder without the splitter plate, in the streamwise direction, the energy is concentrated in the first two modes which contain about 70% of the total energy. On the other hand, the splitter plate carries significantly lower energy in the first two modes, with the energy being redistributed to the higher modes. This however could be an artifact of the reduced spatial resolution due to the structural marker problem that was alluded to earlier. In the transverse direction, the first two modes of the cylinder without the splitter

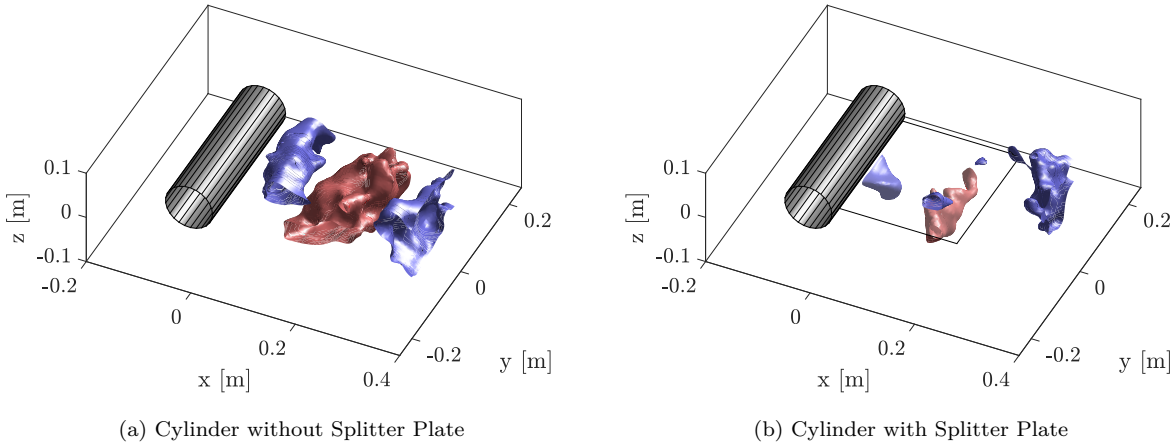


Figure 6.13: Isosurfaces highlighting the spanwise coherence of the transverse velocity $w = 3$ m/s (in blue) and $w = -3$ m/s (in red) for the case $Re = 44,100$. The splitter plate has been shown in its neutral position.

plate contain about 90% of the energy, while the splitter plate also shows increased energy in the transverse direction. This also confirms the periodicity seen in the time series and power spectral densities. The large difference between the first two modes of the splitter plate flow case is because large energy structures might not be captured by the domain.

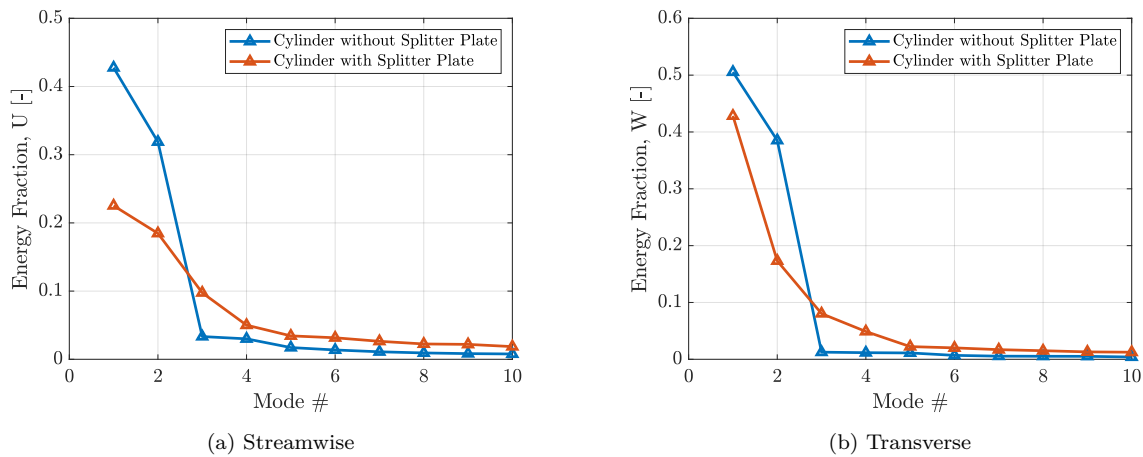


Figure 6.14: Energy distribution over the first ten modes for the case $Re = 44,100$

The streamwise mode shapes in Figure 6.15 show the roll-up and vortex formation of the cylinder and splitter plate flow cases. The cylinder without the splitter plate case shows the expected roll-up of vortices which are alternating signs. The first two modes are also in quadrature of phase. Hence, it is not that different from the baseline cylinder without the splitter plate case and indicated unaffected vortex shedding. The splitter plate flow case shows that the counter-sign regions have been shifted backward, behind the plate. This indicates that the roll-up of the shear layers into vortices happens beyond the splitter plate as a result of reduced oscillations and reduced communication between the layers [12]. When comparing the reduced amplitude splitter plate to the baseline, the large blobs on either side of the plate, of the first mode have been replaced by smaller blobs. Additionally, the reduced amplitude case splitter plate shows some near wake structures involved in vortex shedding which are

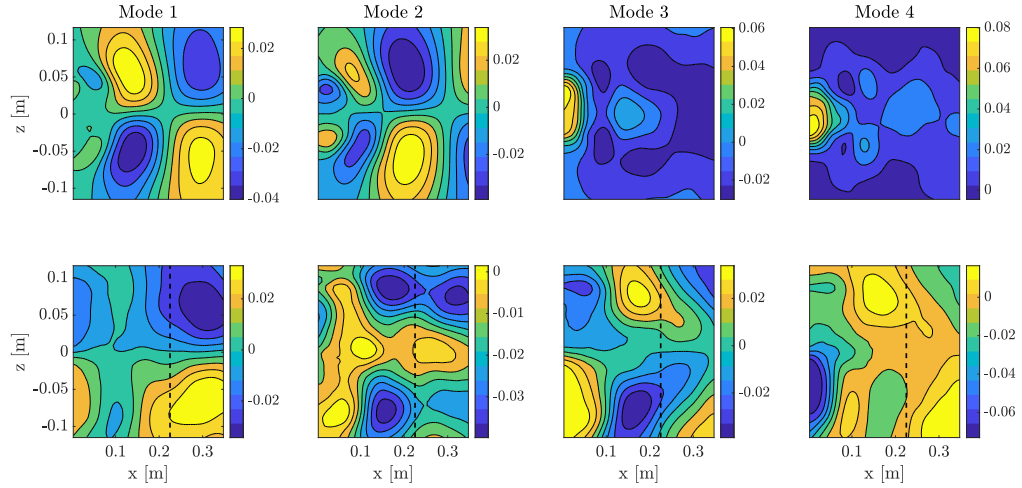


Figure 6.15: The first four streamwise mode shapes for the case $Re = 44,100$ (*Top: Cylinder without Splitter Plate, Below: Cylinder with Splitter Plate*). The limits of the splitter plate have been marked with a black dashed line. The velocity values are in m/s.

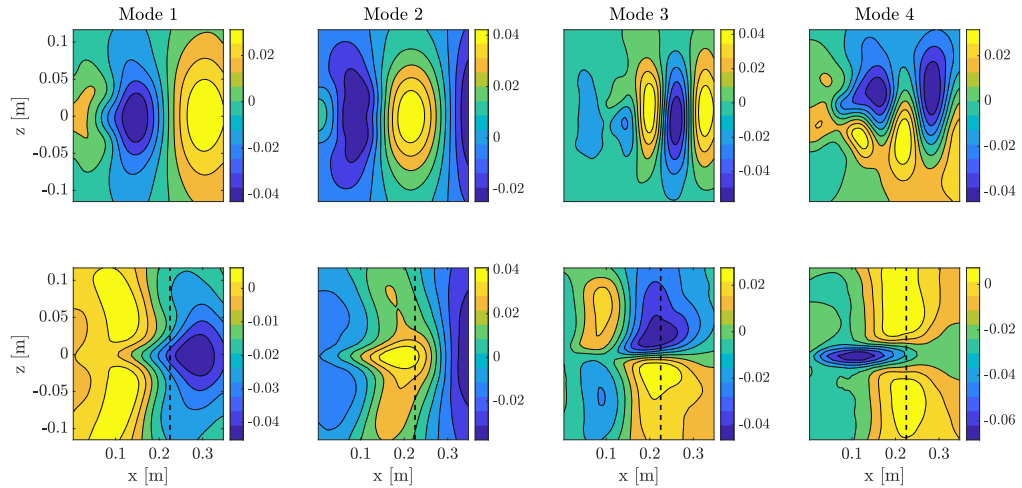


Figure 6.16: The first four transverse mode shapes for the case $Re = 44,100$ (*Top: Cylinder without Splitter Plate, Below: Cylinder with Splitter Plate*). The limits of the splitter plate have been marked with a black dashed line. The velocity values are in m/s.

noticeably absent in the baseline. The higher modes of the splitter plate flow show the random distribution of flow structures which makes it difficult to draw any concrete interpretations. The random distribution of the structures can be attributed to the fact that there is a loss of some spatial resolution due to the structural marker issue discussed in the data processing chapter.

Figure 6.16 shows the mode shapes of the transverse velocity component. The transverse velocity represents the convection of the alternating vortices that are shed from the cylinder. In the case of the cylinder without the splitter plate, we see that strong alternating counter sign regions show the convection of the periodic vortices in the wake. Modes three and four of this case highlight the higher harmonics which is also seen as a secondary peak in the PSD plot. The presence of the splitter plate delays the vortex-shedding process to the tip of the splitter plate. However, the reduced amplitude case shows more near-wake structures when compared

to the baseline in the first two modes. This is the result of the low-frequency oscillations of the splitter plate which does not interfere much with the formation process and allows the development of some near-wake structures. These structures appear to have a resemblance to the first two modes of the cylinder without the splitter plate contributing to the relative periodicity of the wake, albeit influenced by the splitter plate. The counter-sign regions that leave the domain due to the splitter plate are not captured by the POD, contributing to the large drop in the energy content between the first and second modes. The higher modes of the splitter plate flow do not represent any higher harmonics as they are not very coherent and no real conclusions can be drawn from them.

6.3. Chaotic Regime, $Re = 68,600$

As the final part of the results section, the chaotic regime will be compared to the baseline. In the chaotic regime, the splitter plate motion was fully three-dimensional. The bending motion was coupled with large amounts of torsion. As described before, the long splitter plate was subject to *burst motions*, which were short periods of resonant splitter plate motion. A burst or resonant motion of the plate is characterized by the reduction in the three-dimensional motion of the plate. Consequently, the splitter plate motion becomes two-dimensional leading to coherent, low frequency, high amplitude motion. However, this motion of the splitter plate is not sustained for a long duration and the splitter plate eventually breaks out of the resonant motion and returns to its original chaotic state. As mentioned before, the burst would occur at random for different velocities making it very hard to capture. However, for the chaotic regime, the burst motion was captured and will be analyzed alongside the regular chaotic motion of the foil and the cylinder without the splitter plate. In order to make the distinctions clear, first the cylinder without the splitter plate and the chaotic regime will be discussed and then the notion of the resonant motion will be introduced.

6.3.1. Statistical Analysis

The wake of the cylinder without the splitter plate shows a short recirculation bubble, and the fluctuations represent the shear layers that form the edge of the bubble. The cylinder without the splitter plate does not show any significant differences in structure when compared to the baseline. As expected, the presence of the splitter plate elongates the recirculation region as well as the shear layers [20, 39, 57]. This is because the splitter plate interferes with the entrainment and crossflow processes of the shear layer which are responsible for the replenishment of the fluid in it [12]. In the case of chaotic splitter plate motion, the spatial resolution of the shear layer is affected as large three-dimensional oscillations interfere with the camera and STB algorithm. Comparing the chaotic splitter plate motion to the baseline, we see a similar elongation so the recirculation bubble and shear layers. However, we note that the shear layers have reduced in length, this is likely due to higher oscillations of the plate which allow more communication between the shear layers.

As the flow is still in the sub-critical regime, the cylinder still shows regular vortex shedding [29]. The cylinder without the splitter plate case reveals two counter-sign regions that contain the recirculation bubble. Additionally, the cylinder without the splitter plate case shows structures in the near wake that are consistent with the baseline, indicating roll-up and vortex formation. On the other hand, the regular chaotic splitter plate motion appears to elongate the counter-sign regions along the length of the plate. The counter-sign regions have also been shifted rearwards due to the near wake interference of the plate. The lengthening of these counter-sign regions can be attributed to the fact that they need to keep a longer recirculation bubble in place. These effects are quite similar to those observed in the baseline case as well

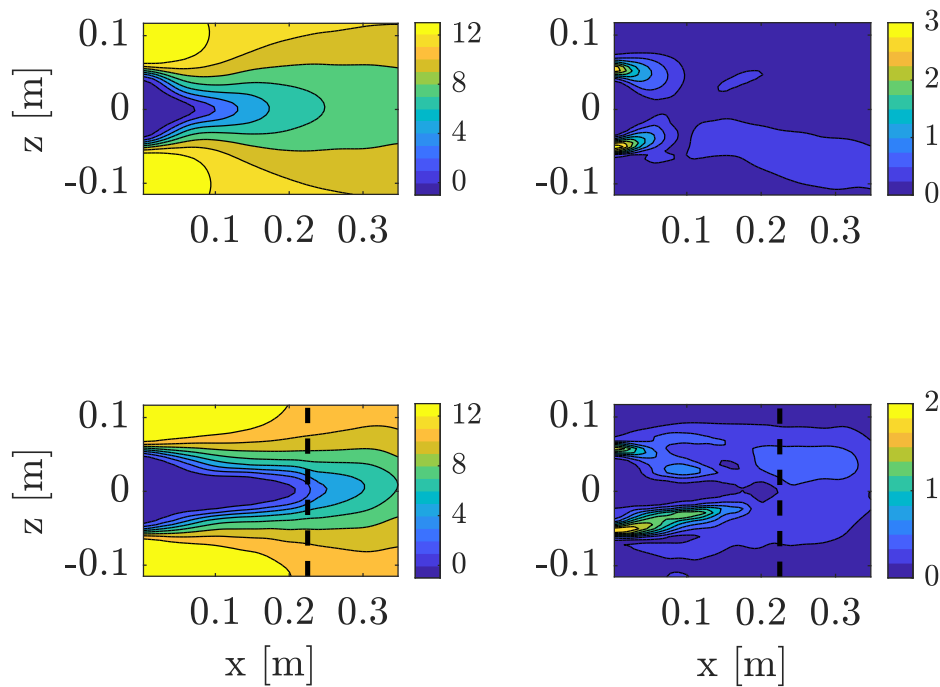


Figure 6.17: The streamwise mean and standard deviation for the case $Re = 68,600$ (*Top: Cylinder without Splitter Plate, Below: Cylinder with Splitter Plate*). The limits of the splitter plate have been marked with a black dashed line. The velocity values are in m/s.

as the reduced amplitude regime. The large amplitude of the chaotic motion also causes a wedge, which causes the spreading out of any near-wake counter-sign regions. The presence of the splitter plate also reduces the fluctuations that are now further into the wake as compared to the cylinder without the splitter plate case. Having understood the influence of the splitter plate on the wake in the chaotic regime, we can now look at the plate motion under resonance or a *burst*.

Resonant Motion

In the resonant case, the three-dimensional motion of the plate is replaced by large amplitude two-dimensional oscillations. As a result of this, the recirculation bubble shortens to a region between the cylinder without the splitter plate and chaotic plate cases. The reduction of the bubble can be explained by increased communication between the shear layers, as evidenced by the shortened fluctuations [57]. Additionally, there is a presence of a smaller recirculation bubble in the region. It is also observed that there are some large fluctuations in the resonant case, in the region of $x = 0.05$ m and $x = 0.2$ m, $z = -0.1$ m, and $z = -0.05$ m. These are artifacts of the large deflections of the splitter plate. In some instances, the splitter plate leaves the measurement domain, which manifests itself in large fluctuations in velocity. This is also corroborated by the increased magnitude of the fluctuations in the region. The transverse velocity component reveals that the elongated counter-sign regions have shortened significantly and are also asymmetrically located in space. This is likely due to the large deflections of the splitter plate which significantly alters the regular vortex shedding phenomenon. The same artifacts of high fluctuations appear in the transverse velocity component as well. The artifacts are enhanced in magnitude and spatial presence, likely due to the large transverse oscillations

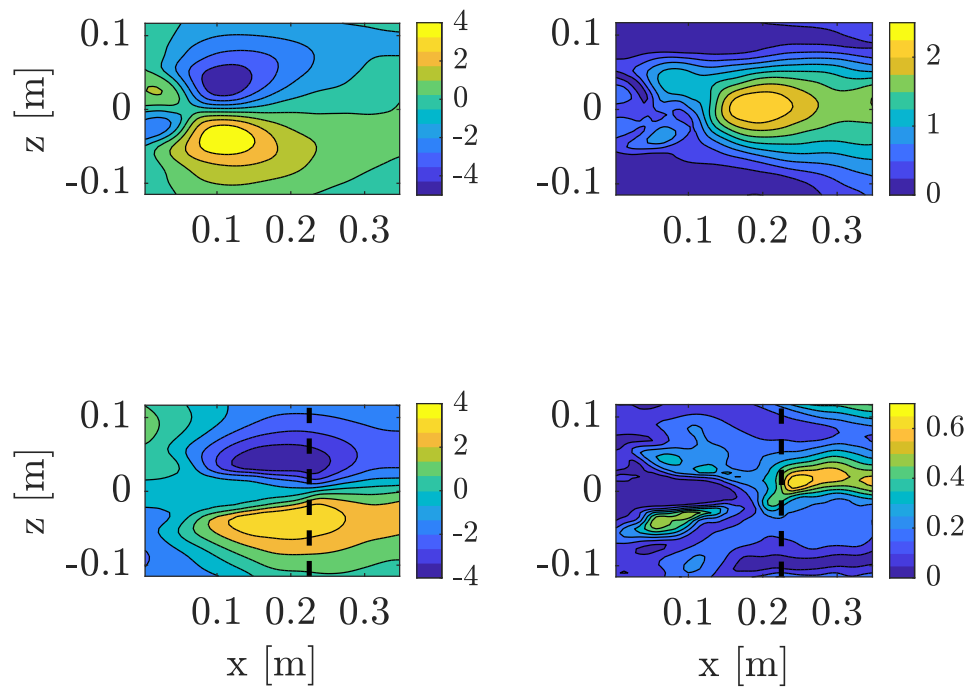


Figure 6.18: The transverse mean and standard deviation for the case $Re = 68,600$ (*Top: Cylinder without Splitter Plate, Below: Cylinder with Splitter Plate*). The limits of the splitter plate have been marked with a black dashed line. The velocity values are in m/s.

of the plate.

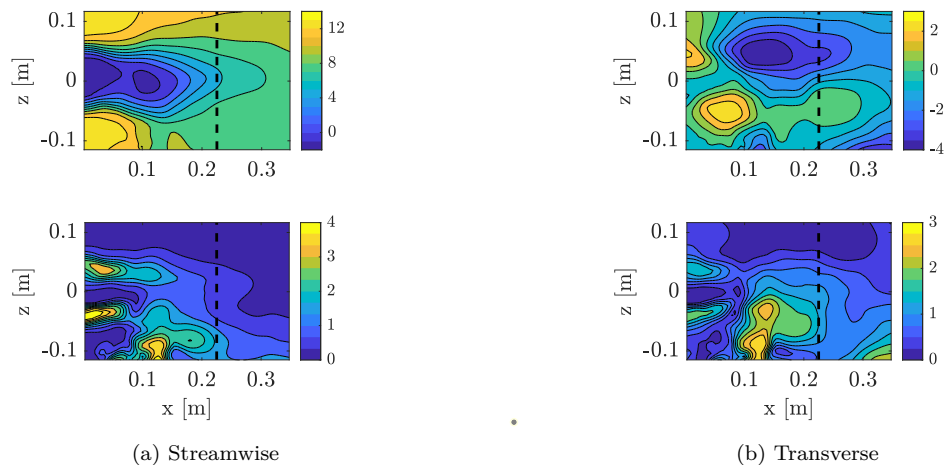


Figure 6.19: The streamwise and transverse mean and standard deviation for the case $Re = 68,600$ (*Top: Mean, Below: Standard Deviation*). The limits of the splitter plate have been marked with a black dashed line. The velocity values are in m/s.

6.3.2. Time Series and Spectral Decomposition

A time series can be generated by plotting the instantaneous behavior of the transverse velocity component in the wake against time measurement time. The cylinder without the splitter plate case reveals periodic variations in values of the transverse velocity component. The maximum amplitude of the oscillations is about ± 6 m/s. This is to be expected and is consistent with the baseline observation albeit with a different magnitude [29]. The chaotic motion of the splitter plate causes the wake to be severely affected. Large amounts of three-dimensional plate motion cause the wake to lose its periodicity and amplitude damped. This is reflected in the plot of the power spectral density, where the cylinder without the splitter plate case has a clear peak of 22.46 Hz which corresponds to an expected Strouhal number of ≈ 0.2 . The secondary peak observed is the contribution of higher harmonics, seen in the other cases as well. The splitter plate PSD does not show a single dominant peak, but a series of peaks at lower frequencies, highlighting the aperiodic behavior of wake. The highest frequency noted was 11.72 Hz, which is roughly half of that of the cylinder without the splitter plate. The PSD plot also reveals that the splitter plate has more high-frequency contribution than the cylinder without the splitter plate. The three-dimensional motion of the splitter plate breaks up the spanwise coherent vortex shedding into small structures. This observation is also consistent with the baseline. Figure 6.24 shows the isosurfaces of the tangential velocity component. For the cylinder, there is a great degree of spanwise coherence that can be seen. Figure 6.24a shows two counter-rotating vortices that have been shed into the wake. The large coherent structures are broken down into smaller structures by the splitter plate, alluded to earlier.

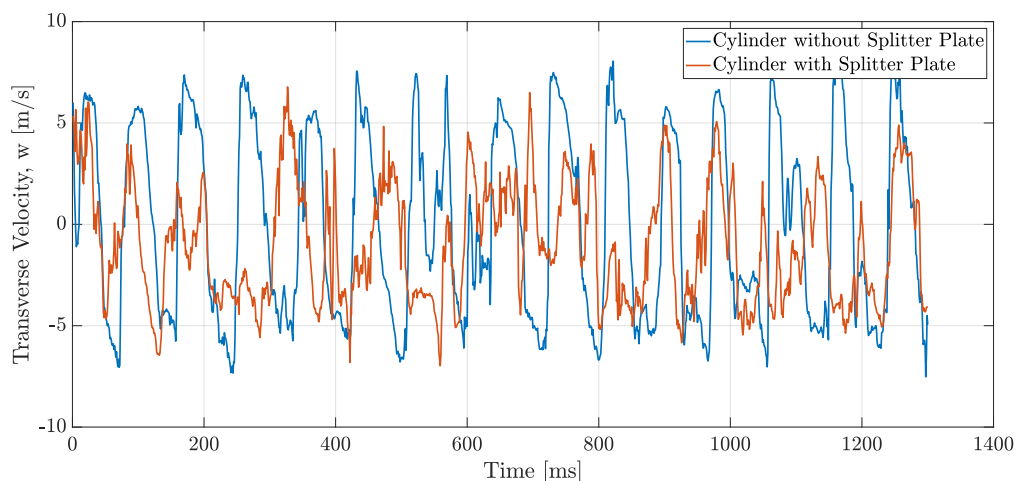


Figure 6.20: Time series of instantaneous transverse velocity at the point $x = 0.2927$ m, $y = 0.0395$ m, and $z = 0.0305$ m for the case $Re = 68,600$ with the regular chaotic motion of the splitter plate. (Blue: *Cylinder without Splitter Plate*, Red: *Cylinder with Splitter Plate*)

Resonant Motion

When the splitter plate experiences resonance, there is a dramatic change in the behavior of the wake. As the splitter plate undergoes high-amplitude, low-frequency oscillations, the transverse velocity increases significantly and the time series become very periodic. This is also a consequence of the splitter plate motion becoming increasingly two-dimensional. The magnitude of oscillations increases to about ± 10 m/s. Additionally, between 1200 and 1300 ms the end of the burst can be seen, where the coherence oscillations lose their periodicity and magnitude. This periodic behavior appears as a peak in the PSD plot (Figure 6.23). The peak frequency is roughly half of that of the cylinder without the splitter plate case at about 11.72

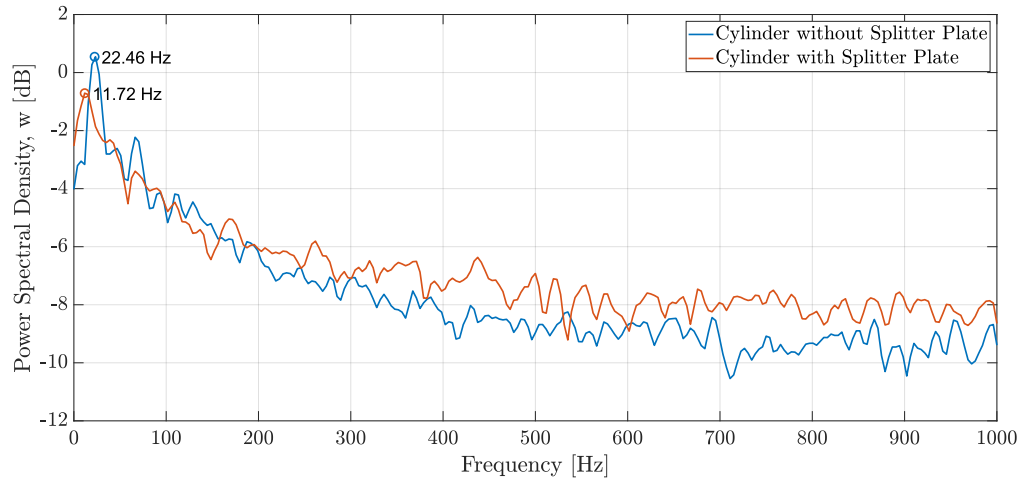


Figure 6.21: Power spectral density of instantaneous transverse velocity at the point $x = 0.2927$ m, $y = 0.0395$ m, and $z = 0.0305$ m for the case $Re = 68,600$ with the regular chaotic motion of the splitter plate. (*Blue: Cylinder without Splitter Plate, Red: Cylinder with Splitter Plate*)

Hz. It is interesting to note that this is the same value observed in the regular chaotic motion of the splitter plate, however, it is significantly higher during resonant motion. Additionally, this observation is similar to the reduced amplitude regime, where there is a tendency of the frequency oscillating wake with the splitter to be half [56], likely due to the delayed formation of the vortices and their convection. Additionally, the large oscillations of the plate could be a contributing factor. Another consequence of the resonance is the return of spanwise coherency in the wake due to the two-dimensional nature of the plate oscillations, as seen in Figure 6.24c. As a result, the resonant PSD does not show a significant contribution at high frequencies. Despite the wake being organized and periodic, the influence of higher harmonics cannot be observed in the PSD.

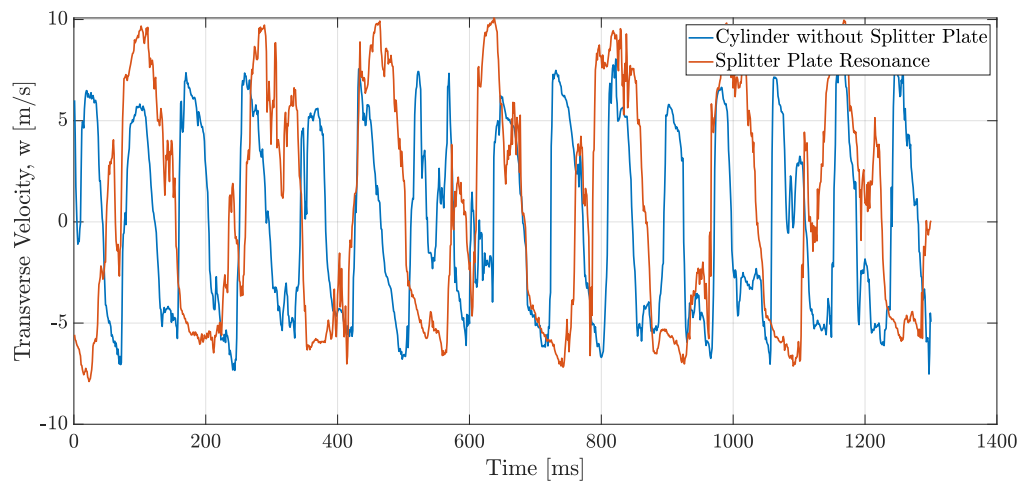


Figure 6.22: Time series of instantaneous transverse velocity at the point $x = 0.2927$ m, $y = 0.0395$ m, and $z = 0.0305$ m for the case $Re = 68,600$ for the resonant splitter plate motion. (*Red: Cylinder without Splitter Plate, Blue: Resonant Splitter Plate*)

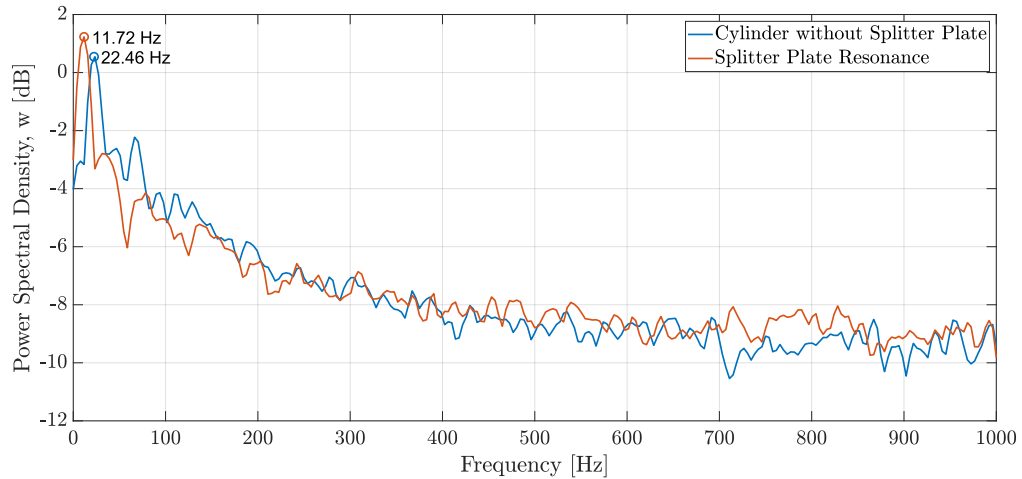


Figure 6.23: Power spectral density of instantaneous transverse velocity at the point $x = 0.2927$ m, $y = 0.0395$ m, and $z = 0.0305$ m for the case $Re = 68,600$ for the resonant splitter plate motion. (*Top: Cylinder without Splitter Plate, Below: Resonant Splitter Plate*)

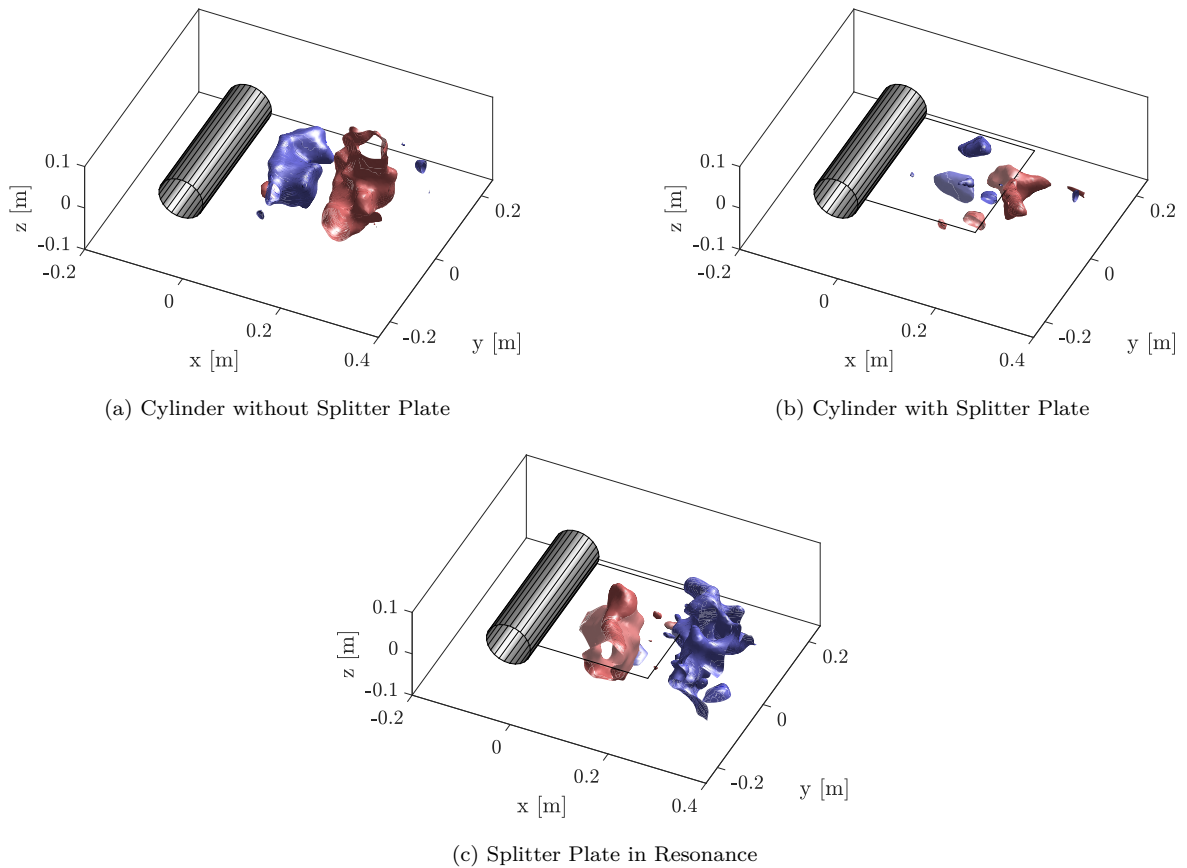


Figure 6.24: Isosurfaces highlighting the spanwise coherence of the transverse velocity $w = 5.5$ m/s (in blue) and $w = -5.5$ m/s (in red) for the case $Re = 68,600$. The splitter plate has been shown in its neutral position.

6.3.3. Proper Orthogonal Decomposition

The proper orthogonal decomposition of the flow data in the streamwise and transverse directions reveals the energy content of the flow as well as its associated mode shapes. Figure

6.25 shows the energy content of the first 10 energy modes.

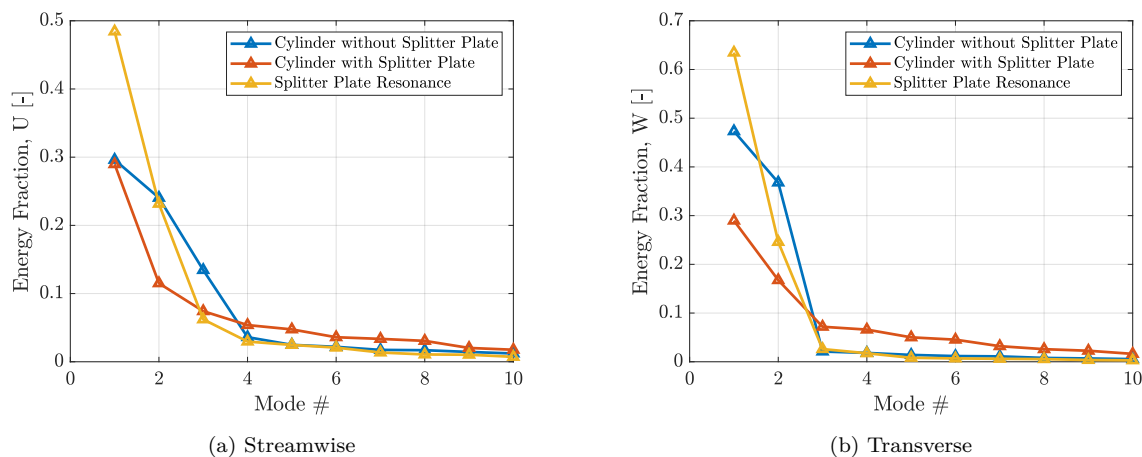


Figure 6.25: Energy distribution over the first ten modes for the case $Re = 68,600$

In the streamwise direction (Figure 6.25a), the cylinder without the splitter plate case shows that the energy content is concentrated in the first two modes, with decreasing contribution from the third mode. The first two modes contain roughly 55% of the total energy. The first mode of the splitter plate in chaotic motion contains roughly the same energy as that of the cylinder without the splitter plate. However, there is a precipitous drop in energy in the second mode, likely due to the fact that some of the wake structures have left the domain. This can also explain why the higher modes of the splitter have a slightly higher energy fraction when compared to the cylinder without the splitter plate. The first two modes appear to be in the quadrature of phase. The streamwise mode shapes describe the roll-up processes of the vortex formation. The cylinder without the splitter plate shows alternating counter-sign regions in the near and far wake, indicating normal vortex formation. This is consistent with the baseline and shows similar structures. The splitter plate disturbs the formation of the near wake structures while elongating some of the other structures. The large three-dimensional oscillations of the plate reduce the communication between the shear layers and affect the entrainment and formation of the vortices [39]. The second mode of the chaotic motion shows a resemblance with the second mode of the cylinder without the splitter plate, albeit the near wake structures are elongated. This further highlights the influence on the communication between the shear layers and periodic vortex shedding.

The transverse energy content of the cylinder without the splitter plate shows that roughly 80% of the energy is contained in the first two modes. The modes higher than them have only small contributions, indicating strong vortex shedding. On the other hand, there is a drop in energy content when looking at the splitter plate, highlighting the influence. The splitter plate affects the spanwise coherence and breaks the vortex tubes into smaller wake structures which distribute the energy to the higher modes. The mode shapes corroborate the picture presented by the energy content. The cylinder without the splitter plate mode shapes shows the convection of strong counter-sign vortices in the wake. The higher modes show the shedding frequency increasing and indicate the higher harmonics that can be seen as a secondary peak in the PSD plot. On the other hand, the shedding process is delayed to the tip of the splitter plate with some roll-up structures visible on either side of the plate. This is a consequence of the plate influencing the formation of vortices and the near wake.

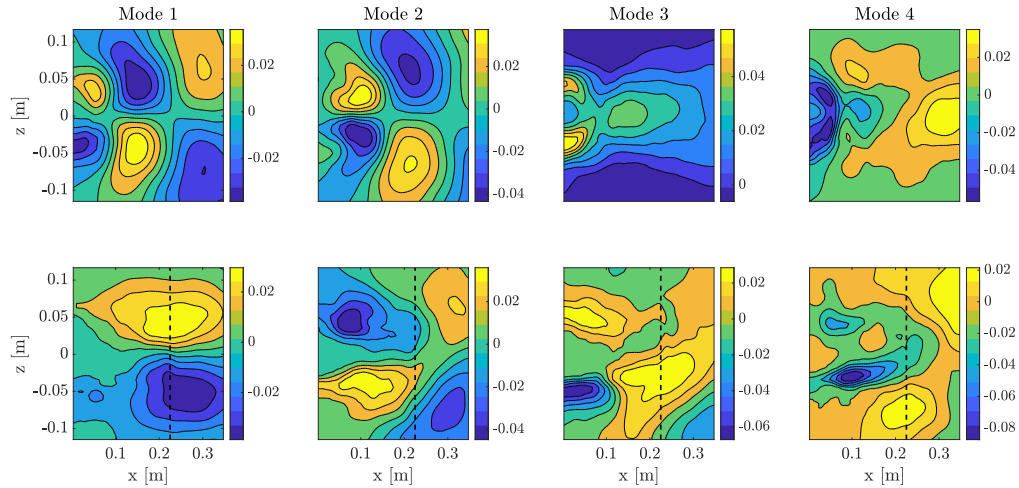


Figure 6.26: The first four streamwise mode shapes for the case $Re = 68,600$ (*Top: Cylinder without Splitter Plate, Below: Cylinder with Splitter Plate*). The limits of the splitter plate have been marked with a black dashed line. The velocity values are in m/s.

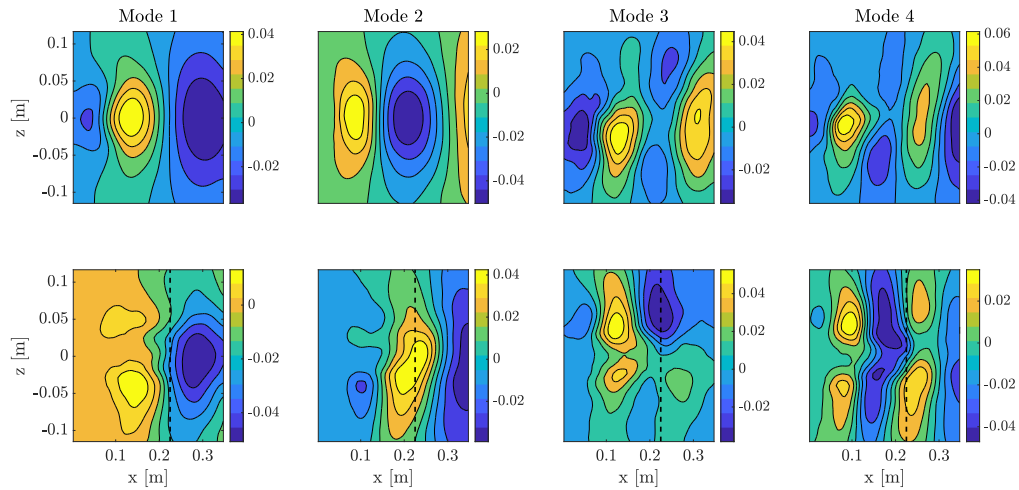


Figure 6.27: The first four transverse mode shapes for the case $Re = 68,600$ (*Top: Cylinder without Splitter Plate, Below: Cylinder with Splitter Plate*). The limits of the splitter plate have been marked with a black dashed line. The velocity values are in m/s.

Resonant Motion

The resonance causes the wake to undergo a dramatic transformation. In the streamwise direction, the resonant case shows that the first mode has the most energy when compared to the cylinder without the splitter plate and chaotic plate motion.

The energy is primarily contained in the first mode, with decreasing contributions from the higher modes. Unlike the case of the chaotic splitter plate, the higher modes of the resonant foil motion do not contribute more energy. This is also a consequence of the ordered nature of the wake and periodic vortex shedding. The mode shapes reveal a fundamental similarity to the mode shapes from the chaotic plate motion. Although it is quite visible that countersign regions have been spread apart significantly, likely due to the large oscillations of the splitter plate. This also along with the countersign regions leaving the domain explains the drop in energy content in the second mode. A similar observation can be made in the energy content

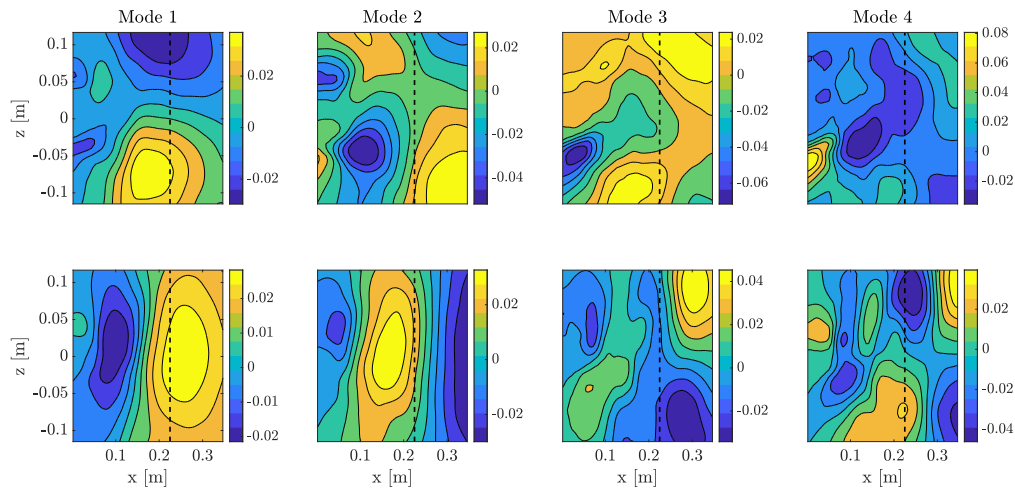


Figure 6.28: The first four streamwise and transverse mode shapes for the resonant splitter plate case $Re = 68,600$ (*Top: Streamwise Modes, Below: Transverse Modes*). The limits of the splitter plate have been marked with a black dashed line. The velocity values are in m/s.

in the transverse energy content. The resonant splitter plate carries significantly more amount of energy due to the high-amplitude low frequency oscillations. Due to the periodic vortex shedding as a result of the two-dimensional oscillations of the plate, the transverse mode shapes bear a closer resemblance to the cylinder without the splitter plate. The first two modes reveal large counter-sign regions which are convected into the wake. The higher resonant modes show a random distribution of wake structures and no real conclusion can be drawn from it, although the fourth mode shows the structures ordered in some form of a higher harmonic. However, this influence cannot be seen in the PSD plot as there are secondary peaks.

Conclusions and Recommendations

7.1. Conclusions

Through the experiments performed and the subsequent analysis of data, it is evident that the flexible splitter plate influences the wake of the cylinder. Before answering the research questions, it is pertinent to review the observations of the splitter plate motion. From a structural perspective, the preliminary analysis of the plate motion showed that increasing the Reynolds number produced four distinct regimes which were studied further: *crossover*, *baseline*, *reduced amplitude*, and *chaotic*. In the *crossover* regime, the splitter plate oscillations showed low amplitude two-dimensional motion with features of the first bending mode. The *baseline* showed a distinct first bending mode with largely two-dimensional oscillations. The amplitude of the oscillation was observed to be significantly larger than that in the crossover regime. As the Reynolds number increased, it was found that the amplitude of the oscillations decreased and the plate motion was increasingly three-dimensional, this regime was thus called the *reduced amplitude* regime. At a higher Reynolds number, the splitter plate motion was fully three-dimensional and chaotic. Thus, this regime was aptly called the *chaotic* regime.

The first research question aims to answer the influence of the splitter plate on the wake dynamics when compared to the bare cylinder. The time series developed for the cylinder wake showed periodic oscillations which appeared as a dominant peak in the PSD plot. It was observed that the bare cylinder showed consistent spanwise coherent vortex shedding with a Strouhal number of approximately 0.2 in line with the literature. As the flow was still sub-critical, there were no significant changes across different velocities. The proper orthogonal decomposition revealed that the energy content was generally dominated by the first two modes. Additionally, the mode shapes revealed normal vortex roll-up and convection. The statistical analysis revealed a short recirculation region with small shear layers on either side of the cylinder. Across different velocities, the wake was disrupted by the motion of the splitter plate which appeared to dampen the oscillations in the wake. As a result, the PSD plot did not reveal a distinct peak (*Baseline and Chaotic Motion regimes*), or the peak had a lower magnitude (*Reduced Amplitude and Crossover regimes*). It was noted that the presence of the splitter plate elongated the shear layers as well as the recirculation bubble. In general, it was also observed that the splitter plate affects the spanwise coherency of the wake by breaking the vortex tubes into smaller turbulent structures. This was also observed through the high-frequency contributions of the splitter plate in the PSD plot when compared to the bare cylinder. While the energy content revealed that the splitter plate reduced the energy in the wake in both the streamwise and transverse directions. The mode shapes indicated that

the roll-up process was elongated and happened along the length of the plate. Additionally, there was a significant influence of the plate on the near wake where communication was most restricted. In the transverse direction, the mode shapes showed that the vortex convection was happening much later than the bare cylinder.

A notable feature of the splitter motion was the encountering of a 'burst'. A burst was characterized by a period of resonant splitter plate motion. In this duration, the three-dimensional motion of the splitter plate was replaced with coherent two-dimensional motion of low frequency and large amplitude in the first bending mode. The burst occurred at random at different velocities making measurement recording difficult. However, a burst was recorded in the chaotic regime for comparison. The statistical analysis of the flowfield revealed that there was a reduction in the recirculation bubble and the shortening of the shear layers when compared to the regular splitter plate motion. This was attributed to the increased communication between the shear layers due to the plate motion. The two-dimensional motion of the plate reintroduced a spanwise coherent wake that oscillated periodically. The periodic vortex shedding appeared as a distinct peak with a higher magnitude but at a reduced frequency, indicating that the vortex shedding happened at a lower frequency. Additionally, the POD showed convection of vortices that was similar to the cylinder flow case, although the roll-up process was still affected by the plate.

On reviewing these observations, it can be concluded that the introduction of the splitter plate into the wake affects the normal vortex formation processes by reducing the communication between the shear layers of the cylinder. The communication of the shear layers is critical in the entrainment, backflow, and crossflow processes of the formation region. As a consequence three-dimensional (bending and torsion) motion of the splitter plate causes the splitter plate to be in a two way coupling with the wake. The vortex shedding is diminished in intensity and magnitude, and this is how the splitter plate affects the wake dynamics when compared to a bare cylinder.

Having discussed the influence on the splitter plate on the wake when compared to a bare cylinder, the second research question is about achieving some sort of characterization based on the above conclusions. This, however, is not straightforward as there are two ways to approach the question of characterization. The first is looking at the plate behavior over the range of Reynolds number, comparing the wake behavior. Even though the splitter plate displayed a distinct motion discussed earlier, the fundamental effect on vortex shedding is the same, i.e, weakening of the vortex shedding due to the interference of the splitter plate in the formation region. Thus, from a wake dynamics perspective, it is difficult to make a categorization on any distinct influence of the splitter plate. The second way of approaching this question of characterization is by comparing a burst to the regular splitter plate motion. In this case, it is possible to make a distinction as the two cases display significantly different wake behavior. We see that the wake of the two-dimensional resonant burst motion is spanwise coherent, and periodic, and displays a convection of vortices that is similar to the bare cylinder. These features of the wake are noticeably absent in the regular motion of the splitter plate which shows damped and delayed vortex convection. In addition, the energy fractions of the resonant regime are also much higher in comparison to the regular plate motion. The mechanisms of the burst initiation and end, however, have not been covered in this present study and are topics for further research.

7.2. Recommendations

Although the present work presents insight into the wake dynamics and nature of coupling of a cylinder with a splitter plate, a few improvements have been envisioned for future work. The recommendations are aimed at improving or rectifying the experimental and processing methods as well as proposing avenues for further research.

One of the challenges encountered in the processing was with the camera setup. The cameras were positioned on only a single side of the splitter plate as the plate was deemed to be optically transparent. This simplified the setup but under high deformations, it was noted that fewer tracks were developed on the other side of the splitter plate. The deformed splitter plate was causing the algorithm to develop false tracks and thus eliminate them. It is recommended that the camera be positioned on either side of the splitter plate to capture the flow particles accurately even under large deformations. In many of the cases, it was found that the seeding concentration in the flow was too high. As a result, too many particles were detected for the algorithm to develop tracks effectively. This caused the loss of spatial resolution which had to be corrected by using the different tolerances of the algorithm in particle detection intensity, triangulation errors, etc. It would be beneficial to have more control over the seeding rake in the wind tunnel to achieve the right seeding concentration in the flow. It is advised to avoid the regular pattern of structural markers on the splitter plate as it posed some roadblocks in image processing. This challenge has been explained in depth in Chapter 5. A new framework of structural marker positioning will result in smoother image analysis with no loss in spatial resolution due to ghost particle detection.

Recording the measurements of the burst proved to be challenging, as the initiation occurred at random. As a result, studying the initiation and end of a burst has been left out presently, and is an avenue for future research. Additionally, the present study is focused largely on the wake effects of the splitter plate and the study of structural markers has been out of scope. Future studies of structural deformations can help further insights into energy harvesting and wake control.

Bibliography

- [1] R.J Adrian et al. “Particle-imaging techniques for experimental fluid mechanics”. In: *Annual review of fluid mechanics* 23.1 (1991), pp. 261–304.
- [2] TU Delft Aerodynamics. *Experimental Wiki*. 2022. URL: <https://wiki.tudelft.nl/bin/view/Organisation/LR/WikiAero/ExperimentalWiki/WebHome>.
- [3] TU Delft Aerodynamics. *Helium Filled Soap Bubbles Wiki*. 2022. URL: <https://wiki.tudelft.nl/bin/view/Organisation/LR/WikiAero/ExperimentalWiki/PIVsystemsWiki/HfsbFluidSupplyUnits>.
- [4] TU Delft Aerodynamics. *LED Flashlight Wiki*. 2022. URL: <https://wiki.tudelft.nl/bin/view/Organisation/LR/WikiAero/ExperimentalWiki/PIVsystemsWiki/LEDWiki>.
- [5] TU Delft Aerodynamics. *Photron Fast Cam Wiki*. 2022. URL: <https://wiki.tudelft.nl/bin/view/Organisation/LR/WikiAero/ExperimentalWiki/PIVsystemsWiki/PhotronFastcamWiki>.
- [6] N Agüera et al. “Ensemble 3D PTV for high resolution turbulent statistics”. In: *Measurement Science and Technology* 27.12 (2016), p. 124011.
- [7] H.D Akaydn, N Elvin, and Y Andreopoulos. “Wake of a cylinder: a paradigm for energy harvesting with piezoelectric materials”. In: *Experiments in Fluids* 49.1 (2010), pp. 291–304.
- [8] H Akilli et al. “Control of vortex shedding of circular cylinder in shallow water flow using an attached splitter plate”. In: *Journal of Fluids Engineering* 130.4 (2008).
- [9] J.J Allen and A.J Smits. “Energy harvesting eel”. In: *Journal of fluids and structures* 15.3-4 (2001), pp. 629–640.
- [10] EA Anderson and AA Szewczyk. “Effects of a splitter plate on the near wake of a circular cylinder in 2 and 3-dimensional flow configurations”. In: *Experiments in Fluids* 23.2 (1997), pp. 161–174.
- [11] J.D Anderson Jr. *Fundamentals of aerodynamics*. Tata McGraw-Hill Education, 2010.
- [12] CJ Apelt, GS West, and Albin A Szewczyk. “The effects of wake splitter plates on the flow past a circular cylinder in the range $104 < R < 5 \times 10^4$ ”. In: *Journal of Fluid Mechanics* 61.1 (1973), pp. 187–198.
- [13] M Armandei, A.C Fernandes, and A Bakhshandeh Rostami. “Hydroelastic buffeting assessment over a vertically hinged flat plate”. In: *Experimental Techniques* 40.2 (2016), pp. 833–839.
- [14] G.R.S Assi and P.W Bearman. “Transverse galloping of circular cylinders fitted with solid and slotted splitter plates”. In: *Journal of Fluids and Structures* 54 (2015), pp. 263–280.
- [15] G.R.S Assi, P.W Bearman, and M.A Tognarelli. “On the stability of a free-to-rotate short-tail fairing and a splitter plate as suppressors of vortex-induced vibration”. In: *Ocean engineering* 92 (2014), pp. 234–244.
- [16] C Atkinson and J Soria. “An efficient simultaneous reconstruction technique for tomographic particle image velocimetry”. In: *Experiments in Fluids* 47.4 (2009), pp. 553–568.

- [17] G Berkooz, P Holmes, and J.L Lumley. “The proper orthogonal decomposition in the analysis of turbulent flows”. In: *Annual review of fluid mechanics* 25.1 (1993), pp. 539–575.
- [18] S Bilgen et al. “Global warming and renewable energy sources for sustainable development: a case study in Turkey”. In: *Renewable and sustainable energy reviews* 12.2 (2008), pp. 372–396.
- [19] R.D Blevins. “Flow-induced vibration”. In: *New York* (1977).
- [20] M.S Bloor. “The transition to turbulence in the wake of a circular cylinder”. In: *Journal of Fluid Mechanics* 19.2 (1964), pp. 290–304.
- [21] J Bosbach, M Kühn, and C Wagner. “Large scale particle image velocimetry with helium filled soap bubbles”. In: *Experiments in fluids* 46.3 (2009), pp. 539–547.
- [22] GS Cardell. “Flow past a circular cylinder with a permeable splitter plate”. In: *California Institute of Technology* (1993).
- [23] Giuseppe Carlo Alp Caridi. “Development and application of helium-filled soap bubbles: For large-scale PIV experiments in aerodynamics”. In: (2018).
- [24] Shoei-Sheng Chen. *Flow-induced vibration of circular cylindrical structures*. Tech. rep. Argonne National Lab.(ANL), Argonne, IL (United States), 1985.
- [25] A Cherubini et al. “Airborne Wind Energy Systems: A review of the technologies”. In: *Renewable and Sustainable Energy Reviews* 51 (2015), pp. 1461–1476.
- [26] H Choi, Woo-Pyung Jeon, and J Kim. “Control of flow over a bluff body”. In: *Annu. Rev. Fluid Mech.* 40 (2008), pp. 113–139.
- [27] J.M Cimbalá and J Leon. “Drag of freely rotatable cylinder/splitter-plate body at sub-critical Reynolds number”. In: *AIAA journal* 34.11 (1996), pp. 2446–2448.
- [28] B.S.H Connell and D.K.P Yue. “Flapping dynamics of a flag in a uniform stream”. In: *Journal of fluid mechanics* 581 (2007), pp. 33–67.
- [29] M Coutanceau and J-R Defaye. “Circular cylinder wake configurations: a flow visualization survey”. In: (1991).
- [30] G De Nayer and M Breuer. “Numerical FSI investigation based on LES: Flow past a cylinder with a flexible splitter plate involving large deformations (FSI-PfS-2a)”. In: *International Journal of Heat and Fluid Flow* 50 (2014), pp. 300–315.
- [31] G De Nayer et al. “Flow past a cylinder with a flexible splitter plate: A complementary experimental–numerical investigation and a new FSI test case (FSI-PfS-1a)”. In: *Computers & Fluids* 99 (2014), pp. 18–43.
- [32] TU Delft. *W-Tunnel*. 2022. URL: <https://www.tudelft.nl/lr/organisatie/afdelingen/flow-physics-and-technology/facilities>.
- [33] I Dincer. “Renewable energy and sustainable development: a crucial review”. In: *Renewable and sustainable energy reviews* 4.2 (2000), pp. 157–175.
- [34] J.R.F Diógenes et al. “Barriers to onshore wind energy implementation: A systematic review”. In: *Energy Research & Social Science* 60 (2020), p. 101337.
- [35] G.E Elsinga et al. “Tomographic particle image velocimetry”. In: *Experiments in fluids* 41.6 (2006), pp. 933–947.
- [36] F.G Ergin, B.B Watz, and N.F Gade-Nielsen. “A review of planar PIV systems and image processing tools for lab-on-chip microfluidics”. In: *Sensors* 18.9 (2018), p. 3090.

- [37] D.E Faleiros et al. “Generation and control of helium-filled soap bubbles for PIV”. In: *Experiments in Fluids* 60.3 (2019), pp. 1–17.
- [38] C.A Friehe. “Vortex shedding from cylinders at low Reynolds numbers”. In: *Journal of Fluid Mechanics* 100.2 (1980), pp. 237–241.
- [39] JH Gerrard. “The mechanics of the formation region of vortices behind bluff bodies”. In: *Journal of fluid mechanics* 25.2 (1966), pp. 401–413.
- [40] LaVision GmbH. *DaVis Product Manual*. 2021. URL: <https://wiki.tudelft.nl/pub/Organisation/LR/WikiAero/ExperimentalWiki>.
- [41] M.H Hayes. *Statistical digital signal processing and modeling*. John Wiley & Sons, 2009.
- [42] G.T Herman and A Lent. “Iterative reconstruction algorithms”. In: *Computers in biology and medicine* 6.4 (1976), pp. 273–294.
- [43] C Hu and W Koteraayama. “Numerical study on a two-dimensional circular cylinder with a rigid and an elastic splitter plate in uniform flow”. In: *The Fourth International Offshore and Polar Engineering Conference*. OnePetro. 1994.
- [44] P Huerre and P.A Monkewitz. “Local and global instabilities in spatially developing flows”. In: *Annual review of fluid mechanics* 22.1 (1990), pp. 473–537.
- [45] A Igbalajobi et al. “The effect of a wake-mounted splitter plate on the flow around a surface-mounted finite-height circular cylinder”. In: *Journal of Fluids and Structures* 37 (2013), pp. 185–200.
- [46] S.H Kwon et al. “The effects of drag reduction by ribbons attached to cylindrical pipes”. In: *Ocean engineering* 29.15 (2002), pp. 1945–1958.
- [47] J Lee and D You. “Study of vortex-shedding-induced vibration of a flexible splitter plate behind a cylinder”. In: *Physics of Fluids* 25.11 (2013), p. 110811.
- [48] S Liang et al. “Vortex-induced vibration and structure instability for a circular cylinder with flexible splitter plates”. In: *Journal of Wind Engineering and Industrial Aerodynamics* 174 (2018), pp. 200–209.
- [49] Y.C Liang et al. “Proper orthogonal decomposition and its applications Part I: Theory”. In: *Journal of Sound and vibration* 252.3 (2002), pp. 527–544.
- [50] J.H Lienhard et al. *Synopsis of lift, drag, and vortex frequency data for rigid circular cylinders*. Vol. 300. Technical Extension Service, Washington State University Pullman, WA, 1966.
- [51] Z Luo and G Chen. *Proper orthogonal decomposition methods for partial differential equations*. Academic Press, 2018.
- [52] HG Maas, A Gruen, and D Papantoniou. “Particle tracking velocimetry in three-dimensional flows”. In: *Experiments in fluids* 15.2 (1993), pp. 133–146.
- [53] A Melling. “Tracer particles and seeding for particle image velocimetry”. In: *Measurement science and technology* 8.12 (1997), p. 1406.
- [54] A.E Perry and M.S Chong. “On the mechanism of wall turbulence”. In: *Journal of Fluid Mechanics* 119 (1982), pp. 173–217.
- [55] M Raffel, C.E Willert, J Kompenhans, et al. *Particle image velocimetry: a practical guide*. Vol. 2. Springer, 1998.
- [56] A Roshko. *On the development of turbulent wakes from vortex streets*. Tech. rep. 1954.
- [57] A Roshko. *On the drag and shedding frequency of two-dimensional bluff bodies*. Tech. rep. 1954.

- [58] A Roshko. “On the wake and drag of bluff bodies”. In: *Journal of the aeronautical sciences* 22.2 (1955), pp. 124–132.
- [59] P Sadorsky. “Wind energy for sustainable development: Driving factors and future outlook”. In: *Journal of Cleaner Production* 289 (2021), p. 125779.
- [60] G González Saiz, A Sciacchitano, and F Scarano. “On the closure of Collars triangle by optical diagnostics”. In: *Experiments in Fluids* 63.8 (2022), pp. 1–14.
- [61] F Scarano. “Tomographic PIV: principles and practice”. In: *Measurement Science and Technology* 24.1 (2012), p. 012001.
- [62] F Scarano et al. “On the use of helium-filled soap bubbles for large-scale tomographic PIV in wind tunnel experiments”. In: *Experiments in Fluids* 56.2 (2015), pp. 1–12.
- [63] D Schanz, A Gesemann, and A Schröder. “Shake-The-Box: Lagrangian particle tracking at high particle image densities”. In: *Experiments in fluids* 57.5 (2016), pp. 1–27.
- [64] D Schanz et al. “Non-uniform optical transfer functions in particle imaging: calibration and application to tomographic reconstruction”. In: *Measurement Science and Technology* 24.2 (2012), p. 024009.
- [65] A Sciacchitano and F Scarano. “Elimination of PIV light reflections via a temporal high pass filter”. In: *Measurement Science and Technology* 25.8 (2014), p. 084009.
- [66] S Shukla, RN Govardhan, and JH Arakeri. “Dynamics of a flexible splitter plate in the wake of a circular cylinder”. In: *Journal of Fluids and Structures* 41 (2013), pp. 127–134.
- [67] J Song et al. “Performance of a circular cylinder piezoelectric wind energy harvester fitted with a splitter plate”. In: *Applied Physics Letters* 111.22 (2017), p. 223903.
- [68] G.W Taylor et al. “The energy harvesting eel: a small subsurface ocean/river power generator”. In: *IEEE journal of oceanic engineering* 26.4 (2001), pp. 539–547.
- [69] J Wang et al. “The state-of-the-art review on energy harvesting from flow-induced vibrations”. In: *Applied Energy* 267 (2020), p. 114902.
- [70] P Welch. “The use of fast Fourier transform for the estimation of power spectra: a method based on time averaging over short, modified periodograms”. In: *IEEE Transactions on audio and electroacoustics* 15.2 (1967), pp. 70–73.
- [71] B Wieneke. “Iterative reconstruction of volumetric particle distribution”. In: *Measurement Science and Technology* 24.2 (2012), p. 024008.
- [72] B Wieneke. “Volume Self-Calibration for Stere-PIV and Tomographic PIV”. In: *7th Int Symp on Particle Image Velovimetry, Rome, Italy, 2007*. 2007.
- [73] N Wiener. *Extrapolation, interpolation, and smoothing of stationary time series, vol. 2*. 1949.
- [74] CH Wiliamson. “Vortex dynamics in the cylinder wake”. In: (1996).
- [75] C.E Willert and M Gharib. “Digital particle image velocimetry”. In: *Experiments in fluids* 10.4 (1991), pp. 181–193.
- [76] C.E Willert et al. “Pulsed operation of high-power light emitting diodes for imaging flow velocimetry”. In: *Measurement Science and Technology* 21.7 (2010), p. 075402.
- [77] C.H.K Williamson. “Three-dimensional wake transition”. In: *Journal of Fluid Mechanics* 328 (1996), pp. 345–407.
- [78] J.R Wright and J.E Cooper. *Introduction to aircraft aeroelasticity and loads*. Vol. 20. John Wiley & Sons, 2008.

-
- [79] J Wu and C Shu. “Numerical study of flow characteristics behind a stationary circular cylinder with a flapping plate”. In: *Physics of Fluids* 23.7 (2011), p. 073601.
- [80] J Wu, C Shu, and N Zhao. “Investigation of flow characteristics around a stationary circular cylinder with an undulatory plate”. In: *European Journal of Mechanics-B/Fluids* 48 (2014), pp. 27–39.
- [81] J Wu et al. “Spanwise wake structures of a circular cylinder and two circular cylinders in tandem”. In: *Experimental Thermal and Fluid Science* 9.3 (1994), pp. 299–308.
- [82] Y Yu, Y Liu, and X Amandolese. “A review on fluid-induced flag vibrations”. In: *Applied Mechanics Reviews* 71.1 (2019).

A

Crossover Regime: Results

Once the baseline condition has been established and understood, we can now proceed to compare the crossover regime with the sporadic resonance condition. In this regime, the visual observations showed an increasing amplitude with the appearance of the first mode of oscillation although no resonance was observed. The visual observations and a detailed description can be found in Chapter 4 and Figure 4.6

A.1. Statistical Analysis

We begin the comparison by looking at the mean and standard deviations in the stream-wise direction. The mean velocity field shows a recirculation bubble at the base of the wake with small shear layers on either side. This is consistent with the baseline and shows similar recirculation and shear layer features. The splitter plate restricts the communication between the shear layers. As a result, the entrainment and vortex formation processes are affected. As a result, we see that the fluctuations elongate to the length of the splitter plate. This also causes the recirculation bubble to elongate along the span of the plate. This is also consistent with the baseline. The statistics of the transverse velocity component show the counter-sign regions that contain the recirculation bubble. In the case of the cylinder without the splitter plate, we see two counter-sign regions as well as some near-wake structures. This is similar to the structures observed in the baseline. The presence of the splitter plate elongates the counter-sign regions as well as being moved rearwards due to delays in vortex formation. The region of fluctuations in the wake has also moved rearwards with two additional branches. The branches are a result of the plate motion in the wake which causes some extra fluctuations in the wake.

Overall, the wakes of the splitter plate and the cylinder are consistent with the baseline and do not show significant variations as far as the statistics are concerned.

A.2. Time Series and Spectral Decomposition

Since the flow is still in the sub-critical regime [29], the transverse velocity component of the cylinder without the splitter plate shows periodic oscillations with an amplitude of $\approx \pm 2$ m/s. This periodicity is reflected in the power spectral density as a sharp peak of about

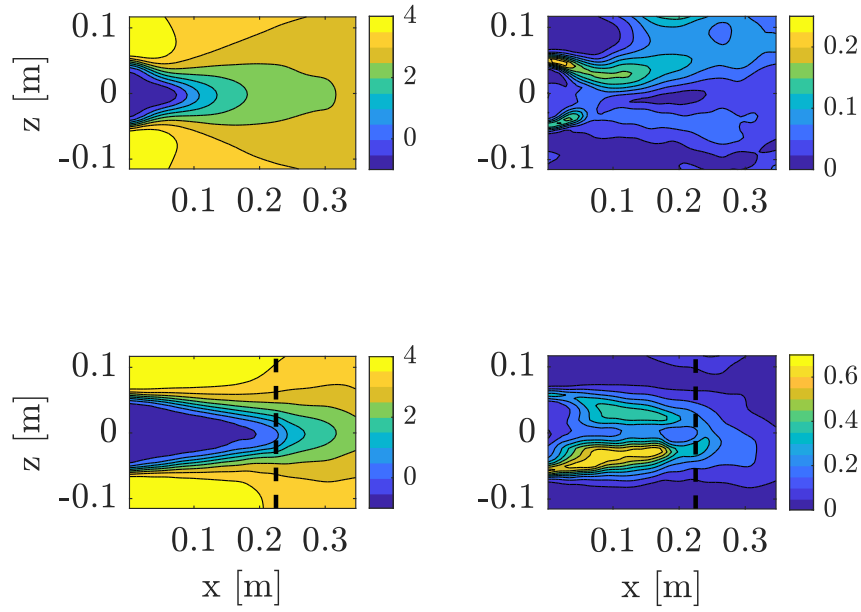


Figure A.1: The streamwise mean and standard deviation for the case $Re = 22,000$ (*Top: Cylinder without Splitter Plate, Below: Cylinder with Splitter Plate*). The limits of the splitter plate have been marked with a black dashed line. The velocity values are in m/s.

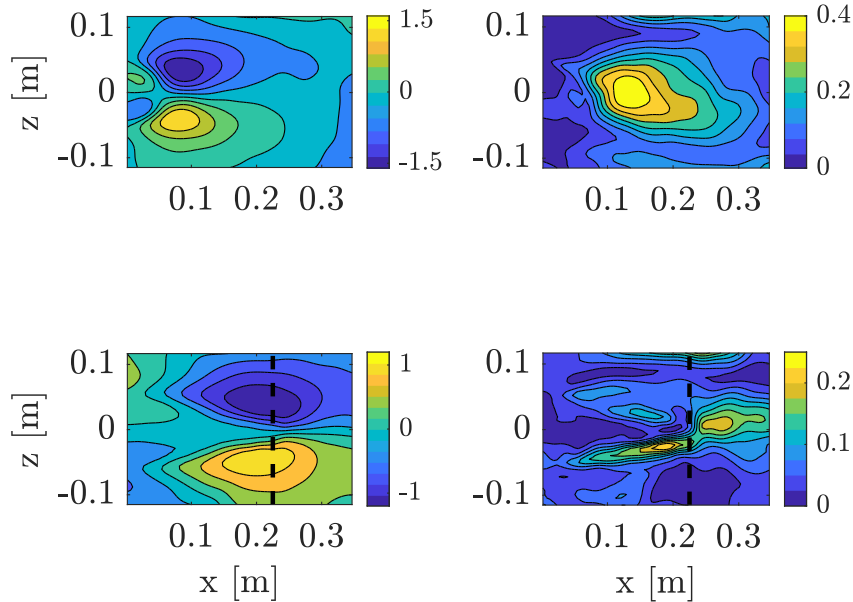


Figure A.2: The transverse mean and standard deviation for the case $Re = 22,000$ (*Top: Cylinder without Splitter Plate, Below: Cylinder with Splitter Plate*). The limits of the splitter plate have been marked with a black dashed line. The velocity values are in m/s.

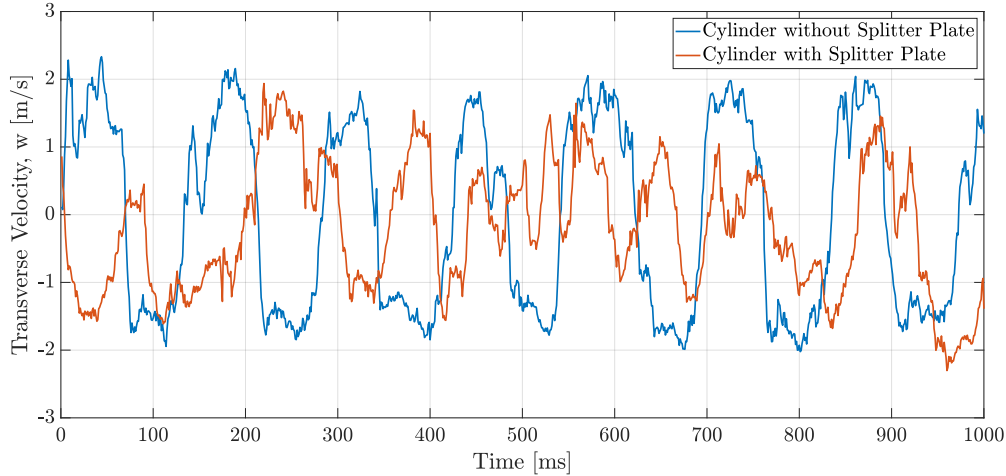


Figure A.3: Time series of instantaneous transverse velocity at the point $x = 0.3089$ m, $y = 0.0179$ m, and $z = -0.0019$ m for the case $Re = 22,000$ (Blue: *Cylinder without Splitter Plate*, Red: *Cylinder with Splitter Plate*)

7.3 Hz. The corresponding Strouhal number is ≈ 0.2 which is consistent with the literature. The amplitude of the oscillations is lower when compared to the baseline case due to the slightly lower freestream velocity. Like the baseline, the cylinder without the splitter plate contains a secondary peak, indicating the influence of higher harmonics in the fluctuating wake. The splitter plate affects this periodicity as can be seen in the red curve of Figure A.3. The magnitude of the oscillations is lower and the fluctuations are more erratic as the splitter plate affects the vortex shedding of the cylinder. This influence can also be seen in the PSD plot, where there is no distinct frequency peak. Instead, there are two peaks with the maximum being 7.3 Hz with the peak having considerably lower intensity when compared to the cylinder without the splitter plate. This indicates that the vortex shedding has been significantly dampened. The high-frequency content of the splitter is not affected, unlike the baseline. This shows that the splitter does not increase the turbulence in the wake significantly and the influence is on the lower frequencies.

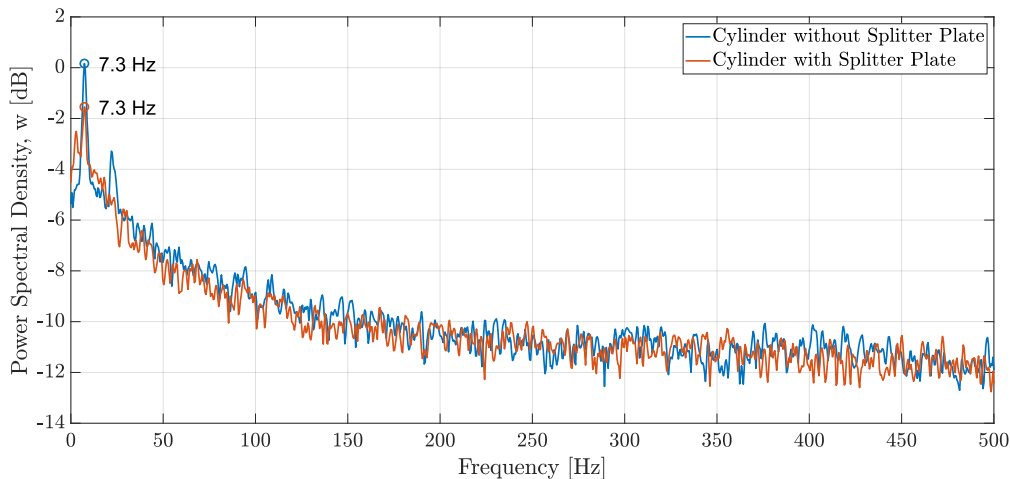


Figure A.4: Power spectral density of instantaneous transverse velocity at the point $x = 0.3089$ m, $y = 0.0179$ m, and $z = -0.0019$ m for the case $Re = 22,000$ (Blue: *Cylinder without Splitter Plate*, Red: *Cylinder with Splitter Plate*)

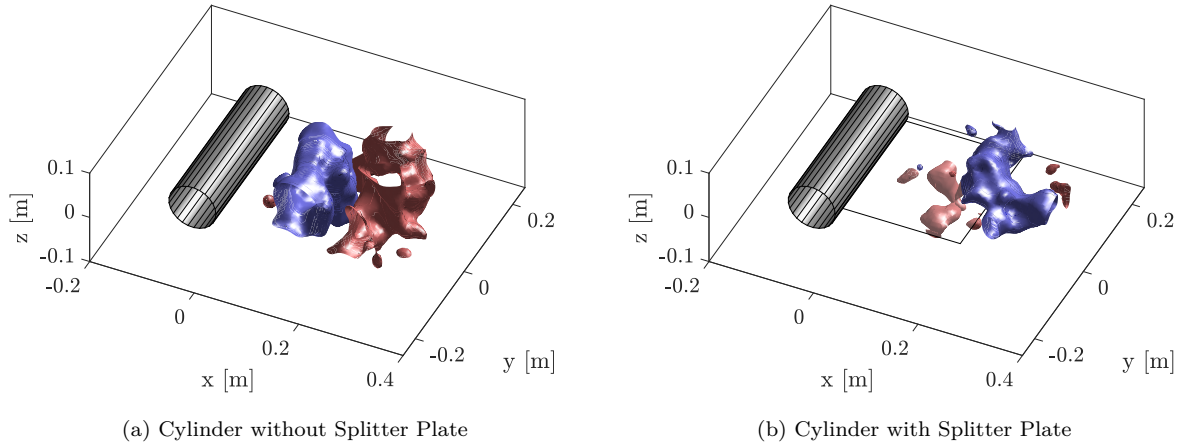


Figure A.5: Isosurfaces highlighting the spanwise coherence of the transverse velocity $w = 1.5$ m/s (in blue) and $w = -1.5$ m/s (in red) for the case $Re = 22,000$. The splitter plate has been shown in its neutral position.

The strong peak of the cylinder without the splitter plate seen in the PSD plot is reflected in the spanwise coherence. Periodic alternating vortices are shed along the span of the cylinder [81]. The introduction of the splitter influences this spanwise vortex formation and the vortices are broken into smaller structures. Although, it can be seen that this effect is not as drastic as observed in some other cases. This is likely due to the fact that the plate itself undergoes low-amplitude, two-dimensional oscillations which does not affect the spanwise coherence to a great extent.

A.3. Proper Orthogonal Decomposition

Figure A.6 reveals the energy content of the first ten modes of wake with and without the splitter plate. In the case of the cylinder without the splitter plate, the energy content is roughly the same as that of the baseline. This can be attributed to the fact the Reynolds numbers of the two cases are not very far apart, hence the physics of the vortex shedding is roughly the same.

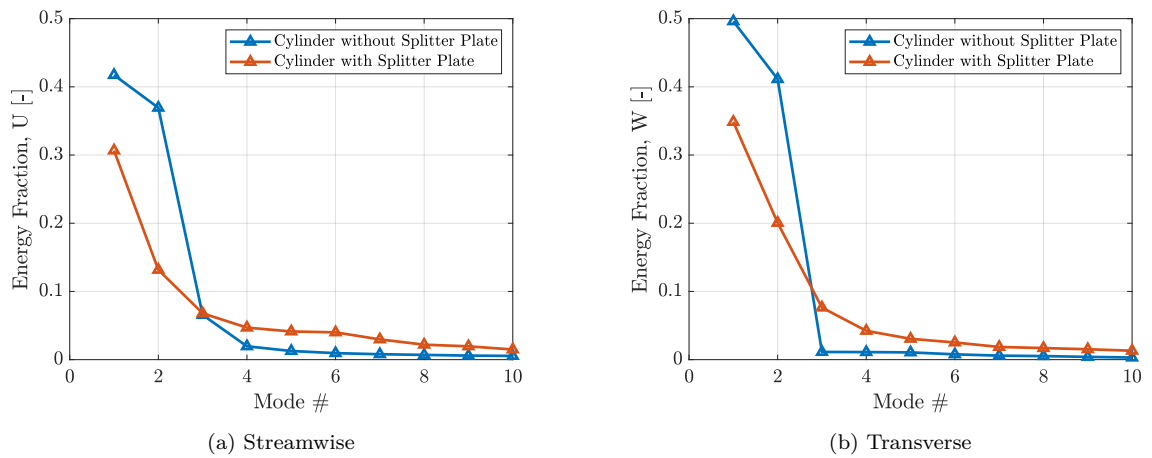


Figure A.6: Energy distribution over the first ten modes for the case $Re = 22,000$

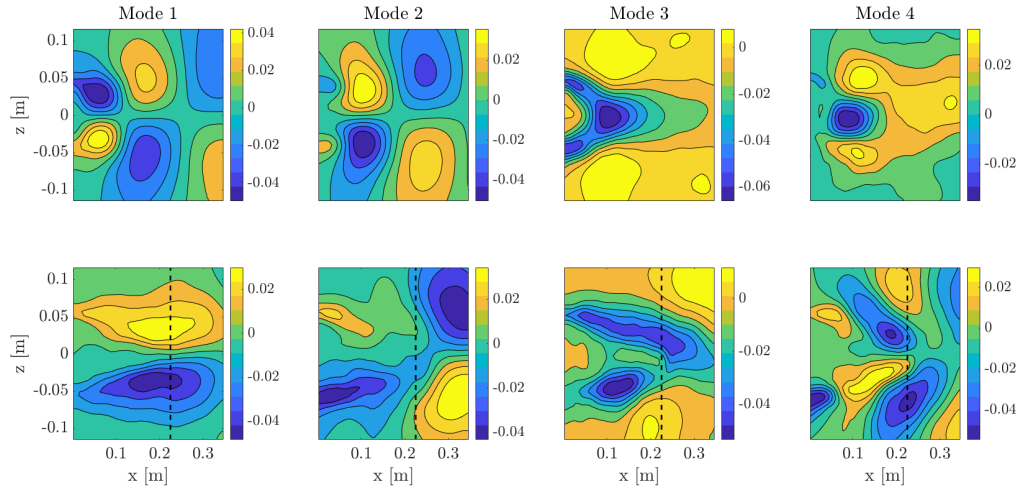


Figure A.7: The first four streamwise mode shapes for the case $Re = 22,000$ (*Top: Cylinder without Splitter Plate, Below: Cylinder with Splitter Plate*). The limits of the splitter plate has been marked with a black dashed line. The velocity values are in m/s.

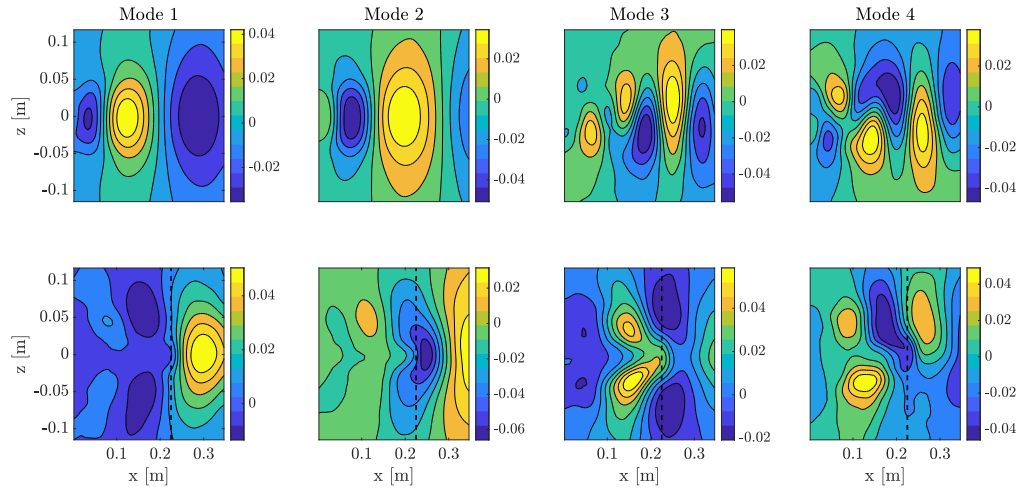


Figure A.8: The first four transverse mode shapes for the case $Re = 22,000$ (*Top: Cylinder without Splitter Plate, Below: Cylinder with Splitter Plate*). The limits of the splitter plate has been marked with a black dashed line. The velocity values are in m/s.

The energy content of the figures above is reflected in the mode shapes of the streamwise and transverse velocity components. Figure A.7 shows the mode shapes in the streamwise direction. In the case of the cylinder without the splitter plate, the mode shapes represent the vortex roll-up and shedding process. The first two modes appear to be in quadrature of phase, indicating strong vortex shedding, similar to the baseline. The splitter plate appears to have drastically affected this process as the first mode does not show the same alternating flow structures. They are instead replaced by two large counter sign regions which are shifted to the tip of the splitter plate. This shows the elongation of the roll-up process along the length of the splitter plate. The second mode of the splitter plate shows some resemblance to the vortex shedding process with the presence of alternating 'blobs'. The near wake structures are elongated due to the long splitter plate and the far wake structures are displaced further into the wake. This also contributes to the drop in the energy content of the second mode in Figure A.6a. The higher modes of the cylinder do not significantly contribute to the process

of vortex shedding and are left out of the discussion, while the splitter plate modes show a random distribution of structures which does not make for a straightforward interpretation.

The transverse velocity mode shapes shown in Figure A.8 depict the convection of the alternating vortices shed from the cylinder. The cylinder without the splitter plate shows consistent alternating vortex shedding that is not very different from the baseline. The splitter plate appears to delay the vortex shedding process as the vortices are convected from the tip of the plate. Like the sporadic resonance case, the splitter plate in the first mode breaks the near-wake vortices into smaller structures on either side of the plate. Additionally, the higher modes of the cylinder without the splitter plate show higher harmonics of vortex shedding, seen as a secondary peak in Figure A.4, the splitter plate wake shows an irregular distribution of structures with no real interpretations from either the time series or the power spectral density plot. 12